THE UNIVERSITY OF QUEENSLAND

AUSTRALIA

Hydraulic Modelling of Unsteady Open Channel Flow: Physical and Analytical Validation of Numerical Models of Positive and Negative Surges

Martina Reichstetter

A thesis submitted for the degree of Master of Philosophy at

The University of Queensland in August 2011

School of Civil Engineering

Declaration by author

This thesis is composed of my original work, and contains no material previously published or written by another person except where due reference has been made in the text. I have clearly stated the contribution by others to jointly-authored works that I have included in my thesis.

I have clearly stated the contribution of others to my thesis as a whole, including statistical assistance, survey design, data analysis, significant technical procedures, professional editorial advice, and any other original research work used or reported in my thesis. The content of my thesis is the result of work I have carried out since the commencement of my research higher degree candidature and does not include a substantial part of work that has been submitted to qualify for the award of any other degree or diploma in any university or other tertiary institution. I have clearly stated which parts of my thesis, if any, have been submitted to qualify for another award.

I acknowledge that an electronic copy of my thesis must be lodged with the University Library and, subject to the General Award Rules of The University of Queensland, immediately made available for research and study in accordance with the *Copyright Act 1968*.

I acknowledge that copyright of all material contained in my thesis resides with the copyright holder(s) of that material.

Statement of Contributions to Jointly Authored Works Contained in the Thesis

"No jointly-authored works."

Statement of Contributions by Others to the Thesis as a Whole

"No contributions by others."

Statement of Parts of the Thesis Submitted to Qualify for the Award of Another Degree

"None."

Published Works by the Author Incorporated into the Thesis

"None."

Additional Published Works by the Author Relevant to the Thesis but not Forming Part of it

REICHSTETTER, M., and CHANSON, H. (2011). "Negative Surge in Open Channel: Physical, Numerical and Analytical Modelling." *Proc. 34th IAHR World Congress*, Brisbane, Australia, 26 June-1 July, Engineers Australia Publication, Eric VALENTINE, Colin APELT, James BALL, Hubert CHANSON, Ron COX, Rob ETTEMA, George KUCZERA, Martin LAMBERT, Bruce MELVILLE and Jane SARGISON Editors, pp.2306-2313.

Acknowledgements

This research project would not have been possible without the support of many people. The author wishes to express her gratitude to her supervisor, Prof. Hubert Chanson who was abundantly helpful and offered invaluable assistance, support and guidance.

Besides my advisor, the author would like to thank my assistant advisor Dr. Luke Toombes for his encouragement and technical support.

Sincere thanks also go to Professor Peter Rutschmann and his team for offering me the exchange opportunity at the Technical University of Munich sharing his resources and expertise. The author would like to express her thanks to Michael Seitz and Shokry Abdelaziz for their support during my stay at the Technical University of Munich.

The author likes to express her gratitude to Dr. Pierre Lubin of the University of Bordeaux for his help and sharing his vast expertise in CFD modeling and formatting of a successful conference presentation.

The author thanks her fellow researchers in the School of Civil Engineering at UQ for the stimulating discussions, especially my office mate Stefan Felder.

Last but not the least; the author would like to thank her family, her parents Hermann Reichstetter and Elisabeth, for supporting her throughout life.

Abstract

Positive and negative surges are generally observed in open channels. Positive surges that occur due to tidal origins are referred to as tidal bores. A positive surge occurs when a sudden change in flow leads to an increase of the water depth, while a negative surge occurs due to a sudden decrease in water depth. Positive and negative surges are commonly induced by control structures, such as the opening and closing of a gate. In this study, the free-surface properties and velocity characteristics of negative and positive surges were investigated physically under controlled conditions, as well as analytically and numerically. Unsteady open channel flow data were collected during the upstream propagation of negative and positive surges. Both, physical and numerical modelling, were performed. Some detailed measurements of free-surface fluctuations were recorded using non-intrusive techniques, including acoustic displacement meters and video recordings. Velocity measurements were sampled with high temporal and spatial resolution using an ADV (200 Hz) at four vertical elevations and two longitudinal locations. The velocity and water depth results were ensemble-averaged for both negative and positive surges. The results showed that the water curvature of the negative surge was steeper near the gate at x=10.5 m compared to further upstream at x=6 m. Both the instantaneous and ensemble-average data showed that in the negative surge the inflection point of the water surface and the longitudinal velocity V_x occurred simultaneously. Also, an increase in V_x was observed at all elevations during the surge passage. For the positive surge the propagation of the bore and the velocity characteristics supported earlier findings by Koch and Chanson (2009) and Docherty and Chanson (2010). The surge was a major discontinuity in terms of the free-surface elevations, and a deceleration of the longitudinal velocities V_x was observed during the surge passage. A number of analytical and numerical models were tested, including the analytical and numerical solutions of the Saint-Venant equations and a computational fluid dynamics (CFD) package. Overall, all models provided reasonable results for the negative surge. None of the models were able to provide a good agreement with the measured data for the positive surge. The study showed that theoretical models may be applied successfully to unsteady flow situations with simple channel geometry. Also, it was found that the selection of the appropriate mesh size for CFD simulations is essential in highly unsteady turbulent flows, such as a positive surge, where the surge front is a sharp discontinuity in terms of water elevation, velocity and pressure. It was concluded that the highly unsteady open channel flows remain a challenge for professional engineers and researchers.

Keywords

modelling, unsteady open channel flows, positive surges, negative surges, physical modelling, numerical modelling, theoretical modelling, Saint-Venant equations, laboratory experiments, computational fluid dynamics (CFD)

Australian and New Zealand Standard Research Classifications (ANZSRC)

090509 Water Resources Engineering

Table of Contents

List of Figures

List of Tables

Notation

The following symbols are used in this report:

A	flow cross-section area (m^2);
B	free-surface width (m);
C	wave celerity (m/s);
C_o	initial celerity (m/s) of a small disturbance in the reservoir with initial reservoir depth d_o;
d	flow depth (m) measured normal to the invert;
d_o	initial reservoir height (m) measured normal to the chute invert;
D_H	hydraulic diameter (m);
Fr	1- flow Froude number: Fr=$V/\sqrt{g \times d}$;
	2- surge Froude number: Fr=$(V+U)/\sqrt{g \times d}$;
f	Darcy-Weisbach friction factor;
g	gravity constant: g=9.8 m/s^2;
L	channel length (m);
P_w	wetted perimeter (m);
Q	volume flow rate (m^3/s);
S_f	friction slope;
S_o	bed slope: $S_o=\sin\theta$;
t	time (s);
U	surge celerity (m/s) positive u/s;
V	flow velocity (m/s);
V_o	initial flow velocity (m/s);
V_x	flow velocity component (m/s) in x-direction;

V_y flow velocity component (m/s) in y-direction;

V_z flow velocity component (m/s) in z-direction;

W channel width (m);

x longitudinal distance (m) measured from the upstream end;

x' dimensionless variable;

z vertical elevation (m);

Greek symbols

θ bed slope angle;

o initially steady flow conditions in the channel;

Notation

D/Dt absolute differential;

$\partial/\partial y$ partial differentiation with respect to y;

Abbreviations

U/S upstream;

D/S downstream;

ADV acoustic Doppler velocimeter;

ADM acoustic displacement meter;

CFD computational fluid dynamics.

1 Introduction

1.1 Description

A positive surge occurs when a sudden change in flow leads to an increase of the water depth. On the other hand, a negative surge occurs due to a sudden decrease in water depth (Figure 1- 1). Positive and negative surges are commonly induced by control structures, such as the opening and closing of a gate respectively (e.g. Henderson 1966, Chanson 2004). Positive and negative surges are generally observed in man-made channels. Positive surges that occur due to tidal origins are referred to as tidal bores (Chanson 2010). Surge waves resulting from dam breaks have been responsible for great destruction. The surge front as a result of a shock, like the complete closing or opening of a gate, is characterised by a sudden discontinuity and extremely rapid variations of flow depth and velocity. Many studies have been conducted looking at surges under controlled laboratory conditions.

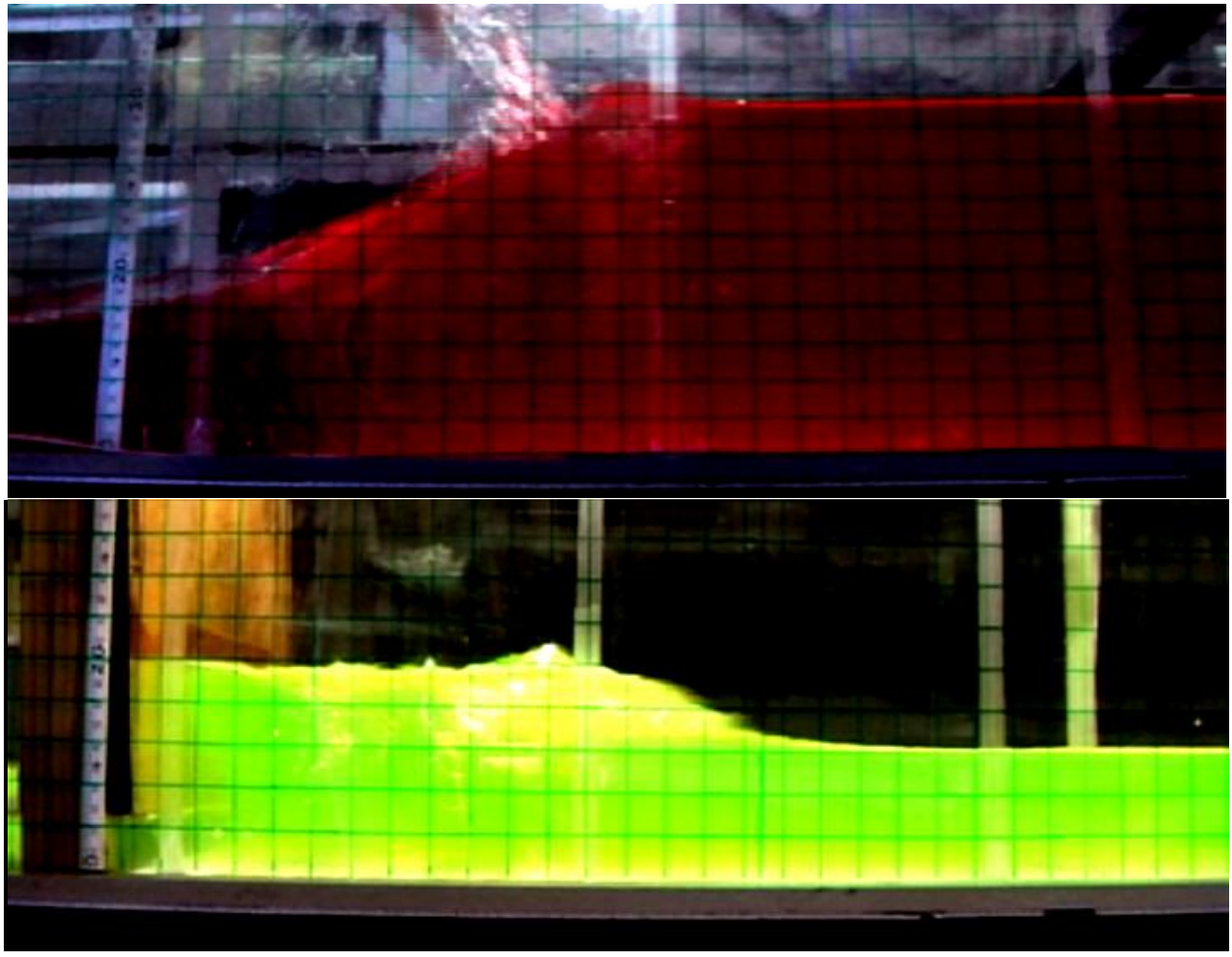

Figure 1-1: Photographs of a negative and positive surge

Many predictions of surge waves rely on numerical analysis, which are often validated against limited data sets. The complex flow situations are solved using empirical approximation and numerical models, which are based on derivates of basic principles, such as the backwater equation, Saint-Venant and Navier-Stokes equations. Numerical models are required to make some form of approximation to solve these principles. Consequently, all models have their limitations. To date most limitations are neither well understood nor documented.

1.2 Objectives and outline

In this study, the free-surface properties and the velocity characteristics of negative and positive surges are investigated physically under controlled conditions, as well as analytically and numerically. New physical modelling is carried out for the specific purpose to provide benchmark data for numerical model validation. A number of numerical models are tested, including the integration of the Saint-Venant equations and a more advanced CFD package. The validation of the numerical models is examined in the cases of positive and negative surges, including the verification of the model predictions against physical model data.

The aim of this work is to present the background and theory, as well as the results of the experimental and numerical investigation undertaken on positive and negative surges.

This report describes a series of experimental and numerical analyses of positive and negative surges. In the next section, a short overview of previous research for negative and positive surges is presented. In section 3, the experimental setup is presented. Section 4 lists and discusses the experimental results. In section 5 the numerical model setup and results are presented. Comparisons of numerical and physical results are presented and discussed in section 6. Conclusions are presented in section 7.

2 Positive and negative surges: a bibliographic review

2.1 Presentation

Water flows can be divided into two flow regimes, steady flows and unsteady flows. In steady flows the velocity and depth do not change with time at a given location in a channel. In unsteady flows the flow parameters change with time and location. Unsteady flows are frequently observed in water supply systems, hydropower canals, and channels with junctions, as well as dam-breaks. In a channel filled with water, the sudden increase in water depth is referred to as a positive surge, while the negative surge is characterised by a reduction in water depth. Historically, some major contributions on surges were published by Bazin (1865), Barré de Saint Venant (1871) and Boussinesq (1877). More recently, some unsteady velocity measurements were conducted using acoustic Doppler velocimeters (ADV) (Koch and Chanson 2009, Chanson 2010, 2011). Figure 2-1(a) shows the definition sketch of a positive surge for an observer standing on the bank. Figure 2-1 (b) shows the definition sketch of a negative surge.

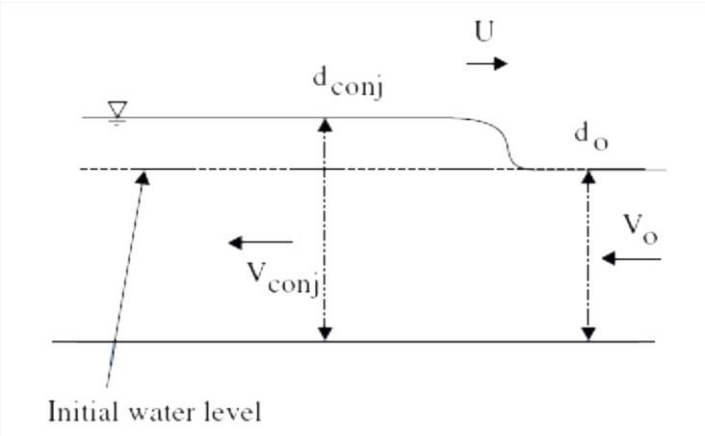

(a) Definition sketch of a positive surge (Chanson 2004)

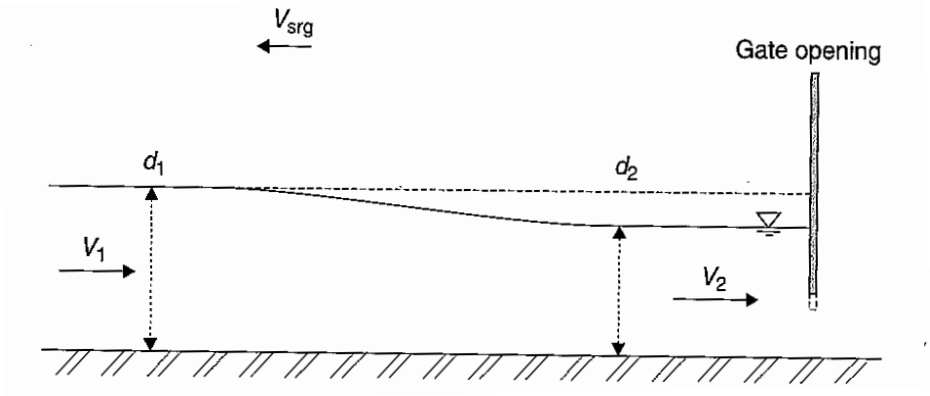

(b) Definition sketch of a negative surge (Chanson 2004)

Figure 2-1: Definition sketch of (a) positive surge and (b) negative surge

2.2 Basic equations

In unsteady open channel flows, water depth and velocities change with time and longitudinal position. The Saint-Venant equations consist of the momentum and continuity equations and are used in the calculation of one-dimensional free-surface flows. The basic assumptions of the Saint-Venant equation are: (1) the flow is one dimensional; (2) the streamline curvature is small and the pressure distribution is hydrostatic; (3) the flow resistance is the same as for a steady uniform flow with the identical depth and velocity; (4) the bed slope is small enough so that $\cos\theta \approx 1$ and $\sin\theta \approx \tan\theta \approx 0$; (5) constant water density; the channel has fixed boundaries and air entrainment and sediment motion are neglected (Chanson 2004). Considering these assumptions, every point at all time during the progression of the surge can be characterised by two variables, such as V and d: where V is the velocity and d is the water depth. The following system of two partial differential equations can be used to describe the unsteady flow properties:

$$\frac{\partial d}{\partial t} + \frac{A}{B}\frac{\partial V}{\partial x} + V\frac{\partial d}{\partial x} + \frac{V}{B}\left(\frac{\partial A}{\partial x}\right)_{d=cons\tan t} = 0 \qquad (2\text{-}1)$$

$$\frac{\partial V}{\partial t} + V\frac{\partial V}{\partial x} + g\frac{\partial d}{\partial x} + g(S_f - S_o) = 0 \qquad (2\text{-}2)$$

where t is the time, A is the cross-section area, B is the free-surface width, x is the streamwise coordinate, S_o is the bed slope, θ is the angle between the bed and the horizontal, with θ > 0 for a downward slope and S_f is the friction slope (Chanson 2004).

The friction slope can be defined as $S_f = fv^2/(2gD_H)$ where D_H is the hydraulic diameter and the Darcy friction factor f is a non-linear function of both the Reynolds number and the relative roughness (Chanson 2004). Equation (2-1) is the continuity equation and (2-2) is the momentum equation (Liggett 1994, Montes 1998, Chanson 2004).

2.3 Analytical solution of the Saint-Venant equations

Simple solutions of the Saint-Venant equations may be obtained using the "simple wave" approximation. In this study the simple wave method is used to calculate the water surface profile of the negative wave. A simple wave is defined as a wave for which $(S_o = S_f = 0)$ with constant initial water depth and flow velocity (Chanson 2004). To solve the simple wave, the Saint-Venant equations become a characteristic system of equations:

$$\frac{D}{Dt} \times (V + 2C) = 0 \qquad \text{forward characteristic} \qquad (2\text{-}3)$$

$$\frac{D}{Dt} \times (V - 2C) = 0 \qquad \text{backward characteristic} \qquad (2\text{-}4)$$

along:

$$\frac{dx}{dt} = V + C \qquad \text{forward characteristic} \qquad (2\text{-}5)$$

$$\frac{dx}{dt} = V - C \qquad \text{backward characteristic} \qquad (2\text{-}6)$$

where *(V + 2C)* is a constant along the forward characteristic (Equation 2-5) (Chanson 2004). For an observer moving at the absolute velocity *(V + C*), the term *(V + 2C)* appears constant. Similarly *(V - 2C)* appears constant along the backward characteristic (Equation 2-6). The characteristic trajectories are plotted in the (x, t) plane and represent the path of the observers travelling on the forward and backward characteristics. For each forward characteristic, the slope of the trajectory is defined as *1/(V + C)* and *(V + 2C)* and is considered constant along the characteristic trajectory. The characteristic trajectories form contour lines of *(V + 2C)* and *(V - 2C*) (Chanson 2004, Montes 1998). The simple wave equations were applied to the negative and positive surge experiments and the results are discussed in section 5.1 and 6. Rapidly varied unsteady flows in open channels, which are frequently the focus of research studies, include surge waves, stationary or movable hydraulic jumps and dam-break waves.

2.4 Previous experimental research

Positive surges were studied by a number of researchers for over a century. Relevant reviews include, but are not limited to Benjamin and Lighthill (1954), Sander and Hutter (1991), and Cunge (2003). Major contributions were already made early on and included, but are not limited to the following researchers: Barré de Saint Venant (1871), Boussinesq (1877), Lemoine (1948) and Serre (1953). The development of the positive surge front was studied by numerous researchers, such as Tricker (1965), Peregrine (1966), Wilkinson and Banner (1977), Teles Da Silva and Peregrine (1990), Sobey and Dinemans (1992) and Koch and Chanson (2009).

Most experimental studies were limited to visual observations and occasionally free-surface measurements, but rarely encompassed velocity fluctuation measurements. However, there were a few limited studies assessing velocity fluctuation data of positive surges, such as Yeh and Mok (1990), Hornung et al. (1995), Koch and Chanson (2009) and Docherty and Chanson (2010). There are too many experimental research projects focusing on unsteady flows in open channels, to mention, but a selection of the major studies are summarised in Table 2-1.

While there are numerous experimental studies assessing the positive surge propagation, there are only few focused on the negative surge propagation and characteristics (Lauber and Hager 1998, Bazin 1865, Estrade et al.1964, Cavaillé 1965, Dressler 1952).

Dam-break waves are rapidly time variant unsteady flow situations, and research in dam-break waves may be applicable to positive and negative surge research. While this report focuses on the positive and negative surges, the author will also discuss previous research undertaken, on the dam-break wave problem. Most dam- break research was experimental, much like the research on the positive surge. However, theoretical concepts and numerical methods are gaining on importance. Relevant studies include, but are not limited to Schoklitch (1917), Triffonov (1935), De Marchi (1945), Levin (1952), Dressler (1952, 1954) the US Corps of Engineers (1960), Faure and Nahas (1961), Estrande (1967), Rajar (1973), Martin (1983), Menendez and Navarro (1990), Lauber (1997) and Chanson et al. (2000). Table 2-2 lists the main research undertaken in the field of experimental dam-break research.

Table 2-1: Previous experimental research into positive surges and tidal bores

Reference	V_o (m/s)	d_o (m)	Surge type	Channel geometry	Remarks
Positive Surges					
FAVRE (1935) (1)	0	0.106 to 0.206	+ U/S	Rectangular (W = 0.42 m) θ = 0°	Laboratory experiments. Flume length : 73.8 m.
	≠ 0	0.109 to 0.265	+ U/S	Rectangular (W = 0.42 m) θ = 0.017°	
ZIENKIEWICZ and SANDOVER (1957)		0.05 to 0.11	+	Rectangular (W = 0.127 m) θ = 0° Smooth flume : glass Rough flume : wire mesh	Laboratory experiments. Flume length : 12.2 m.
BENET and CUNGE (1971)	0 to 0.198	0.057 to 0.138	+ D/S	Trapezoidal (base width : 0.172 m, sideslope : 2H:1V) θ = 0.021°	Laboratory experiments. Flume length : 32.5 m.
	0.59 to 1.08	6.61 to 9.16	+ U/S	Trapezoidal (base width : 9 m, sideslope : 2H:1V) θ = 0.006 to 0.0086°	Oraison power plant intake channel.
	1.51 to 2.31	5.62 to 7.53	+ U/S	Trapezoidal (base width : 8.6 m, sideslope : 2H:1V)	Jouques-Saint Estève intake channel.
TRESKE (1994)		0.08 to 0.16	+ U/S	Rectangular (W = 1 m) θ = 0.001°	Laboratory experiments. Flume length : 100 m. Concrete channel.
		0.04 to 0.16	+ U/S, + D/S	Trapezoidal (base width : 1.24 m, sideslope : 3H:1V) θ = 0°	Laboratory experiments. Flume length: 124 m. Concrete channel.
CHANSON (1995)	0.4 to 1.2	0.02 to 0.15	+ U/S	Rectangular (W = 0.25 m) θ = 0.19 to 0.54° Glass walls and bed	Laboratory experiments. Flume length : 20 m.
KOCH and CHANSON (2005)	1.0	0.079	+ U/S	Rectangular (W = 0.50 m) θ = 0° PVC invert, glass walls	Laboratory experiments. Flume length : 12 m.
Tidal Bores					
Dee river, LEWIS (1972)	0 to +0.2 m/s	~ 1.4 m	+ U/S	Dee river near Saltney Ferry footbridge. Trapezoidal channel	Field experiments between March and September 1972.

Notes; d_o is the initial water depth; V_o is the initial flow velocity; (1) see also Benet and Cunge (1971). Surge type : + stands for positive surge; - stands for negative surge; U/S stands for moving upstream; D/S stands for moving downstream (adapted from Koch and Chanson 2005).

Table 2-2: Previous experimental investigation into dam break waves

Reference	Slope deg.	Experimental configuration
Schoklitsch (1917)	0	D ≤ 0.25 m, W = 0.6 m D ≤ 1 m, W = 1.3 m
Triffonov (1935)	0.4	L=30m, W=0.4m Initial water depth 300 and 400 mm
Dressler (1954)	0	D = 0.055 to 0.22 m, W = 0.225 m Smooth invert, Sand paper, Slats
Cavaillé (1965)	0	L = 18 m, W = 0.25 m D = 0.115 to 0.23 m, Smooth invert D = 0.23 m, Rough invert
Estrade(1967)	0	L = 13.65 m, W =0.50 m D = 0.2 & 0.4 m, Smooth & Mortar L = 0.70 m, W = 0.25 m D = 0.3 m, Smooth & Rough invert
Faure and Nahas (1961)	$1.2x10^{-4}$	L=40.6 m, W=0.25 m
US Corps of Engineers (1960)	0.5	L=122 m, W=1.22 m Smooth & Rough
Lauber (1997)	0	L < 3.6 m, W = 0.5 m, D < 0.6 m Smooth PVC invert
Chanson et al (2000)	0	L=15 m, W=0.8 m

2.5 Previous numerical research

Fluid motion is controlled by the principles of conservation of mass, energy and momentum. Complex flow situations are solved using empirical approximations, as well as numerical models, which are based on the basic principles, like the Saint-Venant and the Navier-Stokes equations. All models are required to make an approximation to solve the basic principles. Therefore, all models have their limitations. Mathematical models simulating unsteady flows in open channels have been widely used by civil engineers and other professionals. Computer programs are becoming increasingly available to solve unsteady flows in open channels, but their limitations are poorly understood and documented (Toombes and Chanson 2011).

There are a large number of computational models available to model unsteady flow situations in open channels. The models might be categorised into the flowing four categories:

- One-dimensional models (1D)
  One-dimensional models calculate the flow in one direction only. They either solve fully dynamic or simplified forms of conservative or non-conservative one-dimensional, cross-section averaged or shallow water equations (for example the Saint-Venant equations) (Curge and Benet 1971). Even though, the models are simplistic, they are widely applied and useful in many situations (Toombes and Chanson 2011).

- Two-dimensional models (2D)
  They either solve fully dynamic or simplified forms of conservative or non-conservative two-dimensional, shallow water equations. They include 2D horizontal models (Madsen et al. 2005) and 2D vertical models (Lubin et al.2010).

- Coupled (or integrated) 1D-2D models
  They either solve one-dimensional channel flow or two-dimensional overland flow by means of fully dynamic or simplified forms of conservative or non-conservative one- or/and two-dimensional shallow water equations (Altinakar et al. 2009).

- Three-dimensional models (3D)
  Three-dimensional modelling simulates the motion of water in all directions and is believed to most accurately capture flow patterns and velocity fluctuations.

In computational fluid dynamics (CFD), the governing equations are nonlinear and there are a large number of unknown variables. Therefore, implicitly formulated equations are almost always solved using iterative techniques.

To date most commercial software cannot handle rapidly varied unsteady flows, like the positive surge. This might be due to the lack of practically applicable methods. The majority of explicit methods are unsuitable for commercial programs because they require numerical stability, which is expressed by the Courant condition (Zhang and Summer 1994). Several implicit algorithms, like the widely used Preissmann scheme, are generally not valid for a change from subcritical to supercritical flow or conversely (Cunge et al. 1980; Jin and Fread 1997).

Methods of characteristics are one of the first efforts to numerically solve the Saint-Venant equations (Zhang and Summer 1994). Nevertheless, they are rarely used in commercial models because of their complexities and/or the fact that their numerical solutions may breach mass conservation principles. (Stelkoff and Falvey 1993).

In the last few years a number of numerical models aimed at solving the dam-break problems (Soarez et al. 2002). Alcrudo and Soarez (1998) concluded that the shallow water methods agreed adequately with the experimental results. Nevertheless, the mathematical models and numerical solvers are not always adequate in simulating several observed hydraulic characteristics, such as the wave front celerity, that may be misrepresented, as well as the water depth profiles. For example, shortly after the collapse of a gate, the flow is mainly influenced by vertical acceleration due to gravity and the gradually-varied flow hypothesis does not apply (Biscarini et al 2009).

Advances in computer software and hardware technology led to a recent increase in the application of three-dimensional Computational Fluid Dynamics (CFD) models, which are based on the complete set of the Navier Stokes equations. Several studies have been conducted where models have been applied to typical hydraulic engineering cases, like flows over weirs, through bridge piers, pump stations, as well as dam breaks (e.g. Lubin et al. 2010, Furuyama and Chanson 2010, Mohammadi 2008; Nagata et al. 2005, Gomez-Gesteira and Dalrymple 2004; Quecedo et al. 2005; Liang et al. 2007; Biscarini et al 2009).

Most studies use laboratory/field data to validate computational or numerical models. However, laboratory data collected in the majority of cases focuses on the flow depth and does not include velocity and turbulence measurements (Tan and Chu 2010). Tan and Chu (2010) conducted a model validation study, comparing experimental flow depth and velocity data collected by Lauber and Hager (1998), with the outputs of a one-dimensional model based on the Saint-Venant equations. It was concluded that not all of the real effects of the experiments could be reproduced by a one-dimensional model.

Zhang and Summer (1994) assessed the applicability of the implicit method of characteristics (IMOC) built in a computer program called FLORIS to simulate rapidly varied unsteady flows in irregular and nonprismatic open channels. The results showed that the IMOC maintains the mass conservation and provides satisfactory numerical solutions for both subcritical flows and mixed-flow regimes. It was found that the program simulated one-dimensional flows adequately when compared to physical and field data.

Manciola et al. (1994) and De Maio et al. (2004) carried out three-dimensional numerical simulations, where the effects of the gate collapse and the vertical acceleration were demonstrated (Biscarini et al. 2009). Several studies concluded that the dam break flows can be successfully validated using the shallow water equation (Xanthopoulos et al. 1976; Hromadka et al. 1985; Fraccarollo and Toro 1995; Aric`o et al. 2007). While there is an increase in studies focusing on the model validation of the positive surge, no studies know to the author focus on the validation of the modelled negative surge propagation. Numerical methods of negative surges are limited, but have been discussed by Benet and Cunge (1971), Montes (1998), Chanson (2004) and Henderson (1966).

3 Experimental setup

The physical studies of negative and positive surges are performed with models that have similar geometry; therefore, the modelling requires the selection of the appropriate similitude. For the case of a surge propagating in a rectangular, horizontal channel after a sudden and complete gate opening or closing, a dimensional analysis yields:

$$d, V_x, V_y, V_z = F_1(x, y, z, t, d_0, V_0, \delta, B, g, \rho, \mu, \sigma\ldots) \quad (3\text{-}1)$$

where d is the flow depth, V_x, V_y, V_z are the longitudinal, transverse and vertical velocity components at a location (x, y, z), x is the coordinate in the flow direction, y is the horizontal transverse coordinate measured from the flume centerline, z is the vertical coordinate measured from flume bed, t is the time, d_o and V_o are the initial flow depth and velocity, δ is the initial boundary layer thickness at x, B is the channel width, g is the gravity acceleration, ρ and μ are the water density and dynamic viscosity respectively, and σ is the surface tension between air and water layer. Equation (3-1) expresses the unsteady flow properties (left hand side terms) at a point in space (x, y, z) and time t as functions of the initial flow conditions, channel geometry and fluid properties (Reichstetter and Chanson 2011).

Basic considerations show that the relevant characteristic length and velocity scales are correspondingly the initial flow depth d_o and velocity V_o. Equation 3-1 may be reformulated in dimensionless terms:

$$\frac{d}{d_o}, \frac{V_x}{V_o}, \frac{V_y}{V_o}, \frac{V_z}{V_o} = F_2\left(\frac{x}{d_o}, \frac{y}{d_o}, \frac{z}{d_o}, t\sqrt{\frac{g}{d_o}}, \frac{V_o}{\sqrt{g d_o}}, \rho\frac{V_o d_o}{\mu}, \frac{\delta}{d_o}, \frac{B}{d_o}, \frac{g\mu^4}{\rho\sigma^3}, \ldots\right) \quad (3\text{-}2)$$

In Equation (3-2) on the right hand side, the fifth and sixth terms are the Froude and Reynolds numbers in that order, while the ninth term is the Morton number. In a geometrically similar model, a true dynamic similarity is obtained only if each dimensionless parameter has the same value in both model and prototype. In free-surface flows including negative surges, the gravity effects are important and a Froude similitude is commonly used (Henderson 1966, Chanson 1999). This is also the case in this study.

3.1 Experimental facility

New experiments were carried out in the Hydraulic Laboratory at the University of Queensland. A 12 m long and 0.5 m wide horizontal channel was used. The flume was made of smooth PVC bed and glass walls, and waters were supplied by a constant head tank. Photographs of the experimental facility are shown in Figure 3-1.

(a) 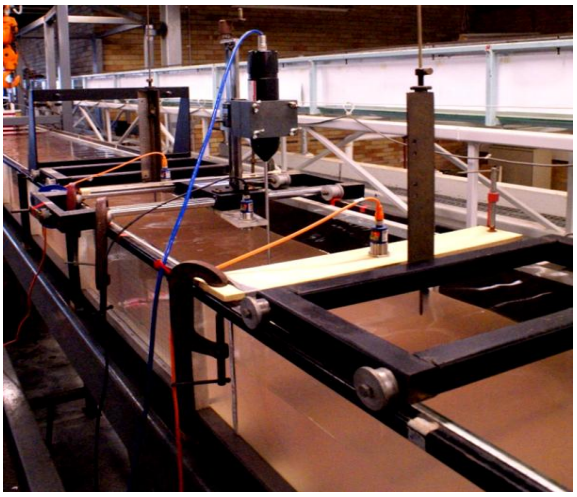

(b) 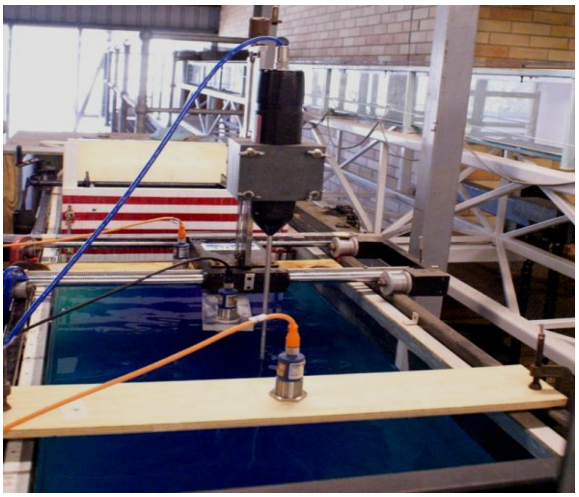

(c) 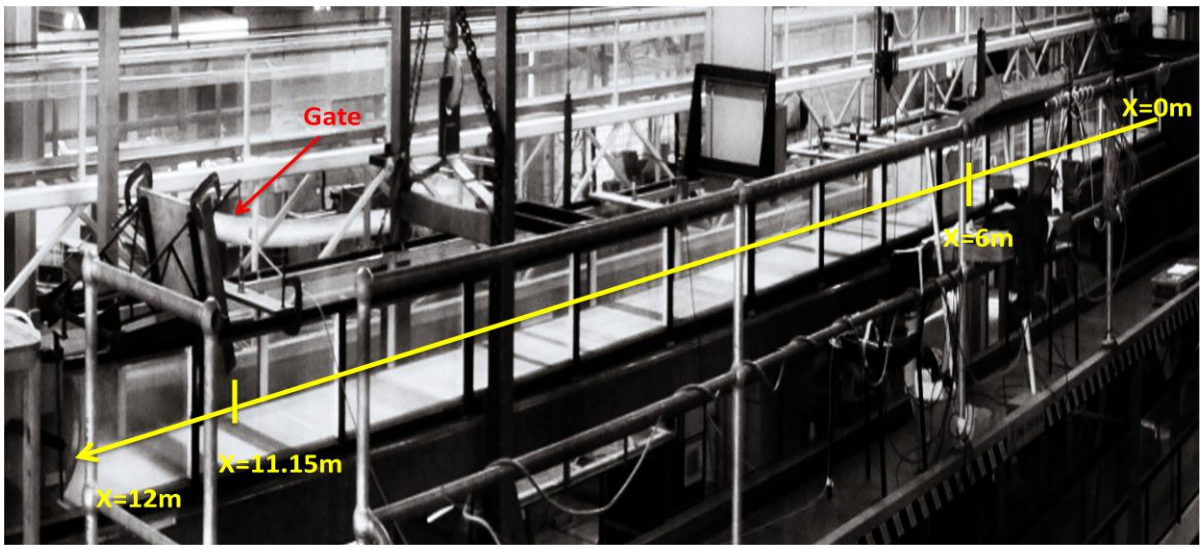

Figure 3-1: Photographs of experimental setup (a) x=6 m, (b) x=10.5 m and (c) x=0-12 m (Courtesy of Prof. Hubert Chanson)

3.2 Instrumentation

The water discharge was measured using orifice meters that were calibrated with a large V-notch weir. The percentage of error was expected to be less than 2%. The analysis of the velocity fluctuations and free surface profile involved more than one instrument, and a reliable synchronization between the devices was needed.

The method used in this study is based upon the analog output of the longitudinal velocity component in the form of a voltage signal from the ADV that is acquired by the data acquisition system (VI Logger, national Instruments) of the acoustic displacement meters.

3.2.1 Free surface measurements using acoustic displacement meters

The water depth was measured using four acoustic displacement meters (Microsonic™ Mic+25/IU/TC and Mic +35/IU/TC units). The Mic+25/IU/TC sensors have an accuracy of 0.18 mm and a response time of 50 ms. The Mic+35/IU/TC sensor has a response time of 70 ms and an accuracy of 0.18 mm.

The acoustic displacement meters emit an acoustic beam into the air that propagates downwards perpendicular to the free surface. The beam is reflected back to the sensor once it hits the air-water interface. From the recorded travel time, the distance between the sensor and water surface is calculated. The sensors were calibrated before each set of experiments. Figure 3-2 shows a typical calibration curve for the four sensors used in the experiments.

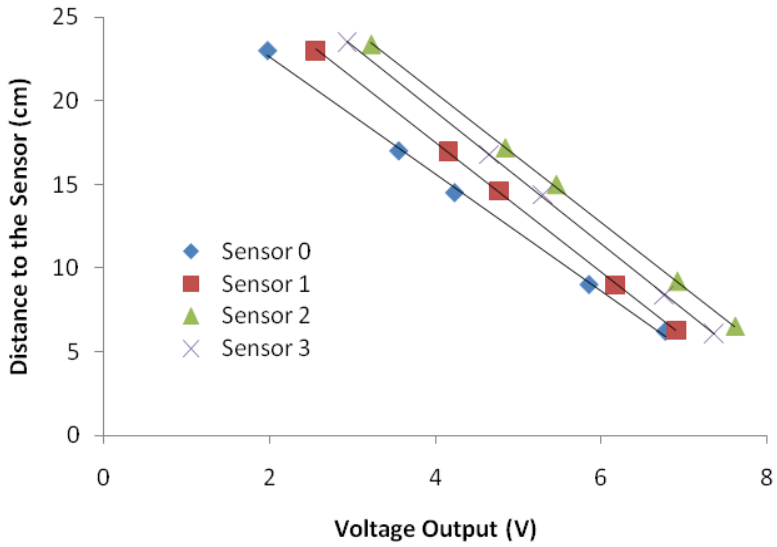

Figure 3-2: Calibration results for the displacement meter measurements

3.2.2 Free surface profile using video imagery

Video imagery was used to record the depth profile and the celerity of the passing surge. A Panasonic™ NV-H30 video camera was used to record the surge at two different locations within the channel.

The first location was near the gate with a full view of the gate to assess the impact of the gate opening and closing on the surge generation and propagation. The second location was at x=6 m. The video movies were recorded at 25 frames per second for the duration of the surge. The camera was placed slightly under the channel surface. The slight angle of the camera was chosen so that the recorded image shows the free surface on the wall and not the surge at the centre of the channel as shown in Figure 3-3. The camera was set back approximately 50 cm from the channel. A 20 mm grid was placed on the side wall of the channel for reference purposes.

Different colour dyes were added to the water to improve the visibility of the free surface in the images. The Panasonic camcorder was connected to a computer via a USB cable.

Two methods of data capture were tested, recording to a miniDV tape and direct computer capture. The videos were imported into Adobe Premiere software, where the movie was split into individual frames for post processing. Each frame was then imported into the DigXY software, and the surface profile data was recorded into an excel spreadsheet.

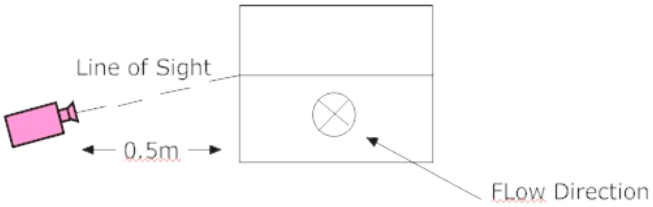

Figure 3-3: Sketch of the video setup

3.2.3 Velocity fluctuations measurements using acoustic Doppler velocimeter (ADV)

The velocity measurements were recorded using an acoustic Doppler velocimeter (ADV) model Nortek™ Vectrino+ (Serial No. VNO 0436) equipped with a three-dimensional side-looking head as shown in Figure 3-4. The velocity range was 1.0 m/s and the sampling rate was 200 Hz. The acoustic displacement meters and the ADV were synchronised and recorded simultaneously at 200 Hz using a high speed data acquisition system NI DAQCard-6024E (maximum sampling rate of 200 Hz).

The translation of the ADV probe in the vertical direction is controlled by a fine adjustment travelling mechanism connected to a Mitutoyo™ digimatic scale unit. The error of the vertical position of the probe is $\Delta z<0.025$ mm.

The accuracy on the longitudinal position is estimated as ∆x<+/- 2 mm. The accuracy on the traverse position of the probe is less than 1 mm. All the measurements were taken on the centreline of the channel.

(a) ADV head above the free-surface during a fixed gravel bed experiment (Docherty and Chanson 2010)

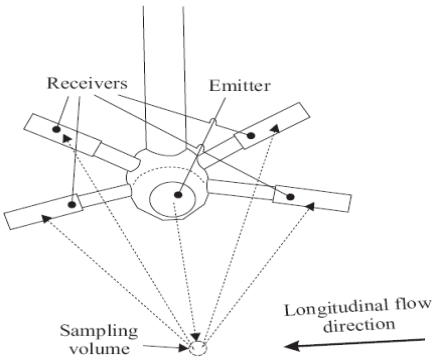

(b) Sketch of the NortekTM ADV side-looking head (Docherty and Chanson 2010)

Figure 3-4: Acoustic Doppler velocimeter (ADV)

The ADV measurements were recorded by measuring the velocity of particles in a remote sampling volume, which is based upon the Doppler shift effect (e.g. Voulgaris and Trowbridge 1998; McLelland and Nicholas 2000). With each sample recording the ADV measured four values, the velocity component, the signal strength value, the correlation value and the signal to-noise ratio. Research showed that there are many problems with the recordings, because the signal outputs combine the effects of velocity fluctuations, Doppler noise and other disturbances (Lemmi and Lhermitte 1999; Goring and Nikora 2002; Chanson et al. 2008). Past experience demonstrated recurrent problems with the velocity data, including low correlations and low signal-to-noise ratios (Chanson 2008).

To eliminate noise some clay powder was added to the channel before and during ADV recordings. Further problems were experienced with boundary proximity, but could not be eliminated.

There are a number of ADV post-processing techniques for steady flows (e.g. Goring and Nikora 2002; Wahl 2003). The post processing of the ADV data was carried out using the software WinADV^{TM} version 2.025 as documented in Koch and Chanson (2009) and Docherty and Chanson (2010). For the ADV post-processing of steady flows, communication errors, average signal to noise ratio data less than 5dB and average correlation values less than 60% were removed. Also, the phase-space thresholding technique developed by Goring and Nikora (2002) was applied to remove spurious points in the ADV steady flow data set. However, it was found that the above mentioned post-processing techniques do not apply in unsteady flow conditions (e.g. Koch and Chanson 2009). Thus, the unsteady flow post-processing was limited to the removal of communication errors. It was noted that the vertical velocity component V_z data may be affected adversely by the bed proximity (Chanson 2010).

3.2.4 Experimental procedure and flow conditions

Two main series of measurement were conducted. The first series aimed to study the free surface properties using video imagery and acoustic displacement meters. The second series was related to the velocity fluctuation analysis using an ADV. During the second series the depth measurements recording continued using only the acoustic displacement meters. During the first series various discharges and gate openings were recorded. The experimental flow conditions are listed in Table 3-1.

Two layouts for the depth and velocity measurements were selected and recorded at 200 Hz for both negative and positive surges. For configuration one the velocity was recorded near the gate at x=10.5 m, while the depth measurements were measured at, x=10.8 m, 10.5 m, 10.2 m and 6 m. Figure 3-5 (a) presents a sketch of configuration one illustrating a negative surge. For configuration two the velocity was recorded at 6 m, while the depth measurements were taken at x=10.8 m, 6.2 m, 6 m and 5.6 m. Figure 3-5(b) presents a sketch for configuration two picturing a positive surge. The ADV measurements were taken at four different vertical elevations, at z=6.69 mm, 25.01 mm, 123.94 mm and 135.2 mm. Twenty-five positive and negative surges runs were recorded for each of the four vertical ADV locations.

The positive and negative surges were produced using a tainter gate. The tainter gate was located next to the downstream end (x=11.15 m) where x is the distance from the channel upstream end. The gate was constructed to allow for different opening settings by moving the plate upwards and downwards. The gate was operated manually and the opening times were recorded by video and sound recordings. The negative and positive surges were produced respectively by opening and closing rapidly the tainter gate and the opening and closing times were less than 0.2 s.

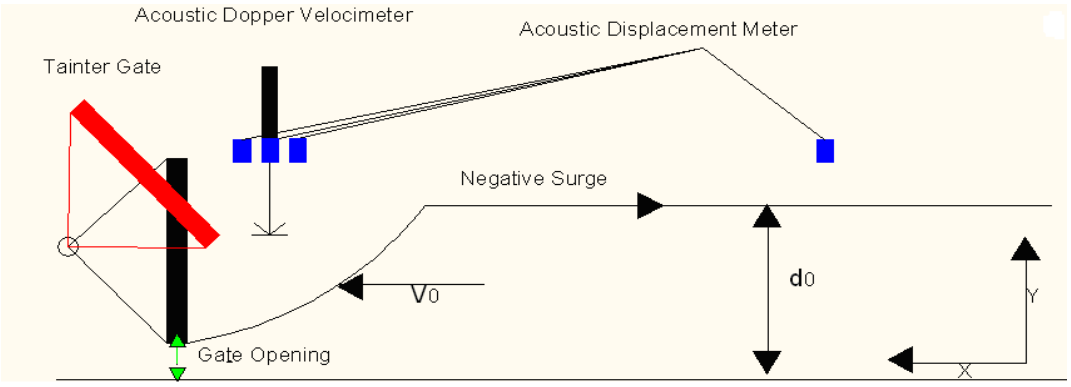

(a) x=10.5 m

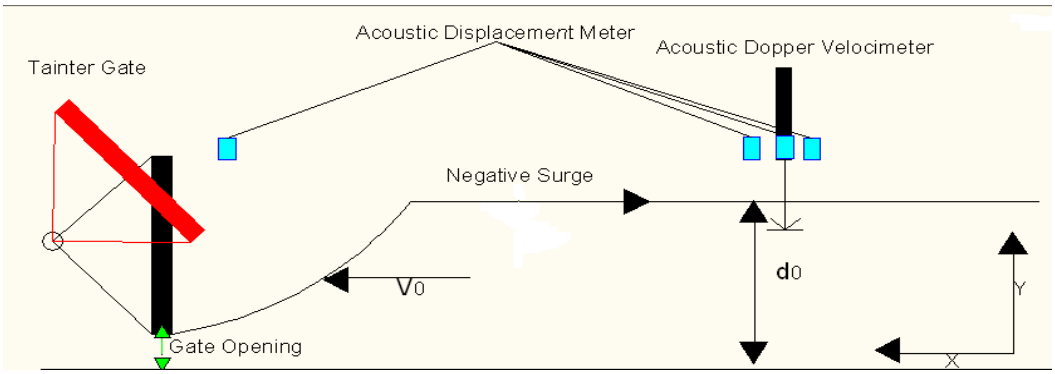

(b) x=6 m

Figure 3-5: Sketch of experimental set-up with ADV

Table 3-1: Experimental flow conditions for turbulent velocity measurements

Instrumentation	Type of surge	Location	Discharge (l/s)	Gate opening
Video	Negative	x=10.5 m	20	30
				50
			30	40
				50
		x=6 m	20	30
				50
			30	40
				50
	Positive (undular)	x=10.5 m	20	30
				50
			30	40
				50
		x=6 m	20	30
				50
			30	40
				50
ADM	Negative	x=10.8 m	20	30
		x=10.5 m		
		x=10.2 m		
		x=6 m		
		x=6.2 m		
		x=5.6 m		
	Positive (undular)	x=10.8 m	20	30
		x=10.5 m		
		x=10.2 m		
		x=6 m		
		x=6.2 m		
		x=5.6 m		
ADV	Negative	x=10.5 m, z=6.69, 25.01, 123.94, 135.2 mm	20	30
		x=6 m, z=6.69, 25.01, 123.94, 135.2 mm		
	Positive (undular)	x=10.5 m, z=6.69, 25.01, 123.94, 135.2 mm	20	30
		x=6 m, z=6.69, 25.01, 123.94, 135.2 mm		

4 Experimental results

The coordinate system was selected with x representing the longitudinal coordinate and the y axis representing the water depth. The initial water depth is characterized by d_0, while d is the water depth at time t. The celerity of a small disturbance is symbolised by C and V stands for the velocity in the x direction. In section 4.1 the ADV results are presented and discussed. The results of the video analysis are outlined in section 4.2 and in section 4.3 the results of the ensemble-average are illustrated and analysed.

Some instantaneous velocity measurements were performed with an ADV at four vertical elevations. The data were sampled at 200 Hz on the centreline near the gate at x=10.5 m and further upstream at x=6 m. For configuration one the velocity was recorded near the gate at x=10.5 m, while the depth measurements were taken at, x=10.8 m, x=10.5 m, x=10.2 m and x=6 m. For configuration two the velocity was recorded at 6 m, while the depth measurements were taken at x=10.8 m, x=6.2 m, x=6 m and x=5.6 m. The experimental flow conditions for the turbulent velocity measurements for the ADV and ADM are summarised in Table 4-1.

Table 4-1: Steady state experimental flow conditions for ADV and ADM measurements

(Q) (l/s)	Gate opening (mm)	Type of surge	Instrumentation	V_0 (m/s)	d_0 (m)	Location (x) (m)
20	30	Negative	ADV, ADM	0.18	0.22	10.8, 10.5, 10.2, 6.2, 6, 5.6
		Positive	ADV, ADM	0.625	0.064	10.8, 10.5, 10.2, 6.2, 6, 5.6

4.1 Acoustic Doppler velocimeter and acoustic displacement meter results

4.1.1 Negative surge

Figures 4.1 and 4.2 present some typical results in the form of instantaneous dimensionless flow depth d/d_o as a function of dimensionless time from gate closure $t \times \sqrt{g / d_0}$, where d_o is the initial water depth at x=6 m and x=10.5 m respectively.

The instantaneous velocity components V_x, V_y and V_z were positive downstream, towards the left side wall and upwards respectively.

The negative surges had an average initial water depth of d_0=0.22 m and an average initial velocity of V_0=0.1766 m/s. The velocities were sampled at vertical elevations of z=6.69 mm, z=25.01 mm, z=123.94 mm and z=135.2 mm and at horizontal locations at x=6 m and x=10.5 m. The data of z=25.01 mm at x=6 m were excluded in the analysis due to instrumentation failure. Most velocity measurements, close to the gate, presented a spike before the surge developed, which might be related to the rapid gate opening. There were increased velocity fluctuations in the vertical velocity component V_z data shortly after the surge formation in all the reported cases. The longitudinal velocity V_x data were closely linked with the depth profile. The transverse velocity component V_y showed little fluctuations before, during and after surge formation.

The surface water profiles at the gate showed a steeper drop in water depth close to the gate (e.g. x=10.8 m) compared to the observations further upstream at x=6 m (Figures 4-1 and 4-2). Generally, the water depth decreased gradually after the initial surge formation at x=6 m. The free surface measurements showed some marked curvature near the surge leading edge. The longitudinal velocity component increased at the same time as the water depth decreased. The velocity measurements at x=6 m showed some higher fluctuations during the initial phases of the surge propagation. The increase of velocity fluctuations observed during the negative surge propagation might indicate some turbulent mixing.

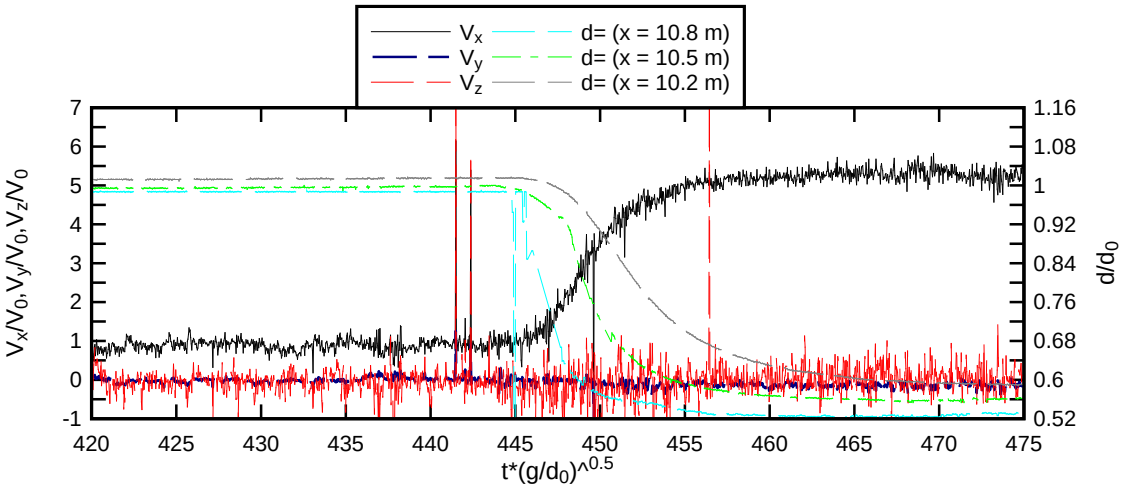

(a) x=10.5 m, z=6.69 mm, Q=20 l/s, d_0=0.22 m and initial gate opening 30 mm

Figure 4-1: Dimensionless instantaneous velocity and depth measurements of a negative surge at x=10.5 m (cont'd)

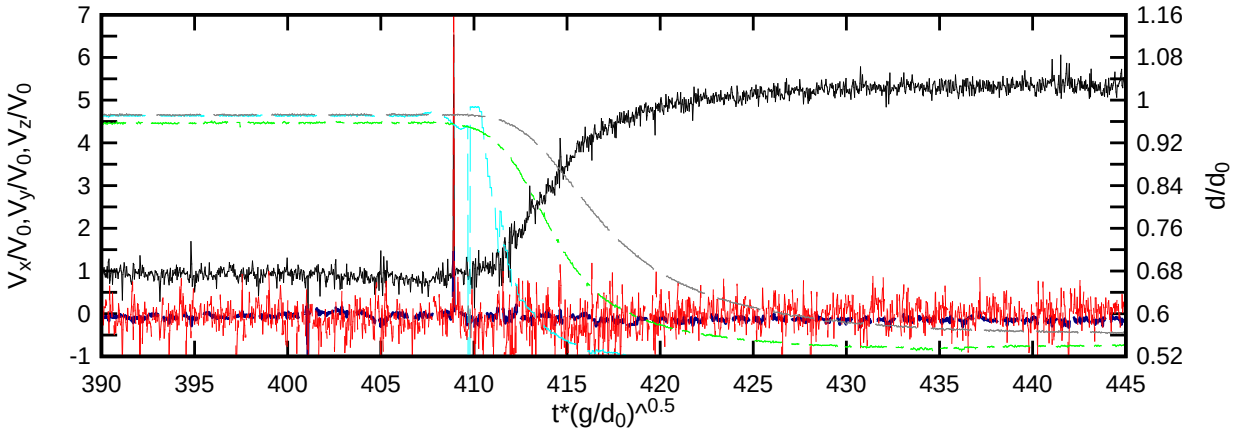

(b) x=10.5 m, z=25.01 mm, Q=20 l/s, d_0=0.22 m and initial gate opening 30 mm

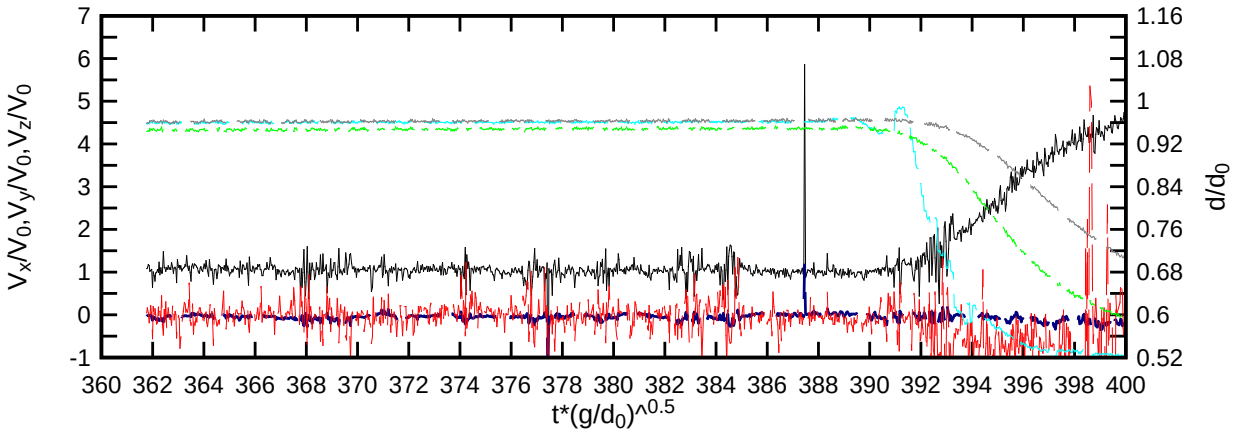

(c) x=10.5 m, z=123.94 mm, Q=20 l/s, d_0=0.22 m and initial gate opening 30 mm

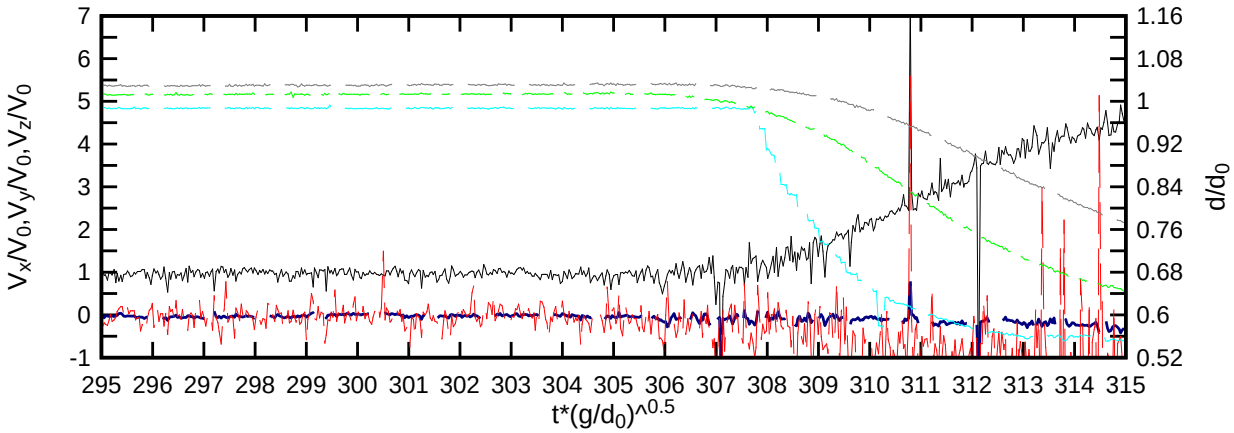

(d) x=10.5 m, z=135.2 mm , Q=20 l/s, d_0=0.22 m and initial gate opening 30 mm

Figure 4-1: Dimensionless instantaneous velocity and depth measurements of a negative surge at x=10.5 m

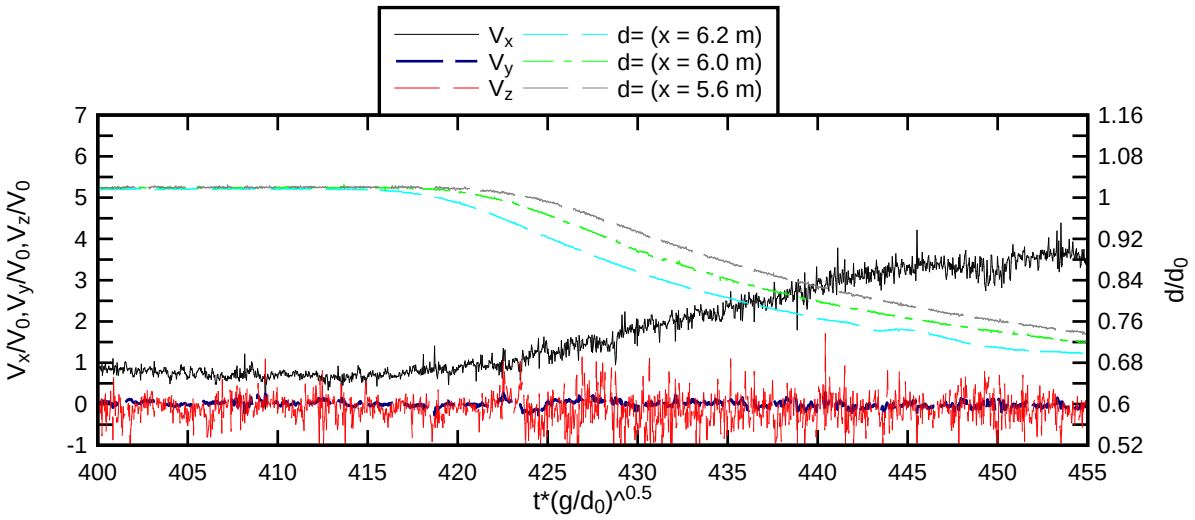

(a) x=6 m, z=6.69 mm, Q=20 l/s, d_0=0.22 m and initial gate opening 30 mm

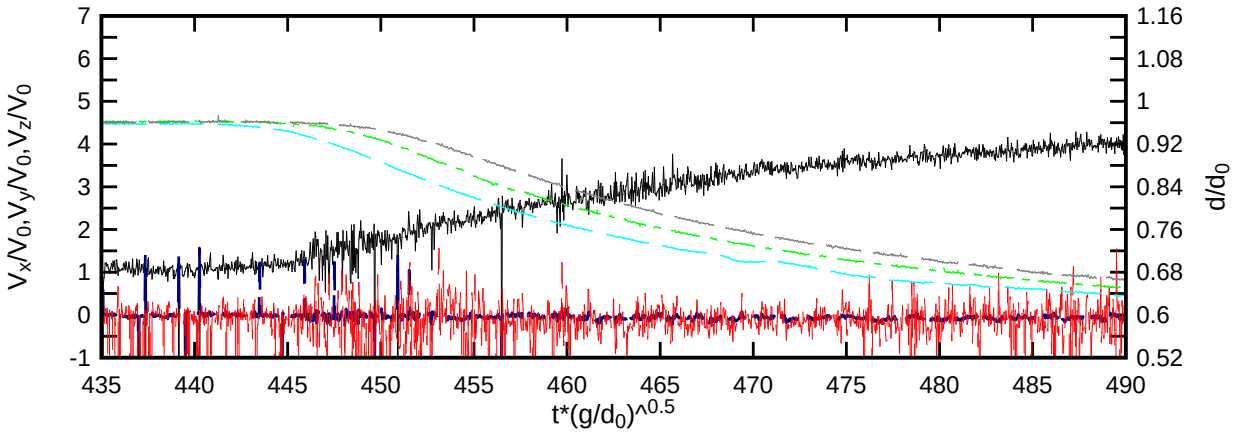

(b) x=6 m, z=123.94 mm, Q=20 l/s, d_0=0.22 m and initial gate opening 30 mm

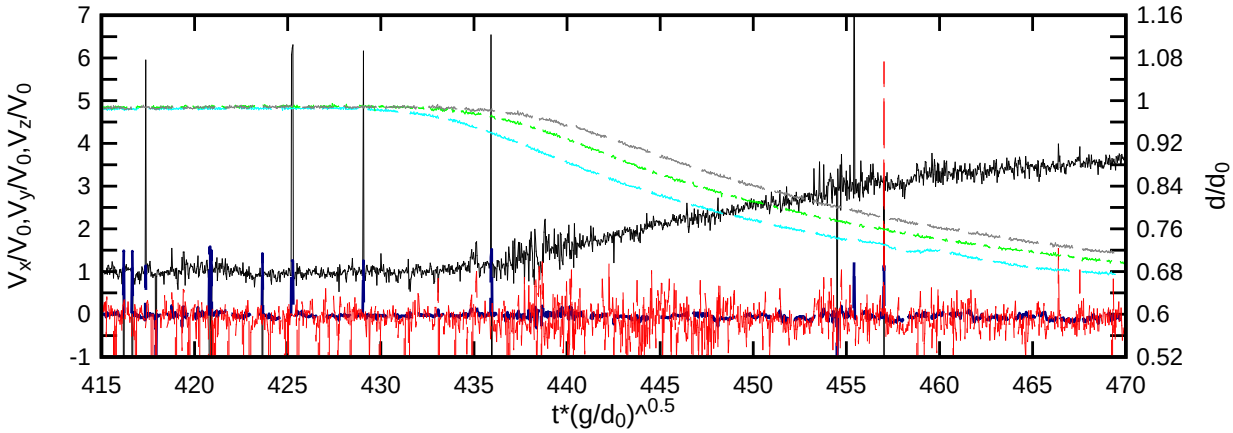

(c) x=6 m, z=135.2 mm, Q=20 l/s, d_0=0.22 m and initial gate opening 30 mm

Figure 4-2: Dimensionless instantaneous velocity and depth measurements of a negative surge at x=6 m

4.1.2 Positive surge

The positive surges had an average initial water depth of d_0=0.064 m and an average initial velocity of V_0=0.625 m/s. Typical instantaneous free-surface profiles and ADV velocity recordings for the positive surges are presented in Figures 4-3 and 4-4. The data of z=25.01 mm at x=6 m were excluded in the analysis due to instrumentation failure.

The figures are presented in instantaneous dimensionless flow depth d/d_o as a function of dimensionless time from gate closure $t \times \sqrt{g / d_0}$, where d_o is the initial water depth at x=6 m and x=10.5 m respectively. The acoustic displacement meter output was a function of the strength of the acoustic signal reflected by the free-surface. When the free-surface was not horizontal, some erroneous points were recorded. These were relatively isolated and easily identified. Overall the data showed a gradual evolution of the positive surge shape as it propagated upstream (e.g. from x=10.8 m to x=6 m) (Figure 4-3). The data suggested a slight reduction in surge height with increasing distance from the downstream gate. Figure 4-3(a) shows the positive surge propagation at x=6 m. A decrease in the V_x velocity component can be observed in the initial phase of the positive surge. The V_y and V_z velocity components did not show any major change in pattern between the steady state phase and the propagation of the positive surge. Significant V_z spikes were observed near the gate as seen in Figure 4-4 (b) and (c).

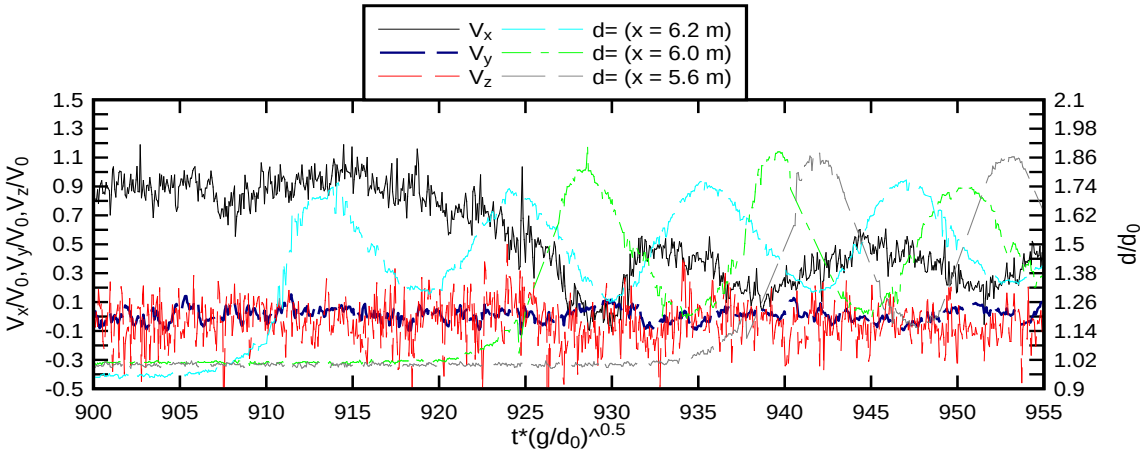

(a) x=6 m, z=6.69 mm, Q=20 l/s, d_0=0.064 m and initial gate opening 30 mm

Figure 4-3: Dimensionless instantaneous velocity and depth measurements of a positive surge at x=6 m

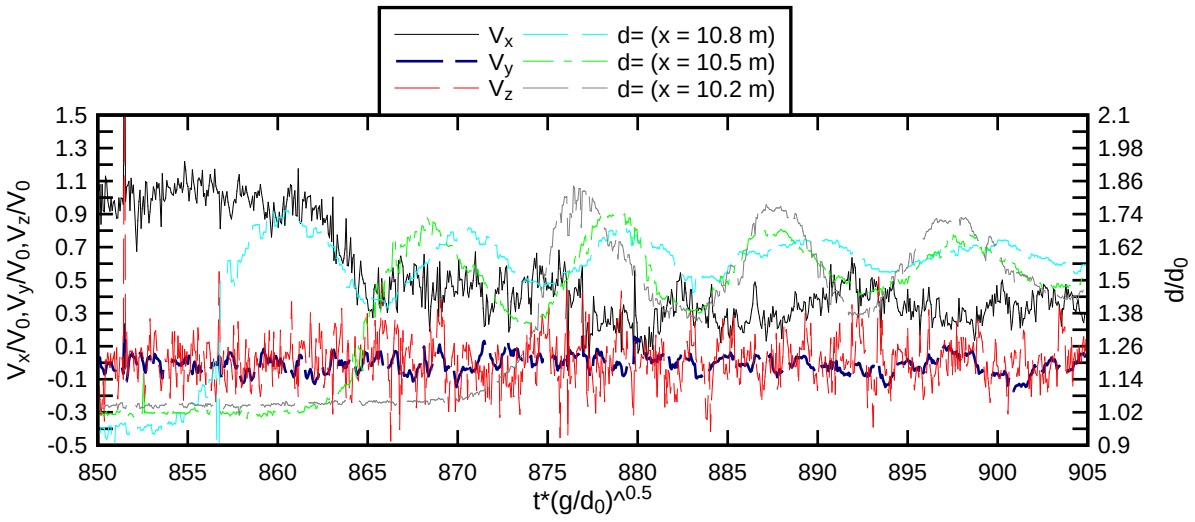

(a) x=10.5 m, z=6.69 mm, Q=20 l/s, d_0=0.064 m and initial gate opening 30 mm

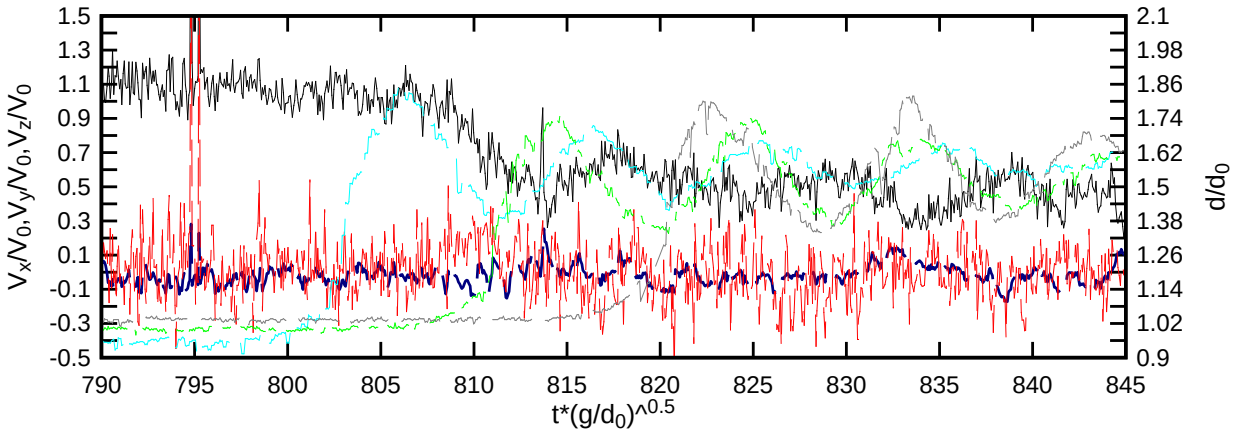

(b) x=10.5 m, z=123.94 mm , Q=20 l/s, d_0=0.064 m

Figure 4-4: Dimensionless instantaneous velocity and depth measurements of a positive surge at x=10.5 m

4.2 Video analysis results

Video imagery was used to record the surface profile of the positive and negative surges. The surface profiles of the propagation of the positive and negative surges were analysed at 6 m and at 10.8 m. The video imagery was analysed frame by frame, with 25 frames per second from the first opening or closing of the gate. A summary of the experimental flow conditions is provided in Table 4.2. Photographs of a positive and negative surge are shown in Figure 4-5.

(a) 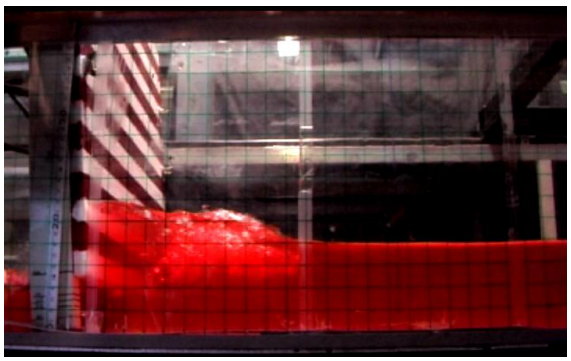 (b) 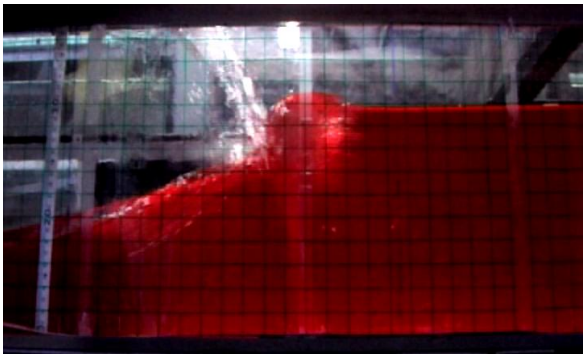

Figure 4-5: Photos of (a) positive and (b) negative surge near the gate at (11.2 m< x <10.48 m)

Table 4-2: Experimental flow conditions for water surface measurements using video analysis

Discharge (Q) (l/s)	Gate opening (mm)	Type of surge	V_0 (m/s)	d_0 (m)	Location (x) (m)
20	30	Negative	0.167	0.24	6, 10.5
		Positive	0.667	0.06	6, 10.5
	50	Negative	0.400	0.10	6, 10.5
		Positive	0.667	0.06	6, 10.5
30	40	Negative	0.231	0.26	6, 10.5
		Positive	0.750	0.08	6, 10.5
	50	Negative	0.273	0.22	6, 10.5
		Positive	0.857	0.07	6, 10.5

4.2.1 Negative surge

The results are illustrated in dimensionless water depth and dimensionless distance x within the recorded frame. Each curve represents the time step for one frame, with a recording speed of 25 frames per second. The results are presented in Figure 4-6 at x=10.5 m and Figure 4-7 at x=6 m. The results close to the gate at x=10.5 m showed, that the flow pattern is very similar regardless of the initial gate opening and discharge. Due to the gate opening there is an initial rise at the beginning of the surge with a slow and steady fall of the water surface elevation. The water depth decreases faster at the beginning of the surge compared to the later stages of the surge. At 6 m the water surface has no curvature anymore. It was observed that the negative surge with Q= 20 l/s and a 50 mm gate opening showed the lowest variation in water depth between each frame. A slight curvature was observed at the dimensionless distance x'/d_0=1.25 in the results of the negative surge at x=6 m with a 30 l/s discharge and a 50 mm gate opening. Overall, the video data provided a good illustration of the water depth profile, showing the propagation of the negative surge as a gradual lowering of the water surface.

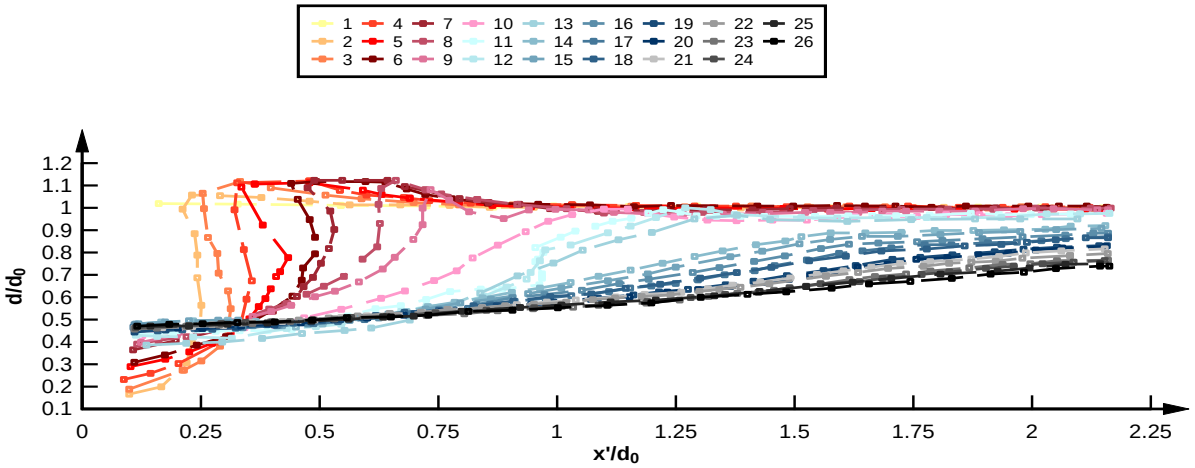

(a) Q=20 l/s and 30 mm gate opening

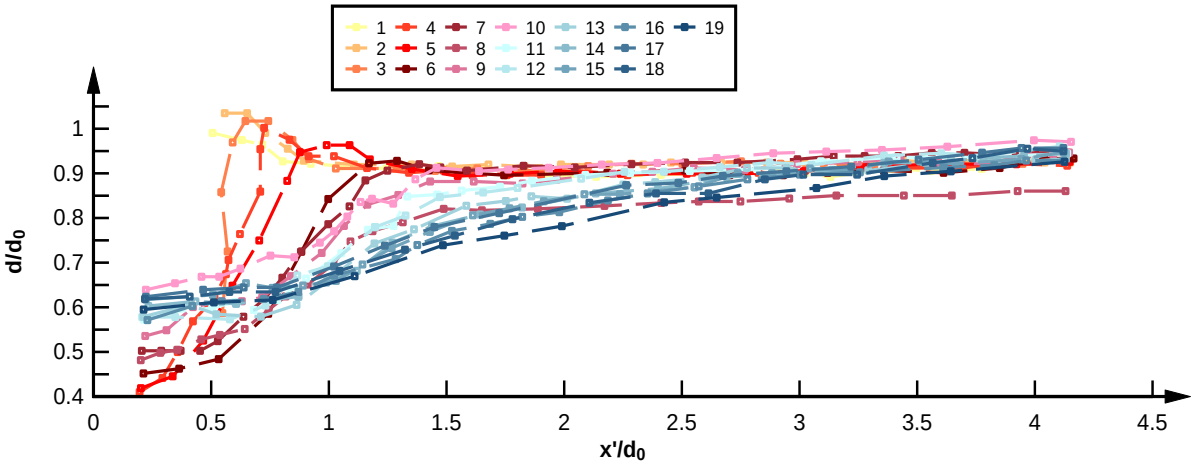

(b) Q=20 l/s and 50 mm gate opening

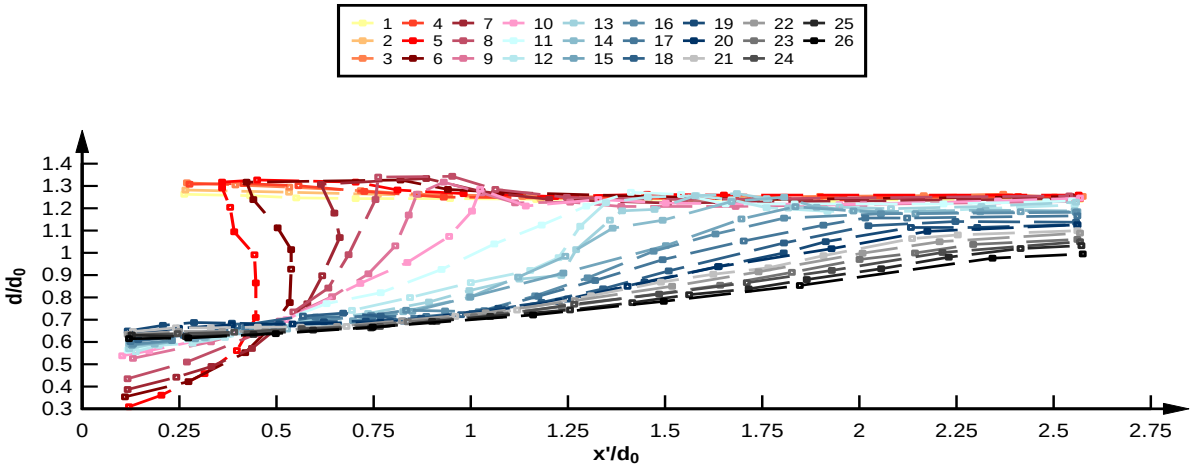

(b) Q=30 l/s and 40 mm gate opening

Figure 4-6: Dimensionless video data for the negative surge immediately u/s of the gate 10.5 m, with x'=0 corresponding to x=11.2 m (cont'd)

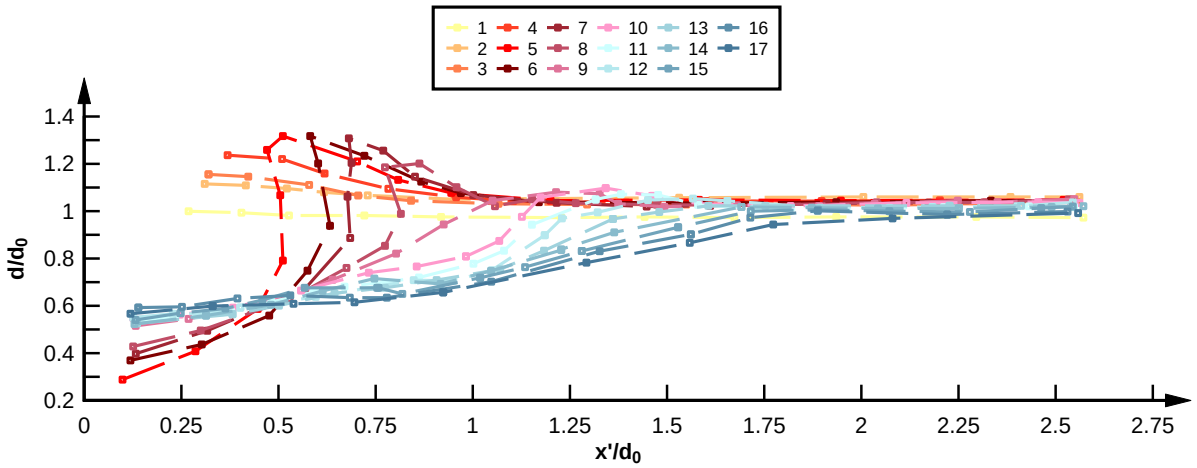

(d) Q=30 l/s and 50 mm gate opening

Figure 4-6: Dimensionless video data for the negative surge immediately u/s of the gate 10.5 m, with x'=0 corresponding to x=11.2 m

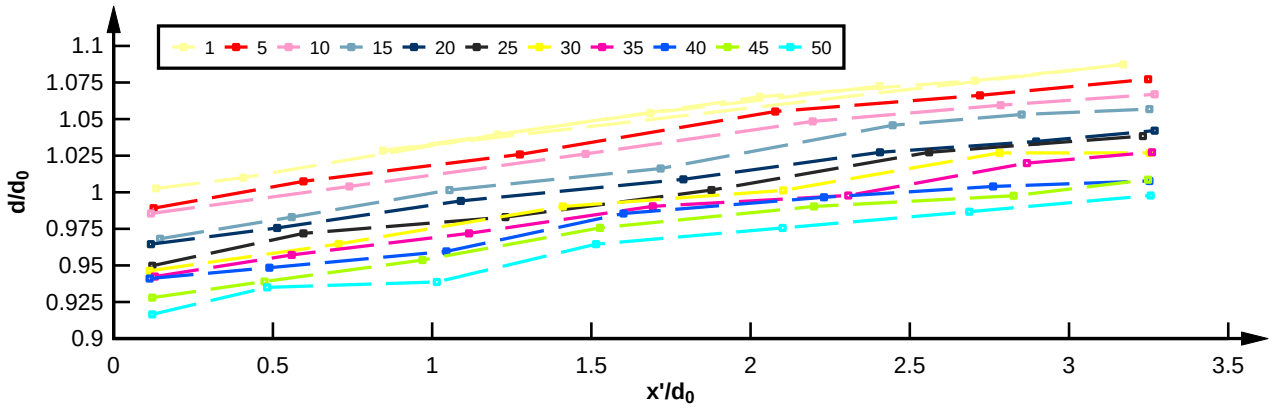

(a) Q=30 l/s and 50 mm gate opening

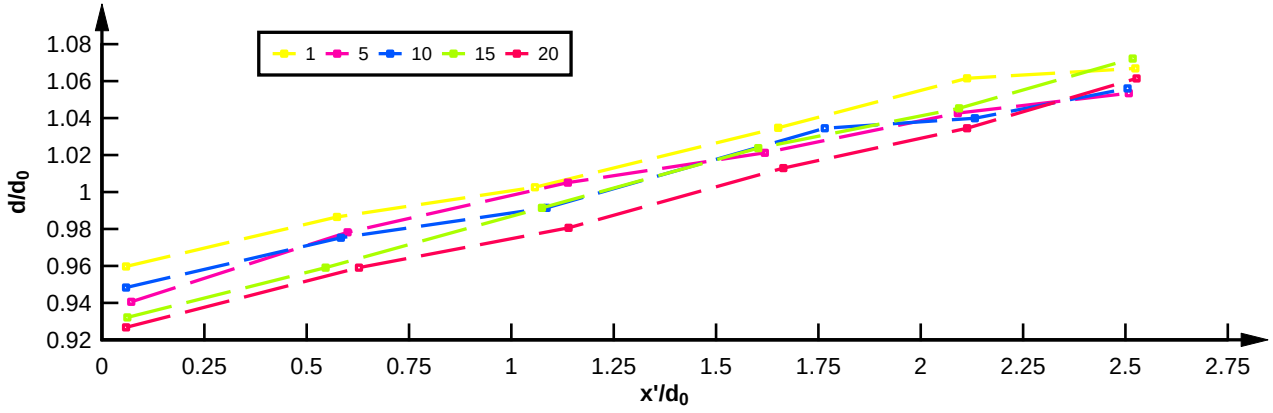

(b) Q=20 l/s and 50 mm gate opening

Figure 4-7: Dimensionless video data for the negative surge at 6 m, with x'=0 corresponding to x=6.3 m (cont'd)

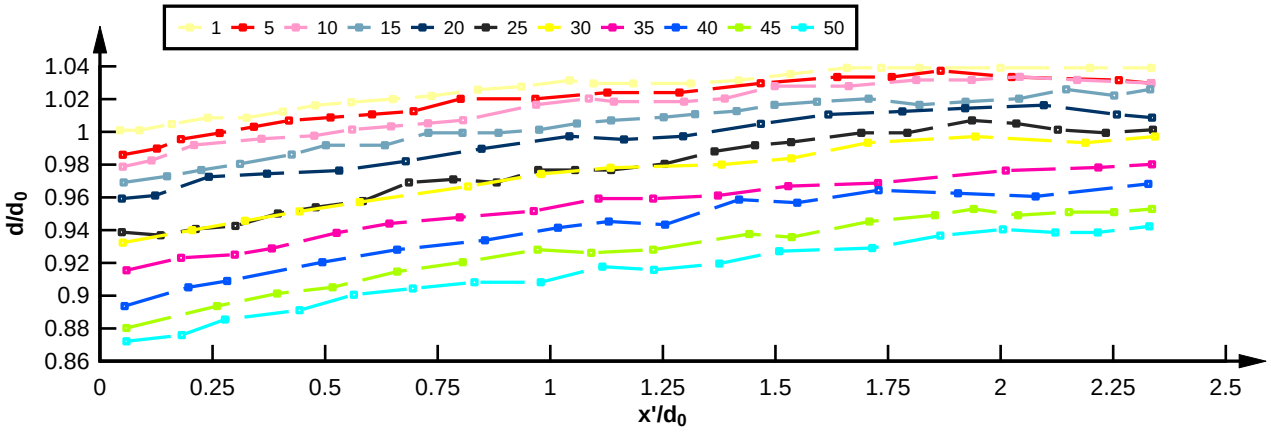

(c) Q=30 l/s and 40 mm gate opening

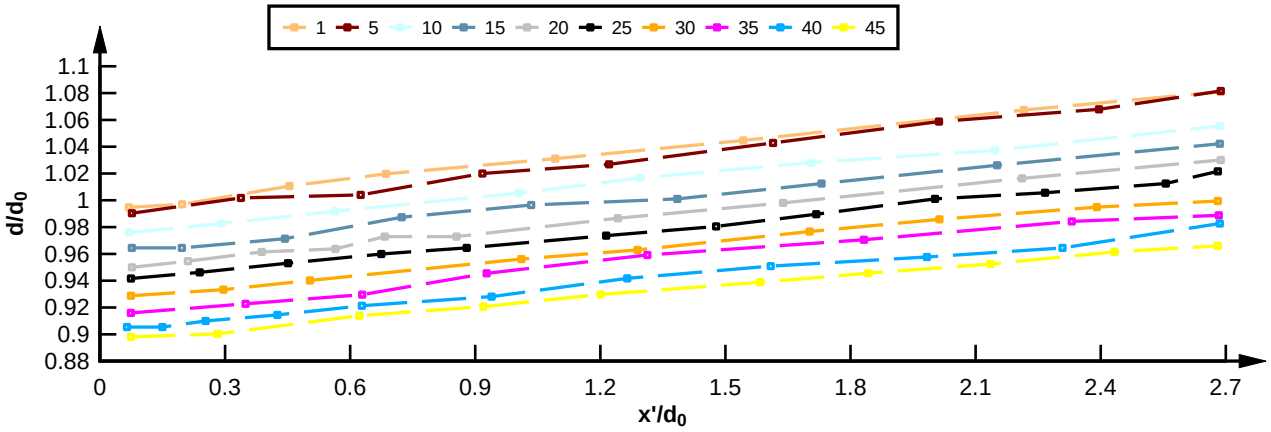

(d) Q=20 l/s and 30 mm gate opening

Figure 4-7: Dimensionless video data for the negative surge at 6 m, with x'=0 corresponding to x= 6.3 m

4.2.2 Positive surge

The results are illustrated in dimensionless water depth and dimensionless distance x within the recorded frame. The first frame corresponded to the start of the gate opening. The results are presented for the positive surge in Figure 4-8 at x=10.5 m and Figure 4-9 at x=6 m. The curves are plotted for each frame with a 25 frames per second camera speed. The positive surge video analysis showed that there is a difference in surge propagation and water depth with different discharge conditions and initial gate openings.

The results of the experiments performed with a discharge of 20 l/s and a gate opening of 50 mm showed that the surge propagates slower than the surge in the other experiments.

The increase in water depth can be best observed at the beginning of the surge formation. After a quick initial rise in water depth the water surface rose gradually until it came to a steady state.

The surface profiles of the positive surge were similar for both observed locations, x=10.5 m and x=6 m. The water depth at x=6 m showed the steady propagation of the surge front with a rise of approximately 0.2 d/d_0 between the initial conditions and the water depth at frame 32 (Δt=1.28 s).

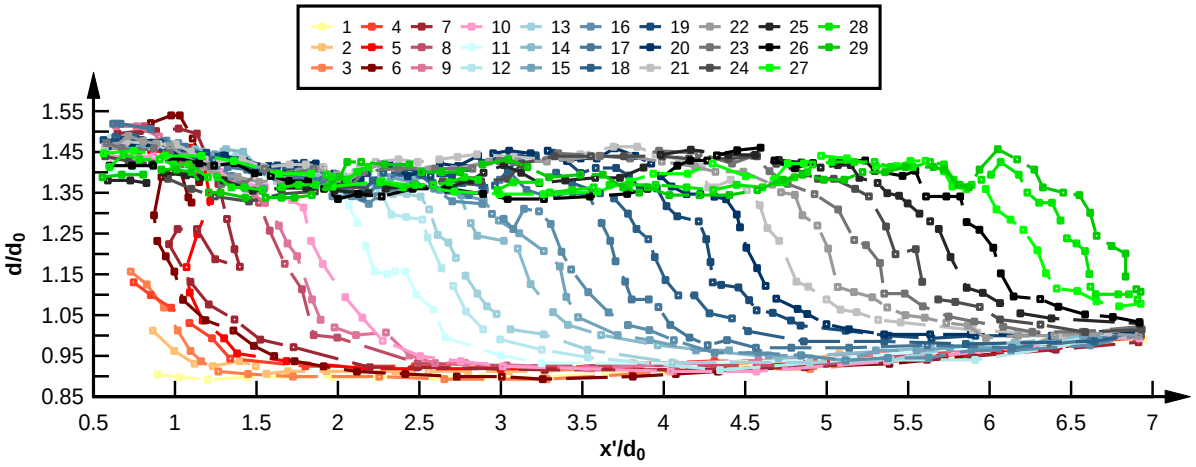

(a) Q=20 l/s and 30 mm gate opening

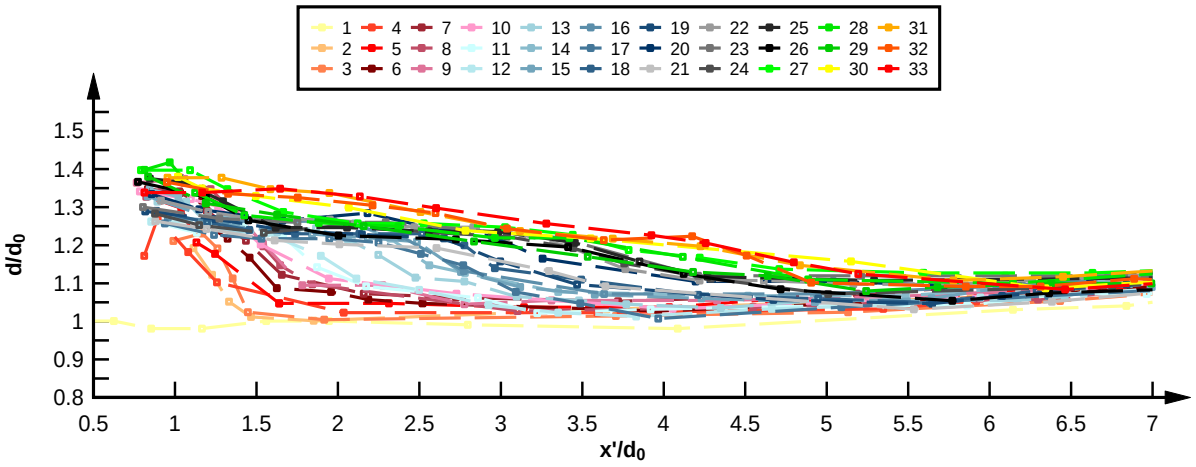

(b) Q=20 l/s and 50 mm gate opening

Figure 4-8: Dimensionless video data for the positive surge at 10.5 m, with x'=0 corresponding to x=11.2 m (cont'd)

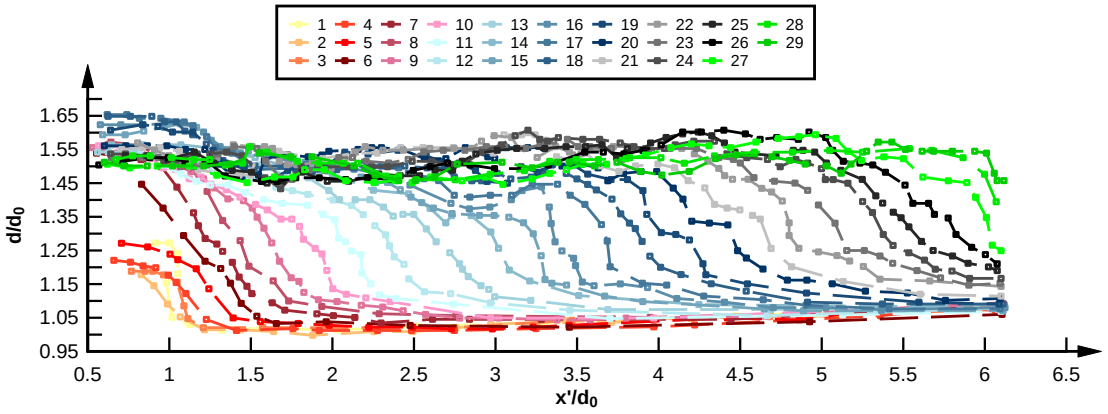

(c) Q=30 l/s and 40 mm gate opening

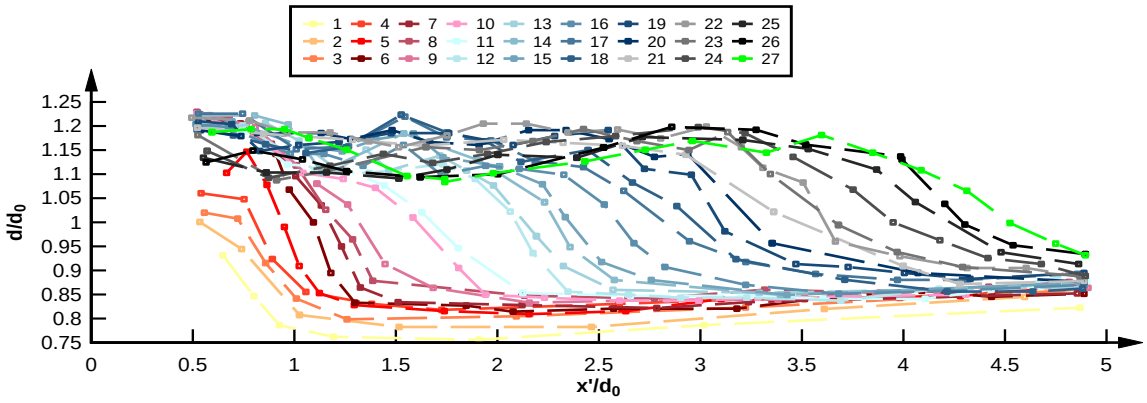

(d) Q=30 l/s and 50 mm gate opening

Figure 4-8: Dimensionless video data for the positive surge at x= 10.5 m, with x'=0 corresponding to x=11.2 m

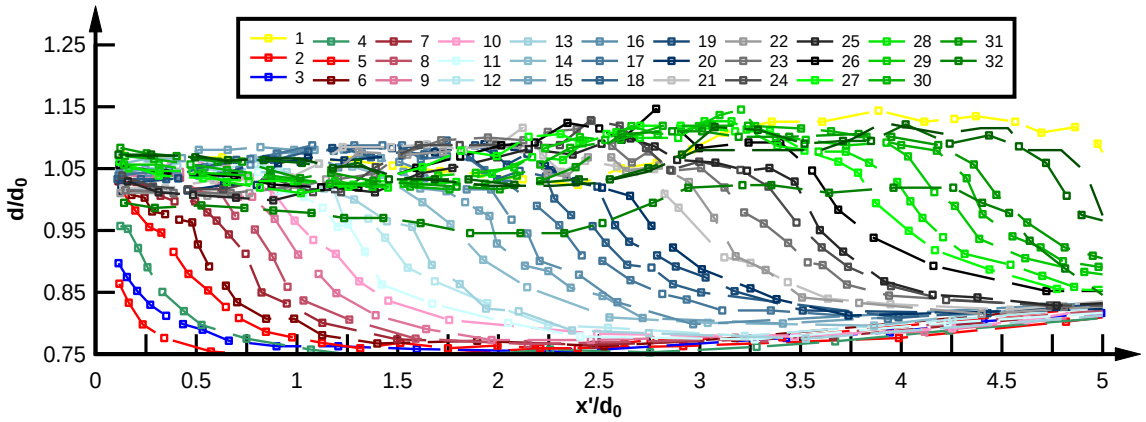

(a) Q=20 l/s and 30 mm gate opening

Figure 4-9: Dimensionless video data for the positive surge at x= 6 m, with x'=0 corresponding to x=6.9 m (cont'd)

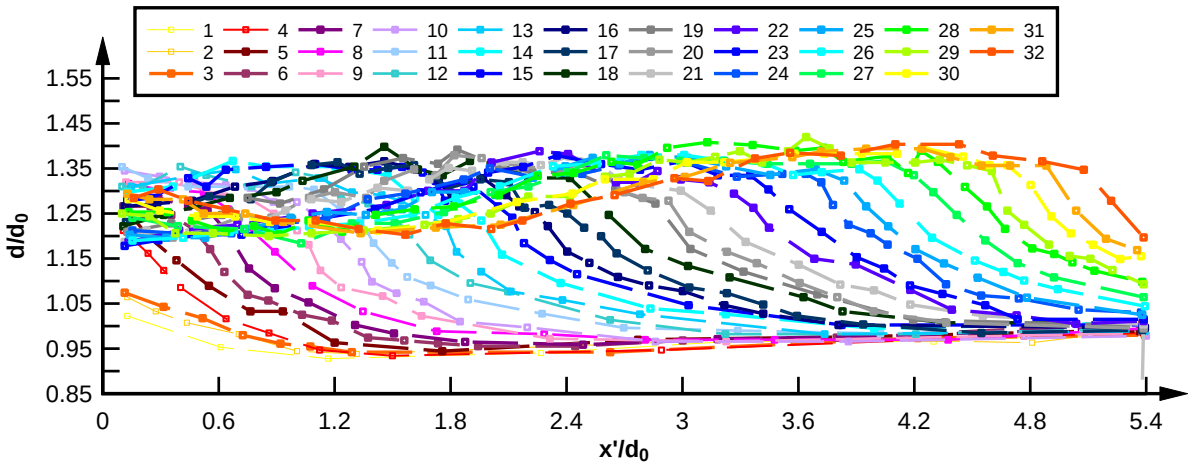

(b) Q=30 l/s and 40 mm gate opening

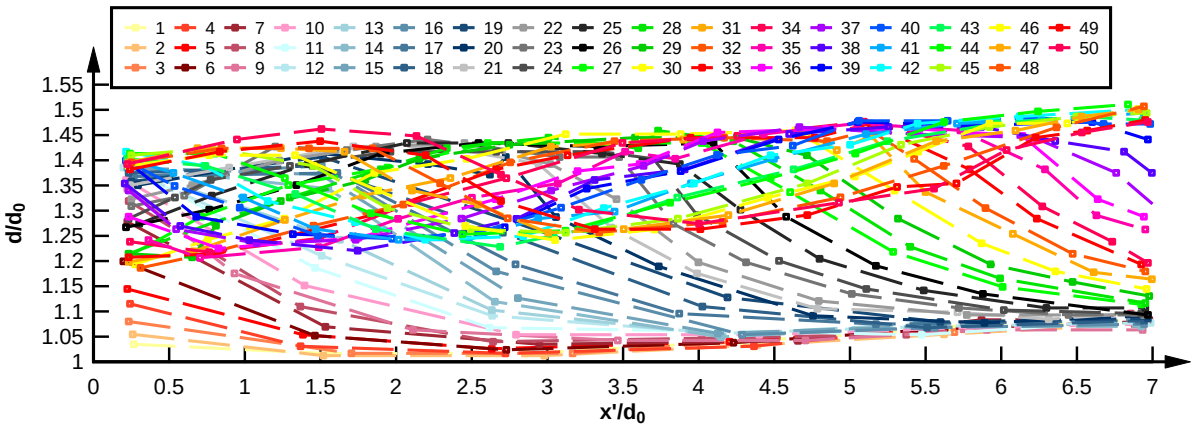

(c) Q=30 l/s and 50 mm gate opening

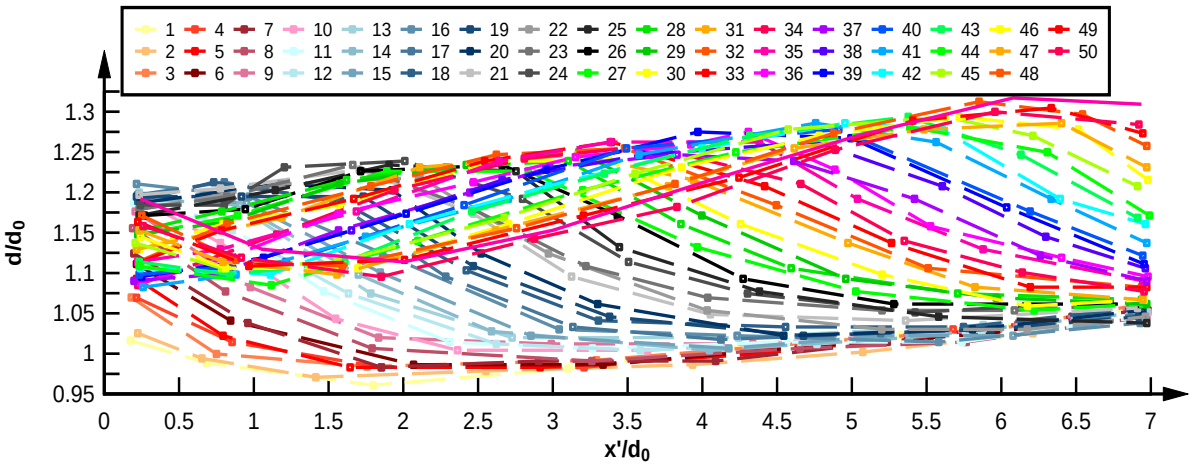

(d) Q=20 l/s and 50 mm gate opening

Figure 4-9: Dimensionless video data for the positive surge at x=6 m, with x'=0 corresponding to x=6.9 m

4.3 Ensemble-average results

In a turbulent unsteady flow, the analysis of the time average data is not meaningful, because the hydrodynamic shock and the short-term fluctuation must be analysed independently. Therefore, the experiments were repeated several times to obtain an ensemble average of the instantaneous data. For both negative and positive surges the free-surface properties and velocity characteristics were systematically investigated at x=10.5 m and x=6 m. A total of 25 runs were conducted for the two layouts and four vertical elevations of the ADV. The data was analysed and scattered runs were eliminated. The remaining runs, typically 20 runs or greater, were ensemble-averaged.

4.3.1 Negative surge

Figures 4-10 shows some typical synchronised dimensionless data of the instantaneous water depth, velocities, as well as the median water depth and median velocities for the negative surge. An ensemble-median of each instantaneous velocity component was produced for each vertical elevation of the ADV measurements. All the negative surge data were synchronised based on the characteristic time t_3 which is further illustrated in Appendix B. The instantaneous depth data was plotted for every run of the 25 runs and the first derivative was calculated. The data was then filtered using a 0-1 Hz band pass. The error in the data synchronisation process was estimated at up to 1%.

Figures 4-11(a) presents some typical results of the ensemble averaged median water depth d_{Median}, the differences between the 3rd and 4th quartiles (d_{75}- d_{25}) and 90% and 10% percentiles (d_{90}-d_{10}) and the maximum height between the minimum and maximum water depth (d_{max}-d_{min}) at x=6 m and z=6.69 mm for the negative surge.

Figures 4-11(b) presents the ensemble averaged median water depth d_{Median}, the differences between the 3rd and 4th quartiles (d_{75}- d_{25}) and 90% and 10% percentiles (d_{90}-d_{10}) and the maximum height between the minimum and maximum water depth (d_{max}-d_{min}) at x=10.5 m z=6.69 mm for the negative surge. The full data sets of the ensemble average water depth for all vertical ADV locations at x=6 m and x=10.5 m are reported in Appendix B.

Some typical experimental results are shown in Figure 4-12 and Figure 4-13 in terms of the ensemble-averaged velocity components as a function of dimensionless time.

Each graph includes the ensemble-averaged median velocity component (V_x, V_y, or V_z), the maximum velocity between the minimum and the maximum (V_{max}- V_{min}), the differences between the 3rd and 4th quartiles (V_{75}-V_{25}), the 90% and 10% percentiles(V_{90}-V_{10}), and the ensemble-averaged median water depth d_{Median}. The full data set is presented in Appendix B.

The ensemble-averaged median water depth showed a steeper curvature for the data recorded at the gate at x=10.5 m compared to the data further upstream at x=6 m. The finding was consistent with the results of the instantaneous data presented in section 4.1. The inflection point of the median water depth and the inflection point for the longitudinal velocity V_x occurred approximately at the same time during the passage of the surge. The fluctuations of the longitudinal velocity V_x seemed to slightly increase near the inflection point of the negative surge, especially near the gate at x=10.5 m. It was also observed further upstream, but the fluctuations were smaller. The V_y velocities were very scattered at x=6 m and z=6.69 mm. However, the median velocities showed little fluctuations. The V_z velocities showed a slight increase in minimum and maximum velocity fluctuations at the beginning of the surge. Overall, the median V_z velocities did not show large variations. The median dimensionless velocities for V_z and V_y were of similar magnitude. To date there is no previous data available to compare the results.

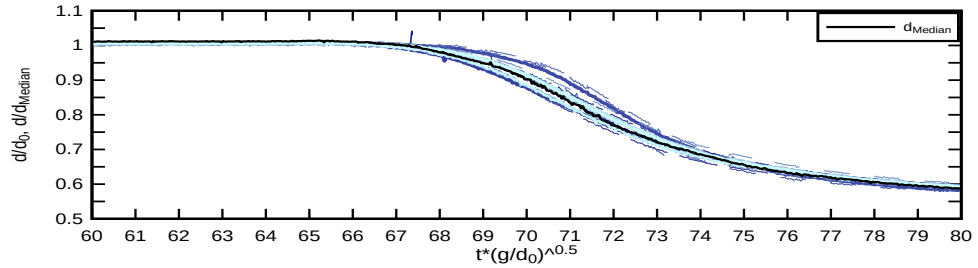

(a) time variation of median water depth d_{Median} at x=10.5 m

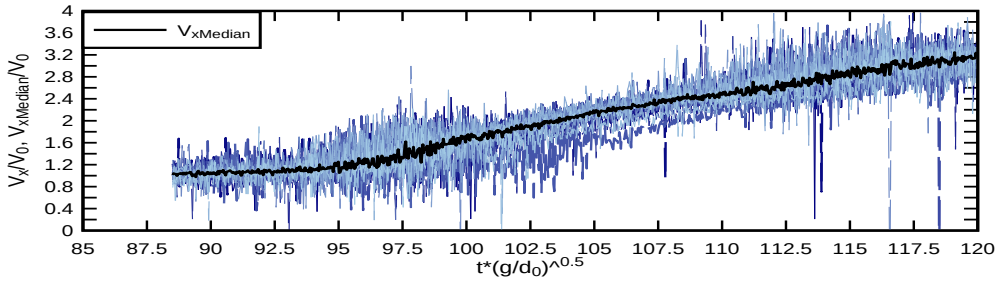

(c) time variation of median velocity in the longitudinal direction $V_{xMedian}$ at x=6 m

Figure 4-10: Instantaneous and median data for all 25 runs for the negative surge at z=6.69 mm (cont'd)

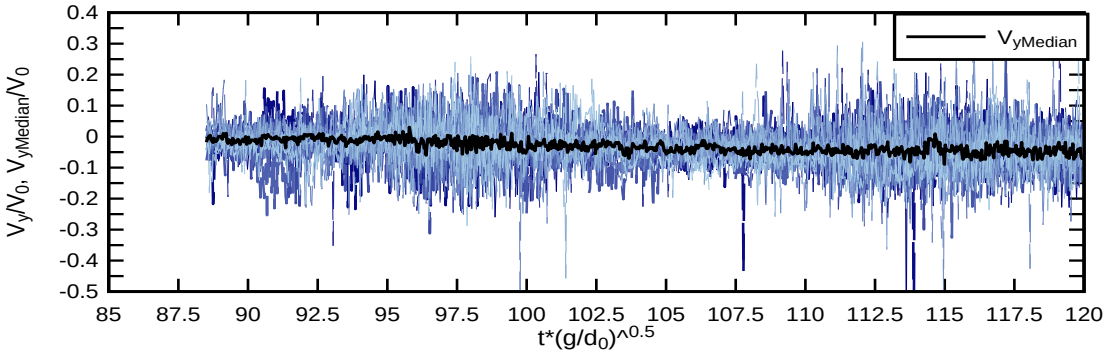

(c) time variation of median velocity in the cross-sectional direction $V_{yMedian}$ at x=6 m

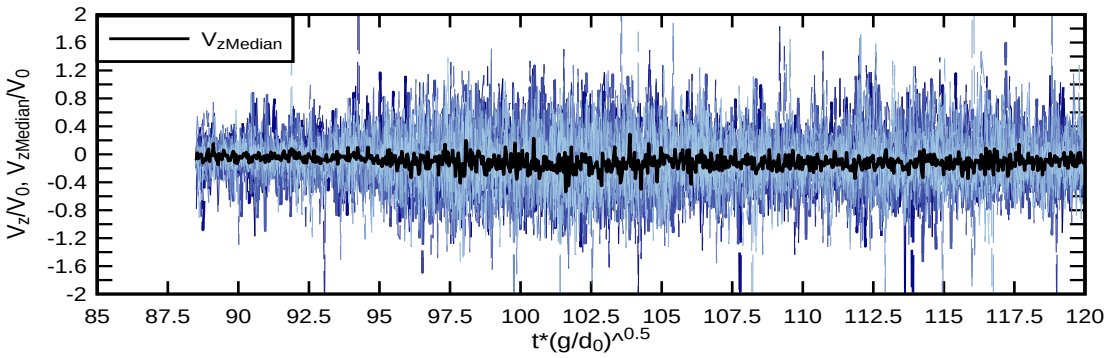

(d) time variation of median velocity in the vertical direction $V_{zMedian}$ at x=6 m

Figure 4-10: Instantaneous and median data for all 25 runs for the negative surge at z=6.69 mm

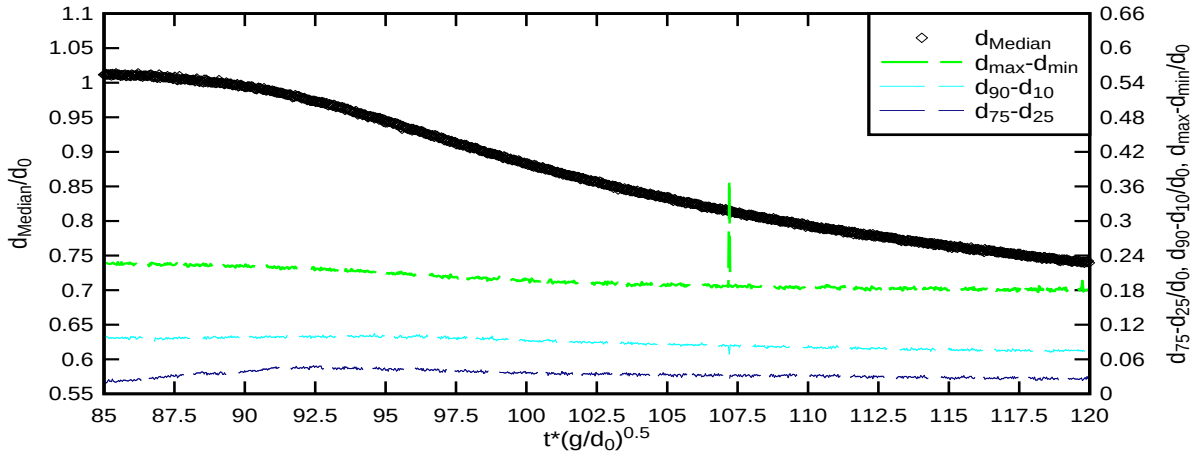

(a) x=6 m and z=6.69 mm

Figure 4-11: Dimensionless ensemble-average median water depth d_{Median}, difference between 3rd and 4th quartiles (d_{75}-d_{25}) and 90% and 10% percentiles (d_{90}-d_{10}), and range of maximum to minimum water depth (d_{max}-d_{min}) (cont'd)

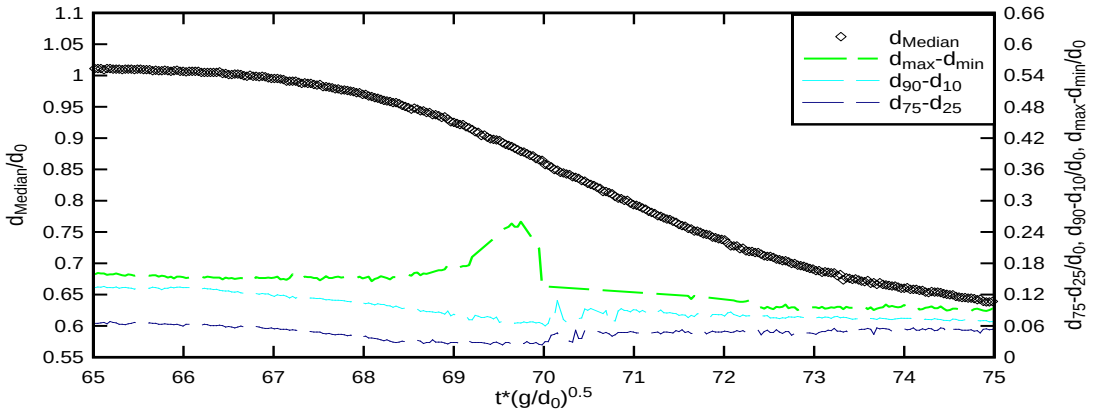

(b) x=10.5 m and z=6.69 mm

Figure 4-11: Dimensionless ensemble-average median water depth d_{Median}, difference between 3rd and 4th quartiles (d_{75}-d_{25}) and 90% and 10% percentiles (d_{90}-d_{10}), and range of maximum to minimum water depth (d_{max}-d_{min})

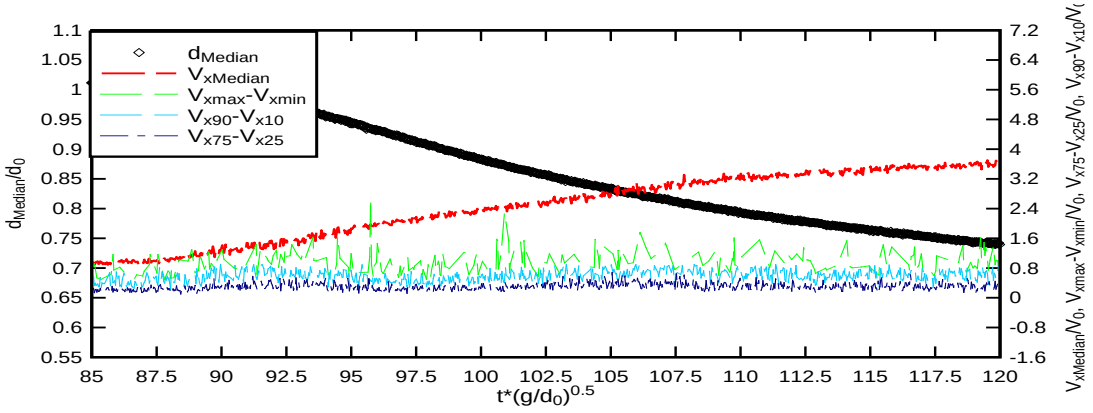

(a) V_x

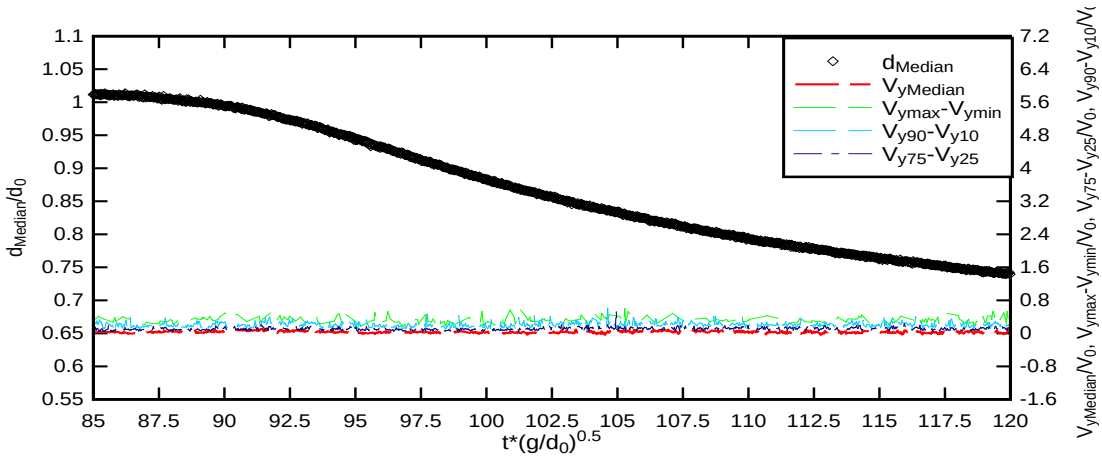

(b) V_y

Figure 4-12: Dimensionless ensemble-average median velocity V_{Median}, difference between 3rd and 4th quartiles (V_{75}- V_{25}) and 90% and 10% percentiles (V_{90}- V_{10}), and range of maximum to minimum water depth (V_{max}- V_{min}) at x=6 m and z=6.69 mm (cont'd)

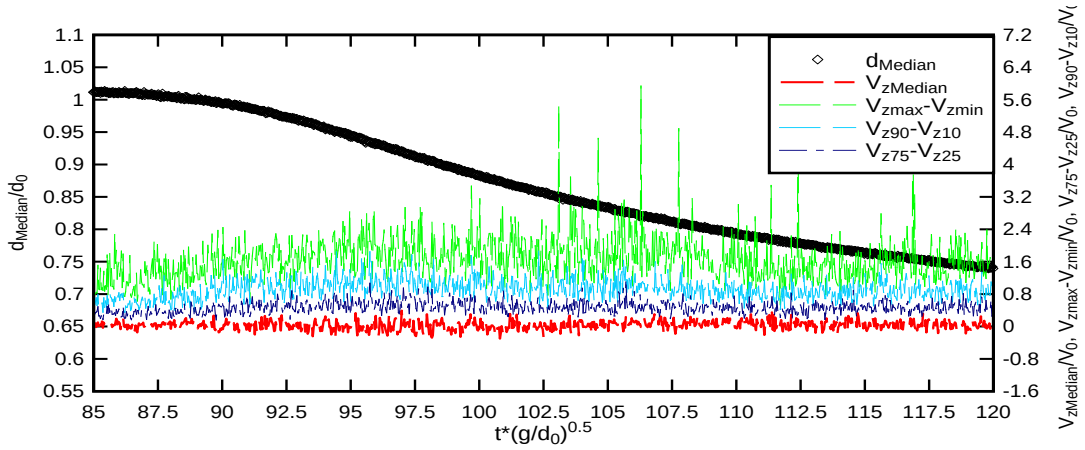

(c) V_z

Figure 4-12: Dimensionless ensemble-average median velocity V_{Median}, difference between 3rd and 4th quartiles (V_{75}- V_{25}) and 90% and 10% percentiles (V_{90}- V_{10}), and range of maximum to minimum water depth (V_{max}- V_{min}) at x=6 m and z=6.69 mm.

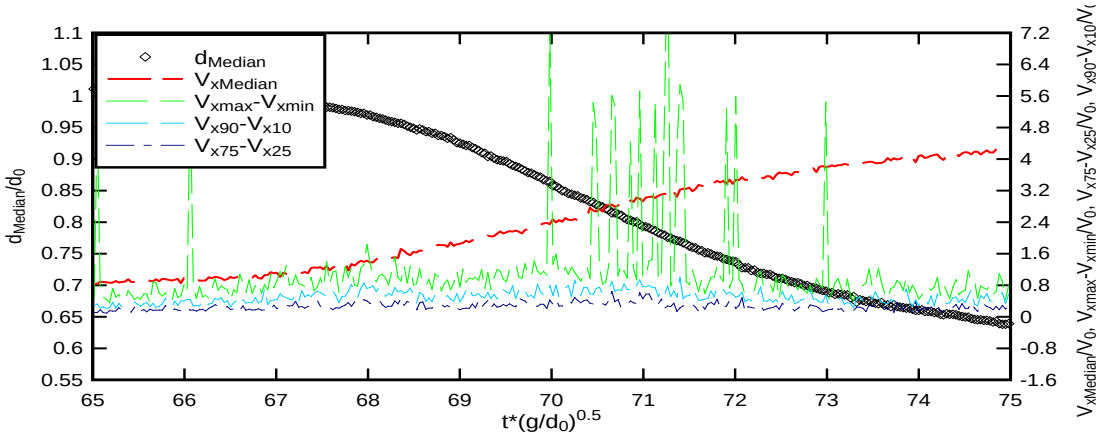

(a) V_x

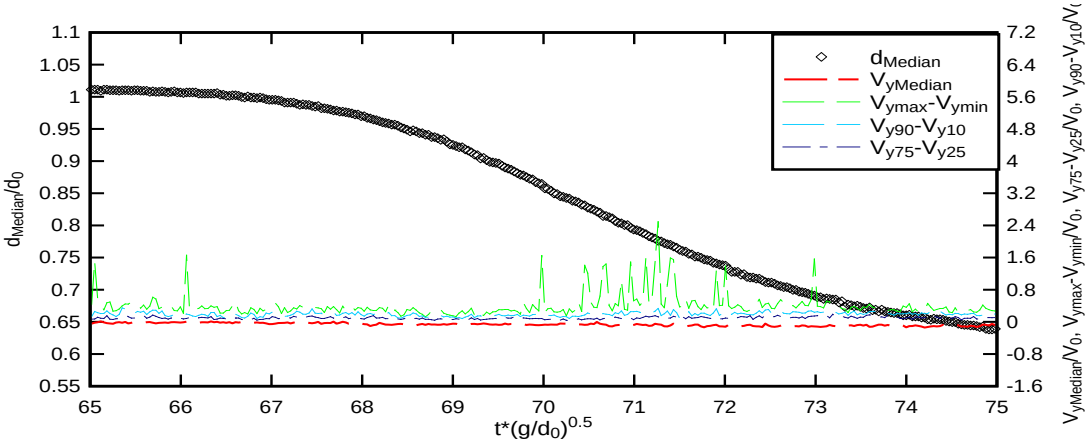

(b) V_y

Figure 4-13: Dimensionless ensemble-average median velocity V_{Median}, difference between 3rd and 4th quartiles (V_{75}- V_{25}) and 90% and 10% percentiles ($V_{z}90$- $V_{z}10$), and range of maximum to minimum water depth (V_{max}- V_{min}) at x=10.5 m and z=6.69 mm.

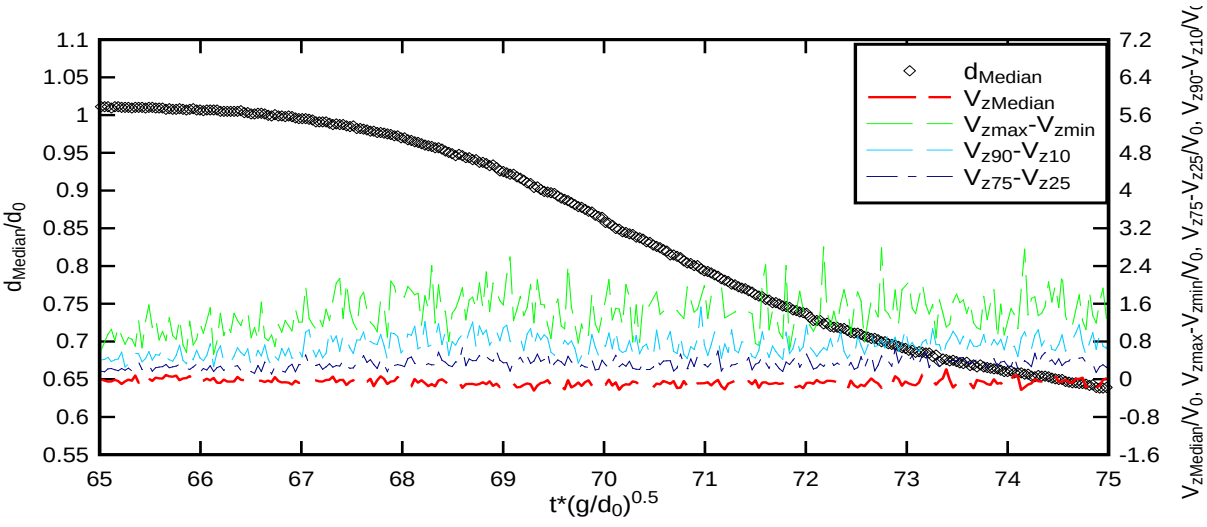

(c) V_z

Figure 4-13: Dimensionless ensemble-average median velocity V_{Median}, difference between 3rd and 4th quartiles (V_{75}- V_{25}) and 90% and 10% percentiles (V_{z90}- V_{z10}), and range of maximum to minimum water depth (V_{max}- V_{min}) at x=10.5 m and z=6.69 mm.

4.3.2 Positive surge

Figure 4-14 shows the dimensionless data of the synchronised instantaneous water depth, velocities, as well as the median water depth and median velocities for the positive surge. An ensemble-median of each instantaneous velocity component was produced for each vertical elevation of the ADV measurements. All the positive surge data were synchronised based on the characteristic time t_3, which is further illustrated in Appendix C. The characteristic points of the positive surge were identified in previous studies by Docherty and Chanson (2010). The estimated error in the data synchronisation process was estimated at up to 2%.

Figures 4-15 presents the ensemble averaged median water depth d_{Median}, the differences between the 3rd and 4th quartiles (d_{75}- d_{25}) and 90% and 10% percentiles (d_{90}-d_{10}) and the maximum height between the minimum and maximum water depth (d_{max}-d_{min}) for the positive surge. The full data set of the ensemble-averaged velocities for all vertical ADV locations and the two longitudinal locations x=10.5 m and x=6 m are presented in Appendix C.

Some typical experimental results are shown in Figure 4-16 and Figure 4-17 in terms of the ensemble-averaged velocity components as a function of dimensionless time.

Each graph includes the ensemble-averaged median velocity component (V_x, V_y, or V_z), the maximum velocity between the minimum and the maximum (V_{max}- V_{min}), the differences between the 3rd and 4th quartiles (V_{75}-V_{25}), the 90% and 10% percentiles(V_{90}-V_{10}), and the ensemble-averaged median water depth d_{Median}. The full data set is presented in Appendix C.

The maximum fluctuation of the water depth occurred at the same time as the maximum fluctuations of the vertical velocities V_x. The maximum fluctuation of the longitudinal velocity V_x occurred in the surge front passage, as seen by the large values of the differences between the 90th and the 10th percentile.

The average vertical velocity component was positive during the surge front passage. There was little fluctuation of the V_y velocities during the surge propagation. Since the surge was produced using a relatively small discharge the fluctuations of the velocities are less profound then observed in previous studies, such as Docherty and Chanson (2010) and Koch and Chanson (2009). However, the results confirmed the findings of characteristic trends in positive surges of previous studies by Koch and Chanson (2009) and Docherty and Chanson (2010).

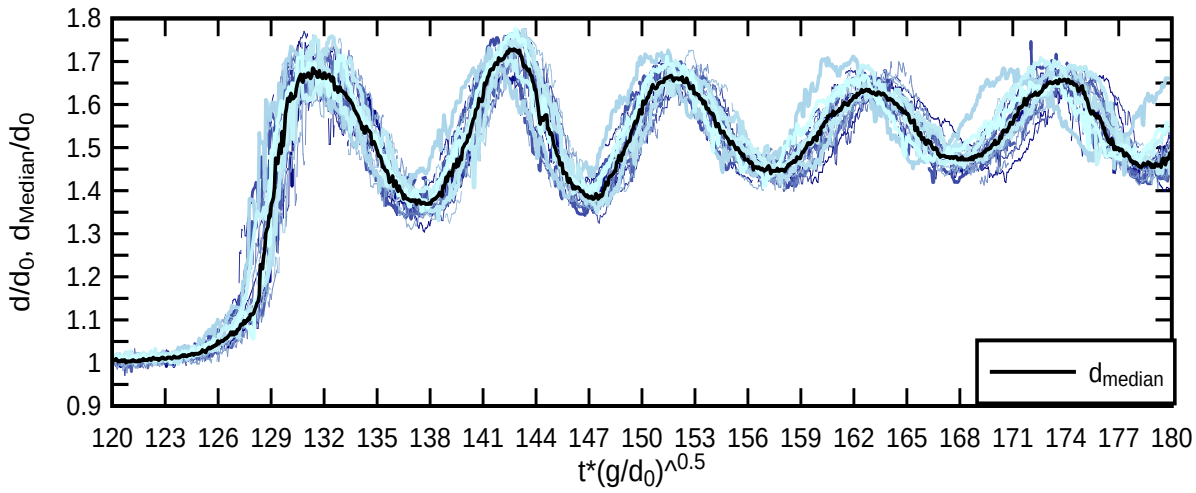

(a) time variation of median water depth d_{Median}

Figure 4-14: Instantaneous and median data for the positive surge at x=6m and z=6.69 mm (cont'd)

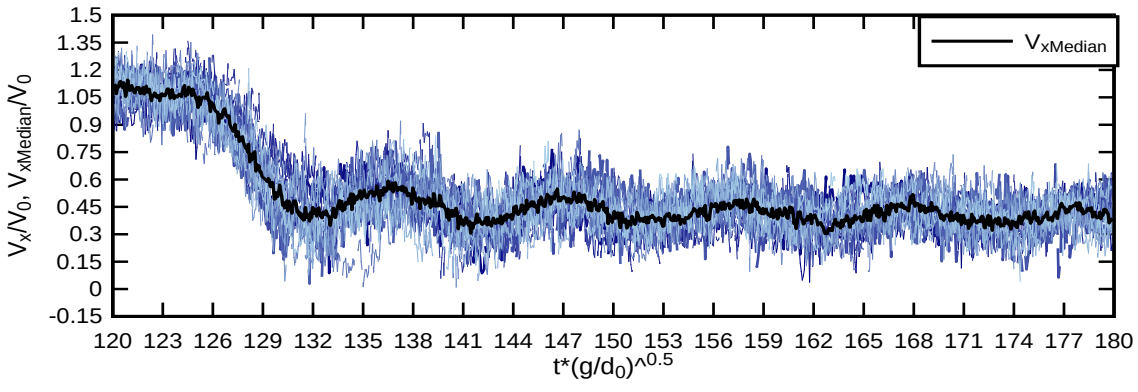

(b) time variation of median velocity in the longitudinal direction $V_{xMedian}$

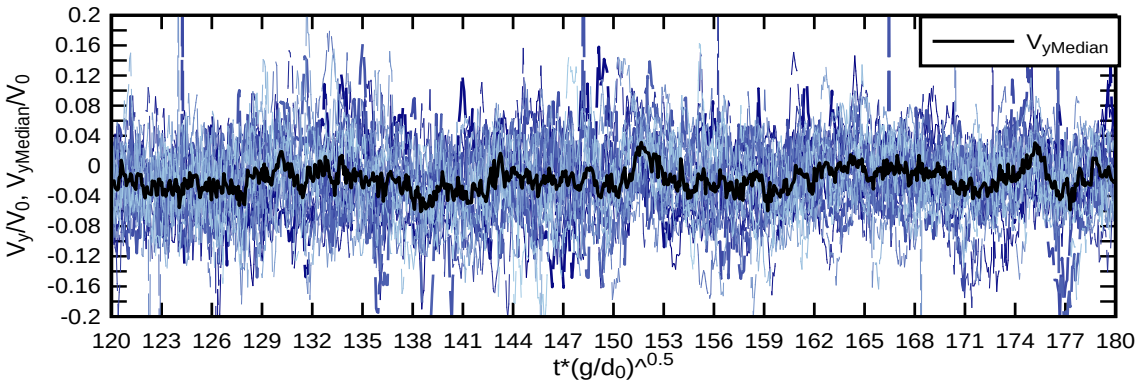

(c) time variation of median velocity in the cross-sectional direction $V_{yMedian}$

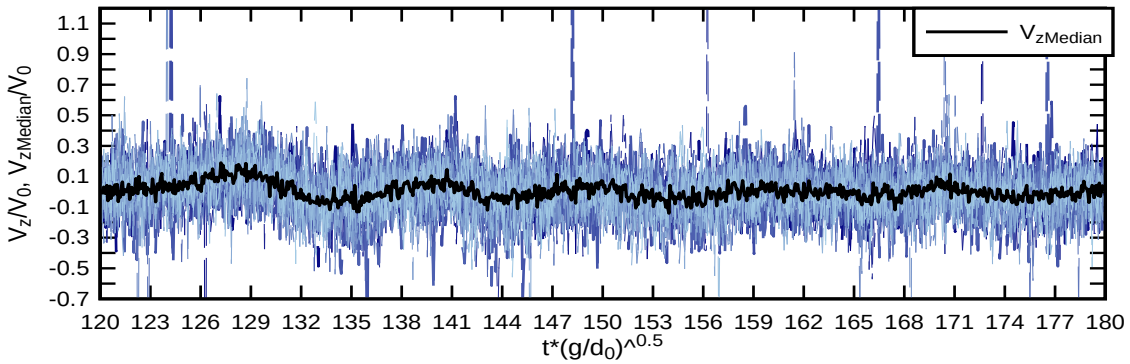

(d) time variation of median velocity in the vertical direction $V_{zMedian}$.

Figure 4-14: Instantaneous and median data for the positive surge at x=6m and z=6.69 mm

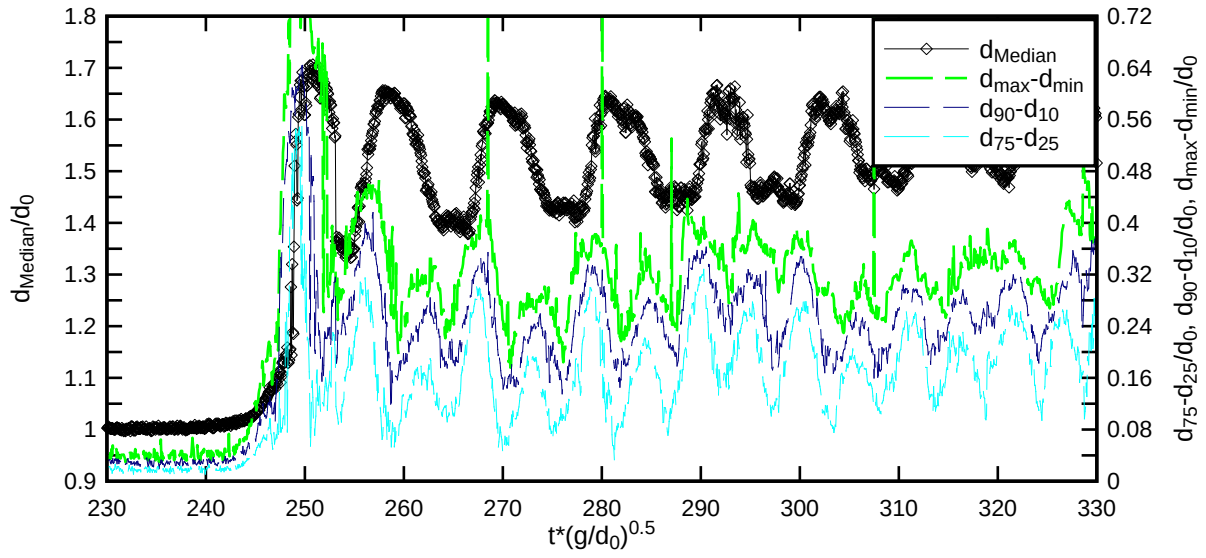

(a) x=6 m and z=6.69 mm

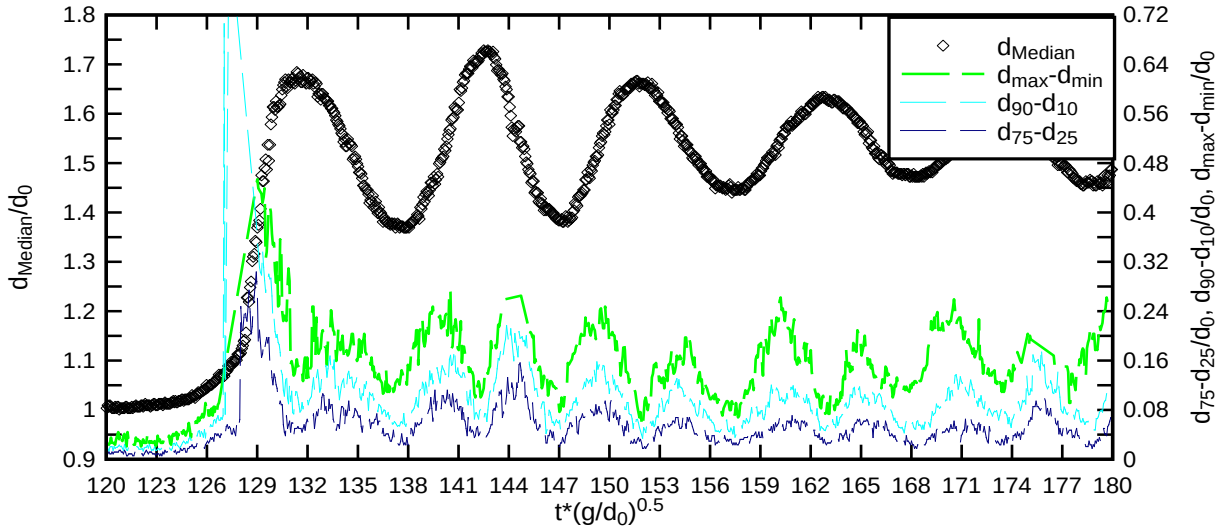

(a) x=10.5 m and z=6.69 mm

Figure 4-15: Dimensionless ensemble-average median water depth d_{Median}, difference between 3rd and 4th quartiles (d_{75}-d_{25}) and 90% and 10% percentiles (d_{90}-d_{10}), and range of maximum to minimum water depth (d_{max}-d_{min})

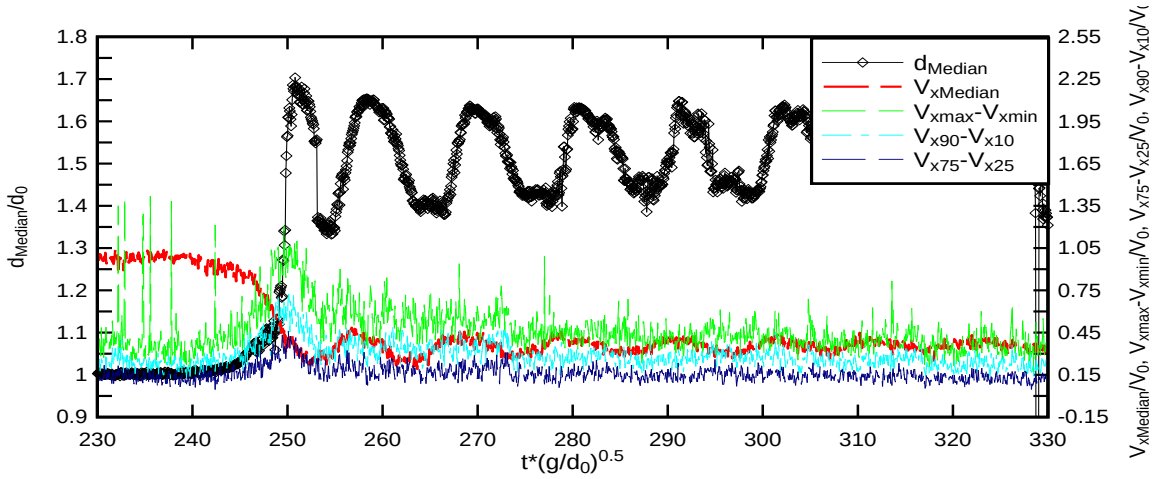

(a) V_x

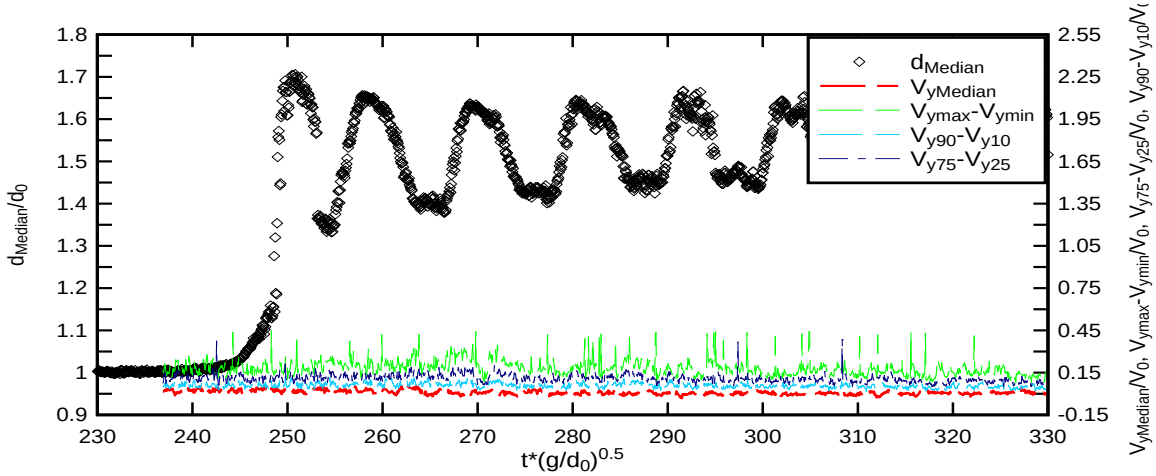

(b) V_y

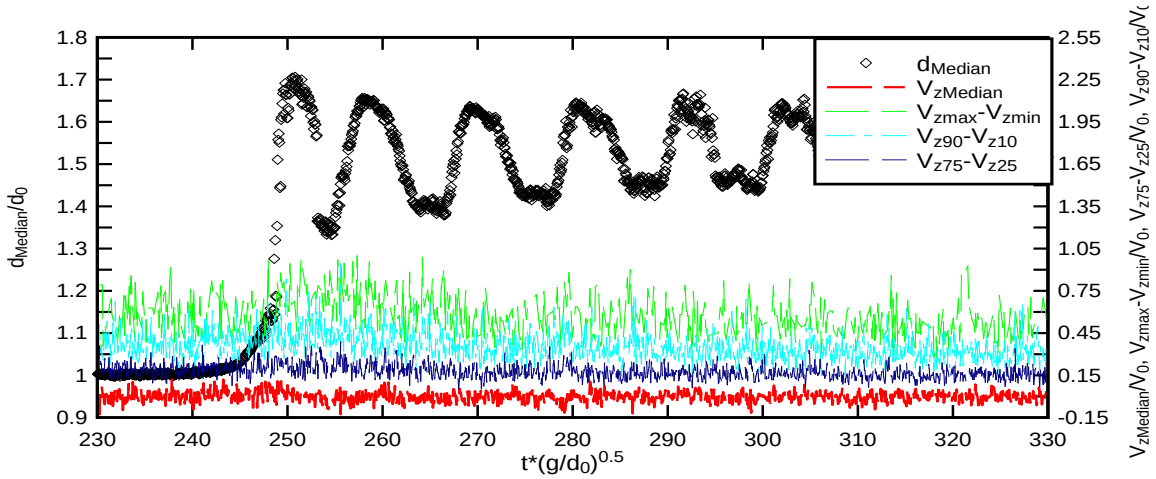

(c) V_z

Figure 4-16: Dimensionless ensemble-average median velocity V_{Median}, difference between 3rd and 4th quartiles (V_{75}- V_{25}) and 90% and 10% percentiles (V_{90}- V_{10}), and range of maximum to minimum water depth (V_{max}- V_{min}) at x=6 m and z=6.69 mm.

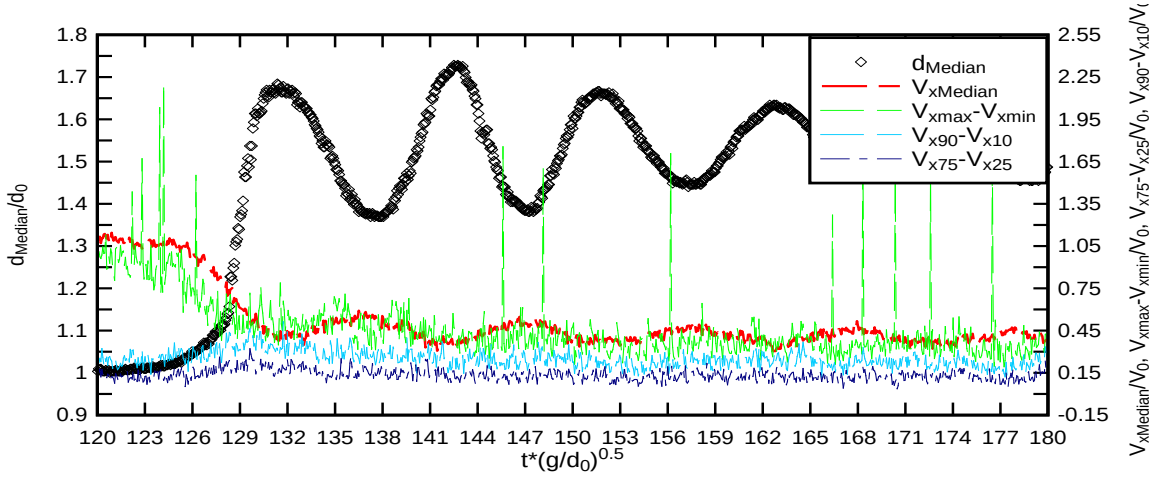

(a) V_x

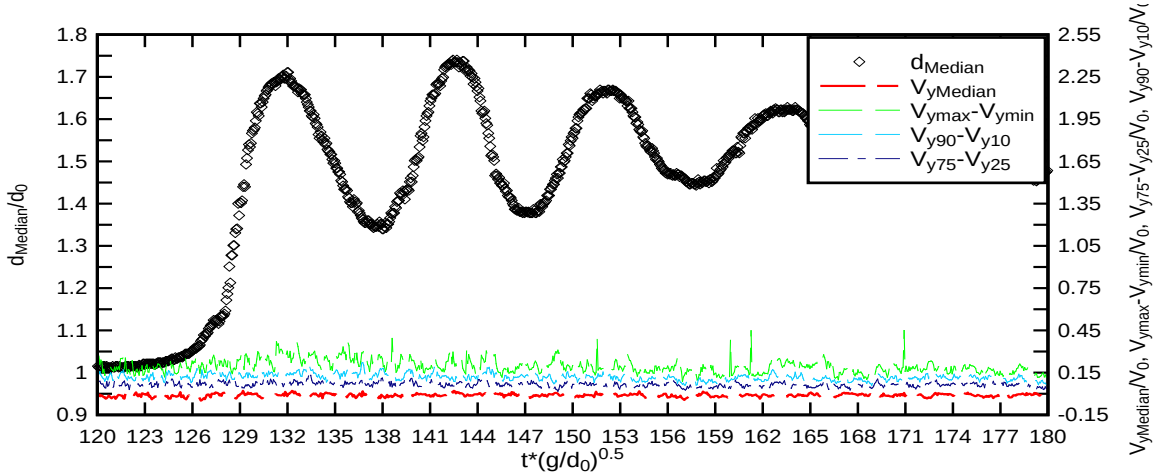

(b) V_y

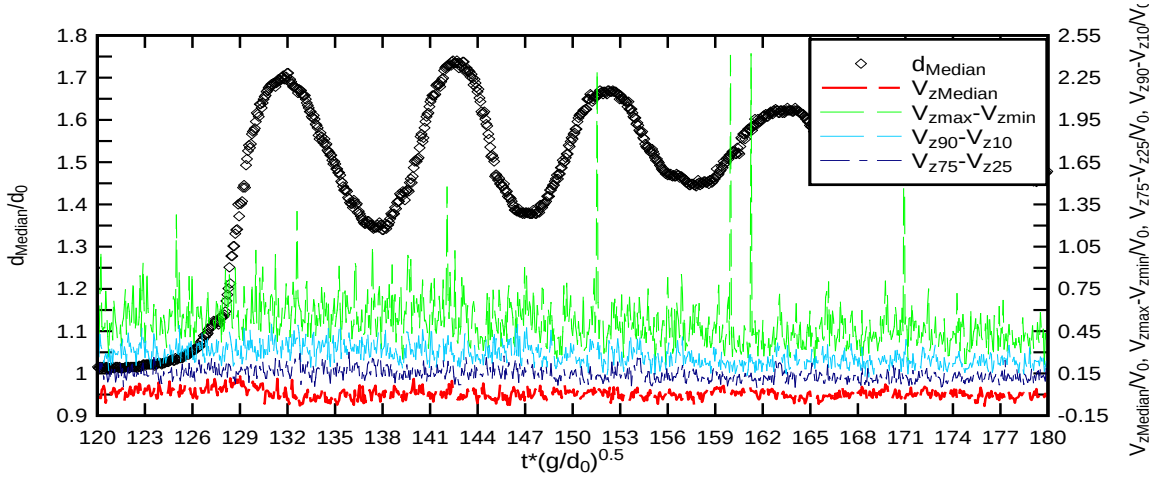

(c) V_z

Figure 4-17: Dimensionless ensemble-average median velocity V_{Median}, difference between 3rd and 4th quartiles (V_{75}- V_{25}) and 90% and 10% percentiles (V_{z90}- V_{z10}), and range of maximum to minimum water depth (V_{max}- V_{min}) at x=10.5 m and z=6.69 mm.

4.4 Discussion

The celerity of the negative surge was measured from the video and acoustic displacement meter data. Figure 4-18 illustrates the results in dimensionless terms with a dotted line showing the location of the gate. Figure 4-18(a) shows the data for one set of flow conditions. Figure 4-18(b) shows the dimensionless celerity data with x/L, where L refers to the channel length of 12 m. This dimensionless presentation enabled the comparison of different flow conditions. The flow conditions are summarised in Table 4-3. The full data sets are presented in Appendix E.

The experimental results showed two distinct phases. Very close to the gate, and immediately after gate closure, the negative surge formation was associated with some local dissipative process illustrated in Appendix A. During this formation phase, the celerity of the negative surge leading edge increased with time. Within the experimental flow conditions (Table 4-3), the present data sets suggested that the acceleration phase took place within 1 m from the gate. After the acceleration/formation phase, the negative surge propagated upstream in a more gradual manner. During this gradually-varied phase, the surge leading edge was very flat and barely perceptible by human eye, and its celerity tended to decrease slowly with increasing distance from the gate as shown in Figure 4-18(a) for $x/d_o < 40$. The data tended to imply some effect of flow resistance in manner possibly opposite to that predicted by Henderson (1966, pp. 297-299). At x=6 m, the dimensionless negative surge celerity $(U+V_o)/\sqrt{g \times d_o}$ ranged from 0.3 up to 1.0 depending upon the initial steady flow conditions (Table 4-3, 5th column).

For comparison, the analytical solution of the Saint-Venant equations for a simple wave predicts that the leading edge of the negative surge propagates with a constant dimensionless celerity $(U+V_o)/\sqrt{g \times d_o}=1$. Lauber and Hager (1998) performed experiments in a horizontal rectangular channel initially at rest (V_o=0) with a 3.5 m long reservoir. They observed $U/\sqrt{g \times d_o} =\sqrt{2} =1.41$. Tan and Chu (2009) re-analysed the data of Lauber and Hager, and their computational data matched the experimental observations yielding $U/\sqrt{g \times d_o}=1$. The present results (Figure 4-18, Table 4-3 & Appendix E) suggest that neither the Saint-Venant equations solution nor previous findings are applicable herein. While the negative surge formation might be affected by the gate opening mechanism, the gradually-varied phase associated with a slow deceleration of the negative surge leading edge was likely linked with the initial flow conditions and flow resistance. The present findings suggested that further studies are required to assess the effect of initial flow conditions and flow resistance on the propagation of negative surges.

Table 4-3: Flow conditions and celerity measurement

Q (l/s)	Gate opening h (mm)	V_0 at x=6m m/s	d_0 at x=6 m m	$(U+V_o)/sqrt(g \times d_o)$ at x=6	Remark
20	30	0.167	0.23	1.0	0.7-1.17 for 5.6 < x < 8.55 m
20	50	0.4	0.1	0.66	
30	40	0.231	0.26	0.30	
30	50	0.273	0.22	0.52	

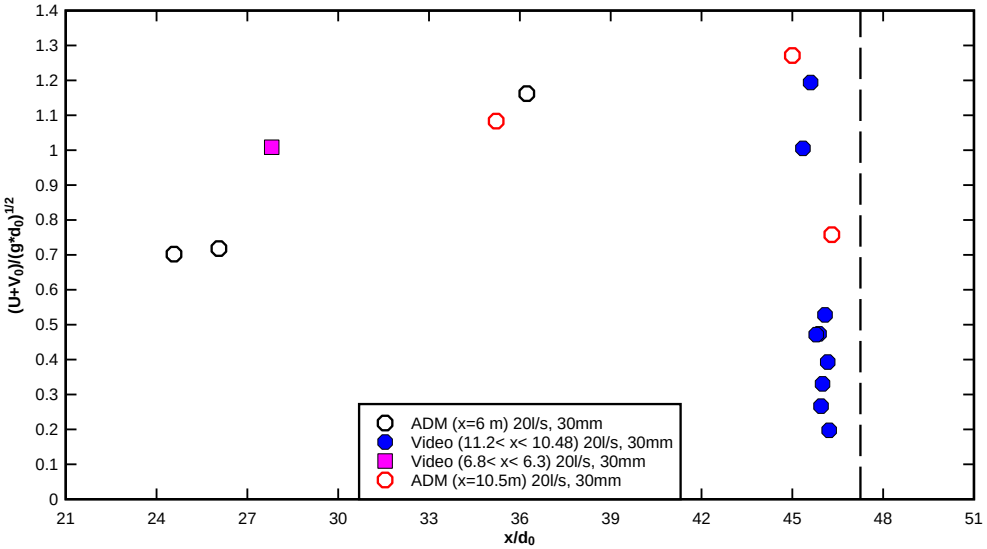

(a) Dimensionless celerity $(U+V_o)/(g\ d_o)^{1/2}$ as function of longitudinal distance x/d_o for Q=0.020 m^3/s and h=30 mm

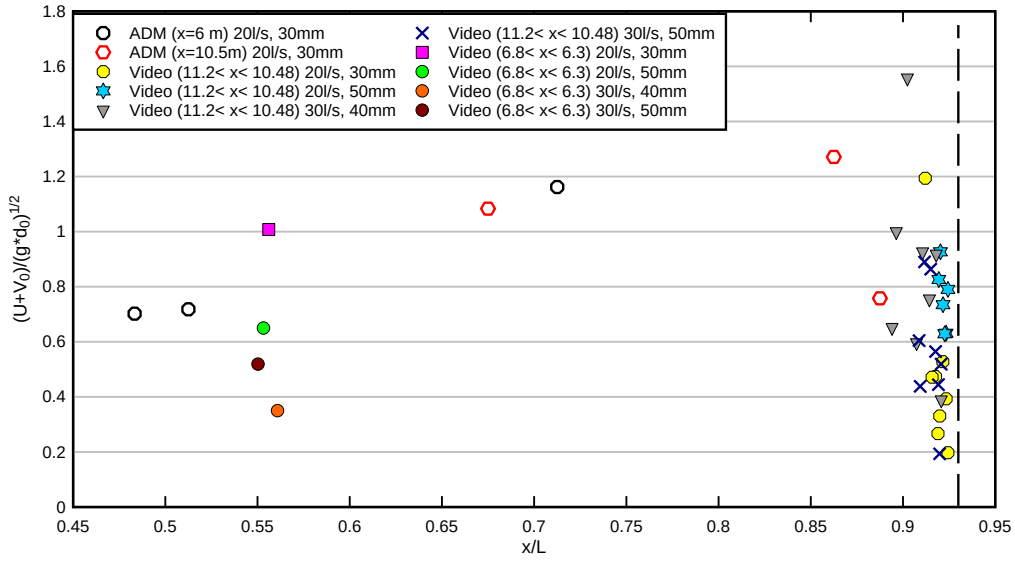

(b) Dimensionless celerity $(U+V_o)/(g\ d_o)^{1/2}$ as function of longitudinal distance x/L (L=12 m)

Figure 4-18: Celerity of negative surges

5 Numerical modelling

5.1 One dimensional modelling: numerical solution of the Saint-Venant equations

5.1.1 Negative surge

Different to steady-state modelling, the unsteady open flow modelling uses the unsteady solution of the continuity and momentum equations. The vertically integrated equations of the continuity and momentum equations are often referred to as the Saint-Venant equations.

The numerical integration of the Saint-Venant equations was performed using the Hartree method. The Hartree method consists of a fixed grid with fixed time and time and special intervals (Montes 1998, Chanson 2004). It is also referred to as the method of specified time intervals. The flow properties are known at time t = (n-1)δt. At the following time-step t +δt, the characteristic intersection at point M (x=i δt, t= n δt) are projected backwards in time where they intersect the line t= (n-1)δt at point L and R whose location are unknown (Figure 5-1). The characteristic system reads as follows:

$V_L + 2C_L = V_M + 2C_M + g(S_f - S_0)\delta t$ forward characteristic (5-1)

$V_R + 2C_R = V_M - 2C_M + g(S_f - S_0)\delta t$ backward characteristic (5-2)

$(x_m - x_L)/\delta t = V_L + C_L$ forward characteristic (5-3)

$(x_m - x_R)/\delta t = V_R - C_R$ backward characteristic (5-4)

assuming $(S_f - S_0)$ constant during the time step δt. The subscripts M, L, R refer to points in the characteristic system (Chanson 2004, Liggett 1994). For the linear interpolation the time step must satisfy the Courant conditions:

$$\delta t \leq \frac{\delta x}{|V + C|} \quad \text{and} \quad . \quad \delta t \leq \frac{\delta x}{|V - C|} \tag{5-5}$$

where $|V+C|$ is the absolute value of the term (V+C) (Chanson 2004).

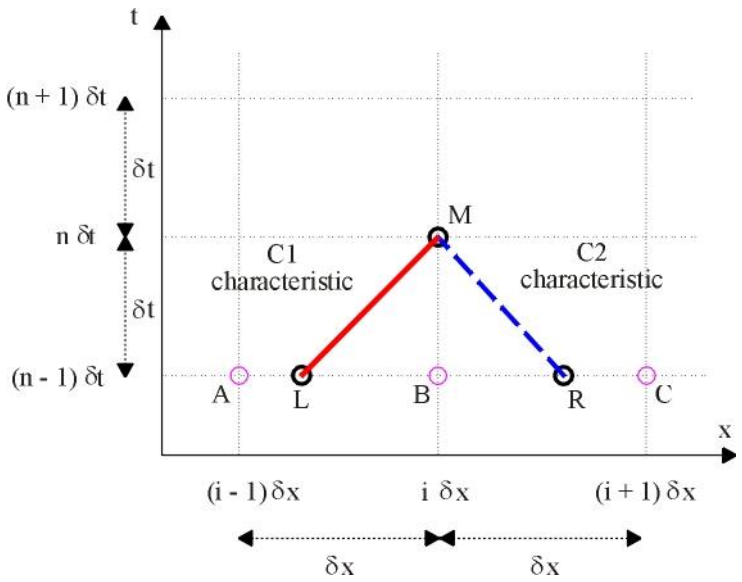

Figure 5-1: Numerical integration of the methods of characteristics by the Hartree methods (Chanson 2004)

Both the analytical solution using the simple wave method and numerical model data were compared with the physical data (Figure 5-2). The analytical solution based upon the simple wave theory compared well with the physical data. The numerical solution of the Saint-Venant equations using the Darcy friction factors f=0.015, f=0.025 and f=0.035 also gave some good results. Most computer software packages use the numerical solution of the Saint-Venant equations for solving one-dimensional flows. Figure 5-2 shows the best agreement with the recorded ADM data was reached by the simple wave solution. Therefore, one may argue that the analytical solution of the Saint-Venant equations did match the physical results better than the numerical solutions or friction effects are negligible.

Note however, that the present flume had a rectangular cross-section and was lined with PVC and glass. Therefore, there was a small boundary friction. In natural channels, the surface roughness is likely to be greater than in a laboratory setting and it might be necessary to include different friction factors.

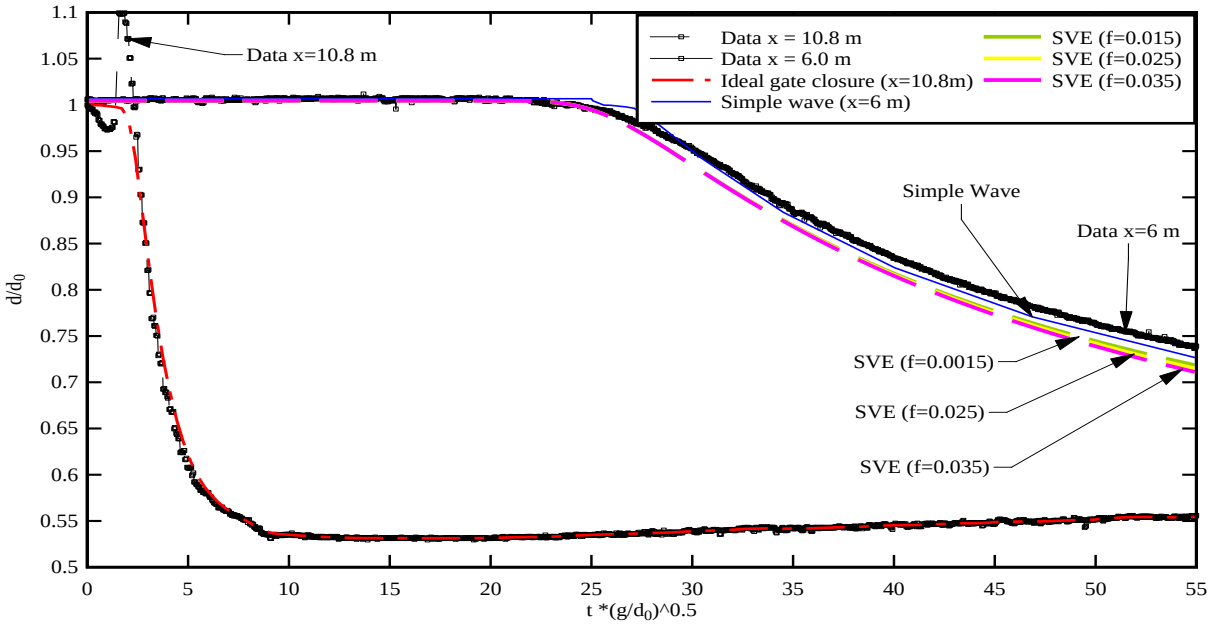

Figure 5-2: Dimensionless unsteady free-surface profile during the negative surge with 20 l/s discharge and a 30 mm gate opening

5.1.2 Positive surge

The simple wave method was compared with the recorded acoustic displacement meter data for the positive surge at x=6 m. Figure 5-3 illustrates that the analytical solution based upon the simple wave theory did not compare well with the physical data. The simple wave solution overestimates the celerity of the surge and underestimates the height of the surge front. The simple wave method only allows calculating the timing of the surge front and the water level increase. There was a difference of 7.8 s between the arrivals of the surge front of the simple wave method compared to the physical data.

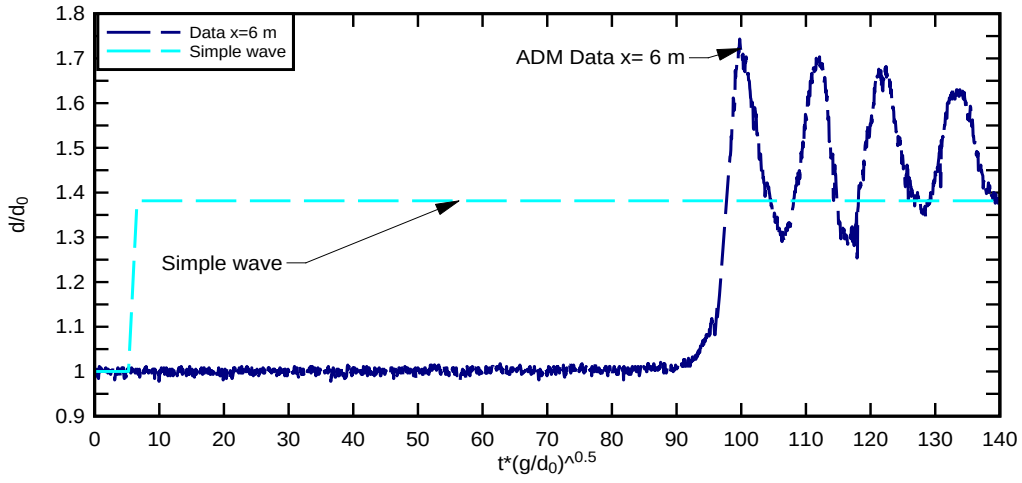

Figure 5-3: Dimensionless unsteady free-surface profile during the positive surge with 20 l/s discharge and a 30 mm gate opening

5.2 Two dimensional modelling with Flow-3D

Flow-3D^{TM} is a CFD model developed by Flow Science Inc.. Flow-3D^{TM} calculates the three velocity components (V_x, V_y, V_z) and pressures at the nodes of an orthogonal finite difference grid, using a range of turbulence models. Flow-3D^{TM} has the capabilities of modelling free surface flows using the Volume of Fluid (VOF) method.

The models were set up using Flow-3D^{TM} version 9.3. The viscosity and velocity fluctuations option was selected with Newtonian viscosity and the renormalisation group (RNG) turbulence model that used a dynamically computed maximum velocity fluctuations mixing length.

The RNG model was selected because it was recommended as the most robust turbulence model available within the Flow-3D^{TM} modelling software (Flow-3D user manual 2007).

The geometry for the models was a simple rectangular channel with the same width and depth as the experimental channel the length of the channel was extended by 0.8 m to reduce boundary effects. The gate was simulated using the general moving object (GMO). The GMO settings were set as prescribed motion with 6 degree of freedom (6-DOF).

The initial location of the reference point was selected in the middle of the gate at x=11.2 m, y=0.25 m and z=0.25 m. The gate was operated using the translational velocity component in the space system with a velocity of a non-sinusoidal movement in the z direction of -1 m/s for the positive surge and +1 m/s for the negative surge. The gate opening was selected to maximise model stability. The gate movement for the simulations was vertical, which is different from the gate operation in the experimental setup, where the gate opens in a semi-circular movement.

The selection of mesh size is essential for both the accuracy of the result and the simulation times. Therefore, a sensitivity analysis was performed using three different uniform mesh sizes of 5 mm, 15 mm and 30 mm. Smaller sizes have been tried out, however, due to time limitations and model stability the smallest size chosen was 5 mm. The results of the sensitivity analysis are further discussed in the following sections.

The selection of appropriate boundary conditions is essential for the accuracy of the simulations. The boundary conditions are summarised in Table 5-1. However, there are several other boundary options available in the software that could be applied for the models in this study.

The choice of the boundary options was made to replicate the steady flow state prior to the surge generation as closely to the experimental conditions as possible.

Table 5-1: Boundary conditions for Flow-3D™ models

	X_{Min}	X_{Max}	Y_{Min}	Y_{Max}	Z_{Min}	Z_{Max}
Negative surge	P	P	S	S	W	S
Positive Surge	Q	P	S	S	W	S

Notes; P is the specified pressure boundary; S is the symmetry boundary; W is the wall boundary and Q stands for the volume flow rate boundary.

5.2.1 Negative surge

A sensitivity analysis was performed to assess the impact of mesh size on the surface profile of the negative surge. The results are presented in Figure 5-4. The Flow-3D™ simulation replicated the experimental data for the negative surge reasonably well. However, all the simulation using the 5 mm, 15 mm and 30 mm mesh sizes showed that the water depth decreased more slowly than the recorded data. The uniform mesh size of 5 mm compared best with the measured results. The 15 mm and 30 mm mesh sizes produced similar outcomes and no improvement was observed by using the 15 mm mesh size compared to the 30 mm mesh size. The results recorded at x=6 m as presented in Figure 5-4 (b) showed the same trend as observed at x=10.8 m using the 5 mm uniform mesh size and compared the best to the measured data. The results calculated using the Flow-3D™ software code, using a 5 mm mesh, are further illustrated in this section. The velocity was assessed at four vertical elevations, which were closest to the measurements taken in the experimental setup using the ADV and acoustic displacement meters. The data were recorded on the centreline near the gate at x=10.5 m and further upstream at x=6 m. The figures show dimensionless flow depth d/d_o as a function of dimensionless time from gate closure $t \times \sqrt{g / d_0}$, where d_o is the initial water depth at x=6 m and x=10.5 m respectively. Figure 5-5 presents some typical results in the form of dimensionless time variation and water depth. For the negative surge, the surface water profiles at the gate showed a steeper drop in water depth close to the gate (e.g. x=10.8 m) compared to the observations further upstream at x=6 m, which is consistent with the findings in previous sections (Figures 4-1 and 4-2). The longitudinal velocity V_x data were closely linked with the depth profile. Due to the rapid drop in the depth profile only little output was available near the gate for the vertical velocity recordings as further illustrated in Appendix D.

Generally, the water depth decreased relatively gradually after the initial surge formation. The free surface measurements showed some marked curvature near the surge leading edge. The longitudinal velocity component increased at the same time as the water depth decreased.

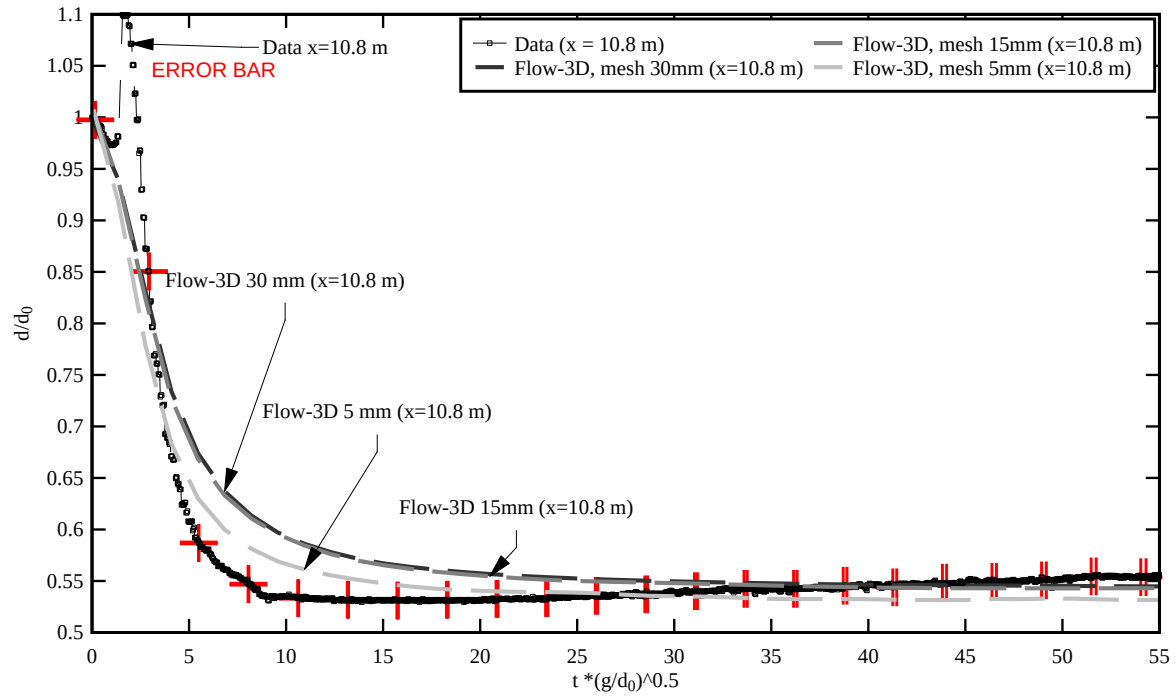

(a) x=10.8 m

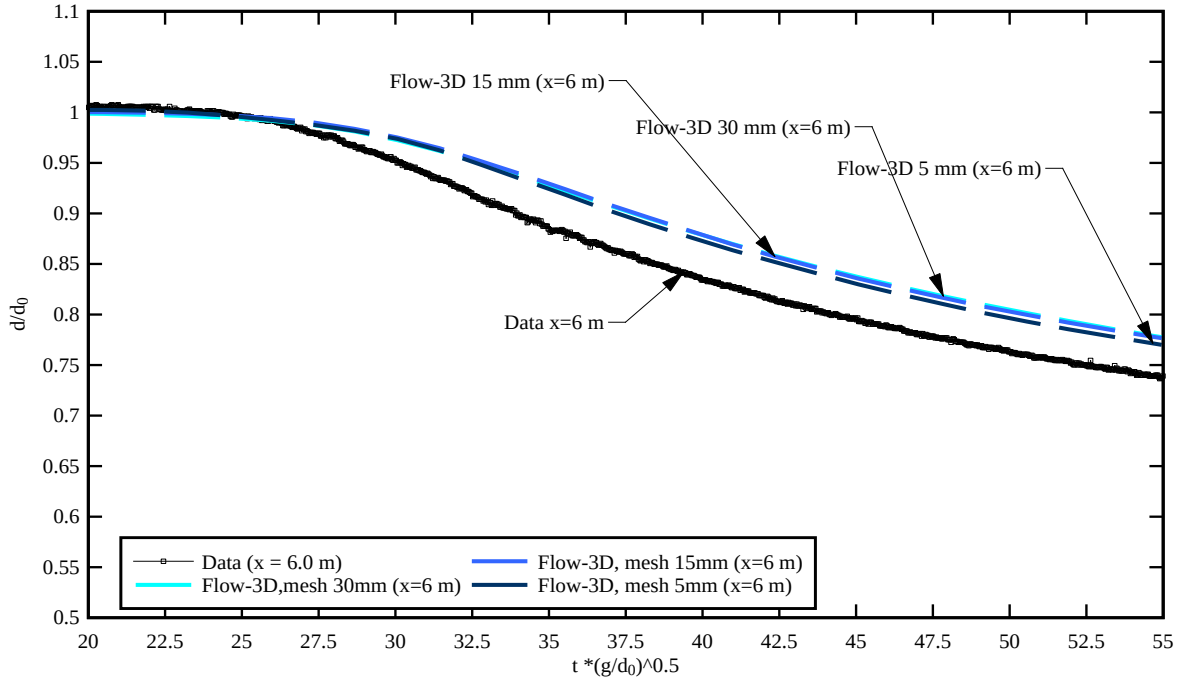

(b) x=6 m

Figure 5-4: Dimensionless unsteady free-surface profile during the negative surge recorded and simulated data

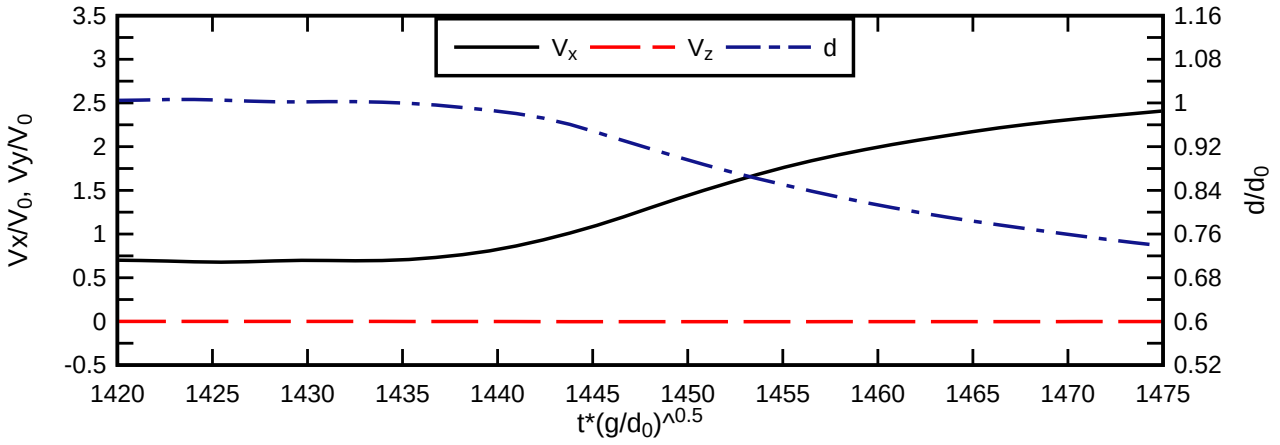

(a) x=6 m, z=7.5 mm, Q=20 l/s, d_0=0.20 m, initial gate opening 30 mm and 5 mm mesh size

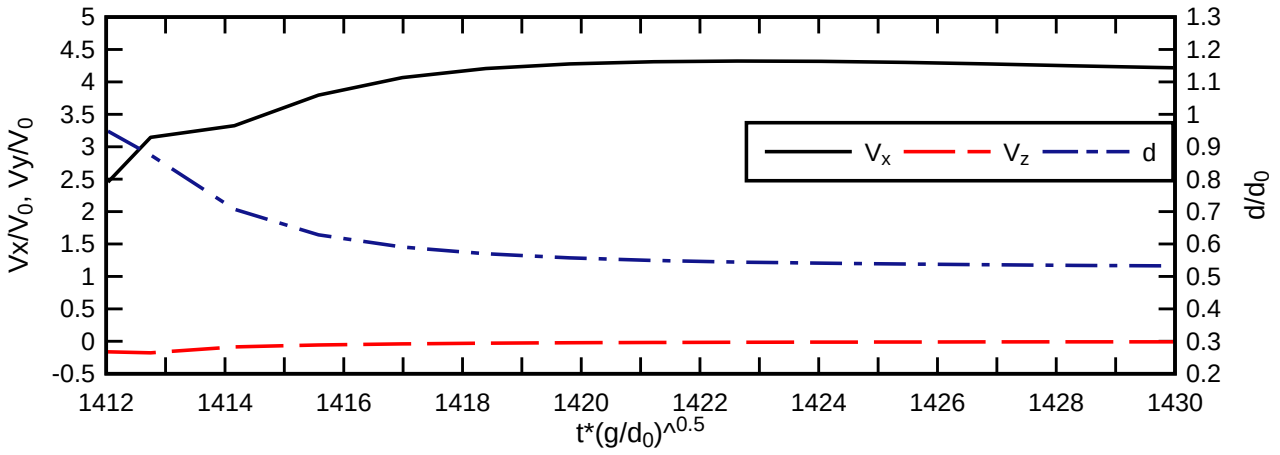

(b) x=10.5 m, z=7.5 mm, Q=20 l/s, d_0=0.064 m, initial gate opening 30 mm and 5 mm mesh size

Figure 5-5: Dimensionless velocity and depth measurements of a negative surge simulated using Flow-3D™

5.2.2 Positive surge

A sensitivity analysis was performed to assess the impact of mesh size on the surface profile of the positive surge. The results are presented in Figure 5-6. The Flow-3D™ simulations did not replicate the experimental data for the positive surge well. All the simulation using the 5 mm, 15 mm and 30 mm uniform mesh sizes showed that the water depth increased much less at the beginning and during the propagation of the surge. All three simulations underestimated the water depth during the surge propagation. The increase in mesh size was relatively sensitive to the timing of the surge front. The simulation using a 15 mm uniform mesh provided good results compared to the recorded data for the timing of the initial surge formation.

However, it not only underestimated the increase in wave amplitude but also overestimated wave length. The Flow-3D^{TM} simulation using the 5 mm mesh overestimated the velocity of the surge propagation and underestimates the water depth during the surge. However, it provides a slightly higher water depth than the simulation using a uniform 15 mm and 30 mm mesh. Overall, none of the Flow-3D^{TM} simulations provided good agreement with the physical data.

The velocity results calculated, using a 5 mm mesh, are presented in this section. The velocity was assessed at two vertical elevations, which are closest to the measurements taken in the experimental setup using the ADV and acoustic displacement meters. The data were recorded on the centreline near the gate at x=10.5 m and further upstream at x=6 m. The curves show dimensionless flow depth d/d_o as a function of dimensionless time from gate closure $t \times \sqrt{g / d_0}$, where d_o is the initial water depth at x=6 m and x=10.5 m respectively Figure 5-6 presents some typical results in the form of dimensionless time variation and water depth. The results at x=6 m and z=7.5 mm are presented in Figure 5-7. The results showed that there is a decrease in V_x in the initial phase of the positive surge and an increase in water depth. The V_z data did not show large variations between the steady state phase and the propagation of the positive surge. The results for the second location near the gate at x=10.5 m were unsatisfactory and are illustrated in Appendix D.

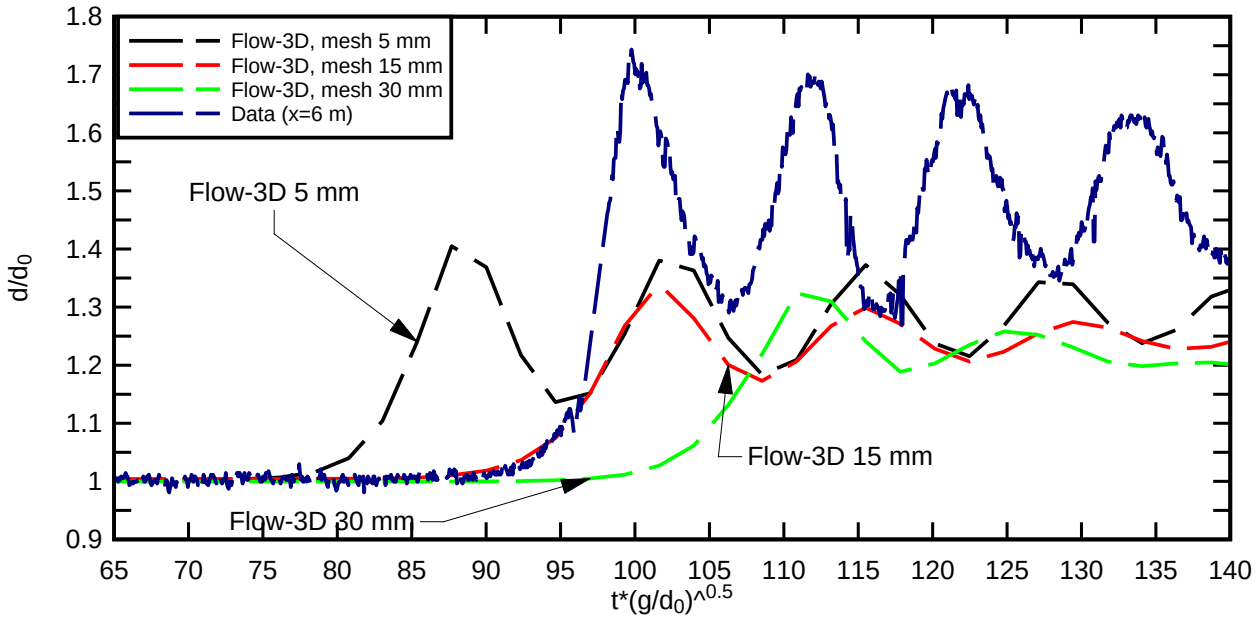

Figure 5-6: Dimensionless unsteady free-surface profile during the positive surge recorded and simulated data

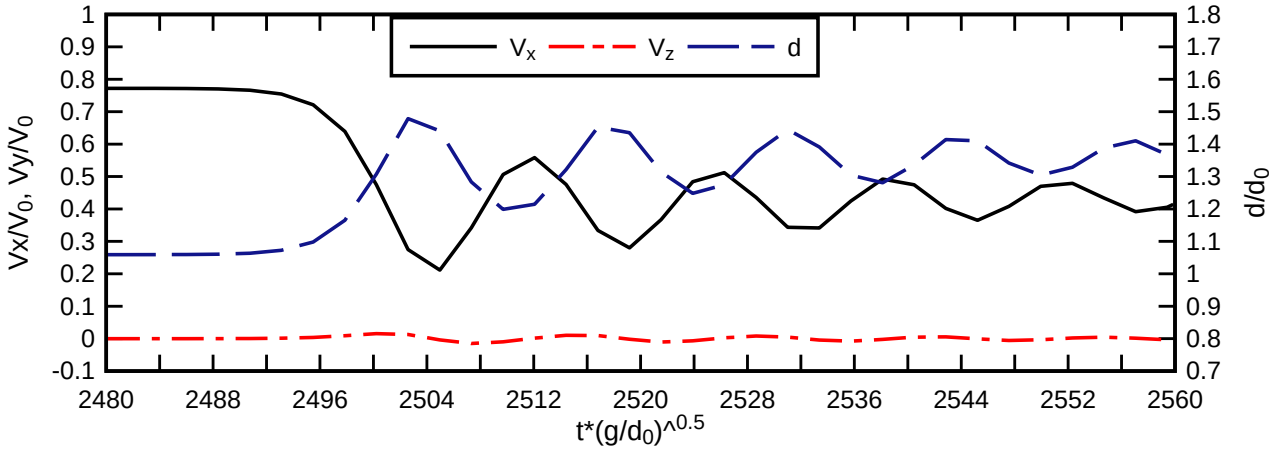

Figure 5-7: Dimensionless velocity and depth measurements of a positive surge simulated using Flow-3D at x=6 m, z=7.5 mm, Q=20 l/s, d_0=0.064 m, initial gate opening 30 mm and 5 mm mesh size

6 Comparison between numerical and physical data

6.1 Negative surge

6.1.1 Surface profile

The analytical solution and numerical model data were compared with experimental data from ADM and video measurements (Figure 6-1). The video measurements at 10.8 m compared well with the ADM data. However, near the gate the video data was slightly higher than the ADM data. This might be related to the difficulty in estimating the water surface near the gate form the video recordings. The simple wave method and the numerical integration of the Saint-Venant equations compared well with the physical data. The solutions with no or little friction compared better to the recorded data, than the ones with higher friction factors. However, the laboratory flume had a rectangular cross-section and was lined with PVC and glass. Therefore, it had a small boundary friction. In natural channels, the surface roughness is likely to be greater than in a laboratory setting and it might be necessary to include different friction factors. The Flow-3D^{TM} results produced a comparable output at x=10.8 m. It is suggested that the initial difference in the surface of the water depth is related to the gate opening mechanism. As observed in previous sections the instantaneous free surface measurements recorded a spike near the gate, which might be due to the semi-circular movement of the gate, which pushed the water upwards, before the natural progression of the surge. Initially the water depth was simulated quite well using Flow-3D^{TM} at x=10.8 m. However, it overestimated the water depth shortly after the inflection points of the free surface and slightly underestimated it, when the water depth reached the steady state flow. Overall, for the location near the gate at x=10.8 m, the 5 mm mesh size matched best against experimental data compare to the models with a uniform mesh size of 15 mm and 30 mm. The Flow-3D^{TM} simulation at x=6 m using 5 mm, 15 mm and 30 mm mesh sizes overestimated the water depth, but produced a similar slope compared to the recoded data. The propagation of the negative surge is replicated quite well for all the numerical method, with the surge front passing through x=6 m, close to the measured data. The Flow-3D^{TM} results showed a slight delay in the surge front, which might be a result of the differences in gate opening mechanisms.

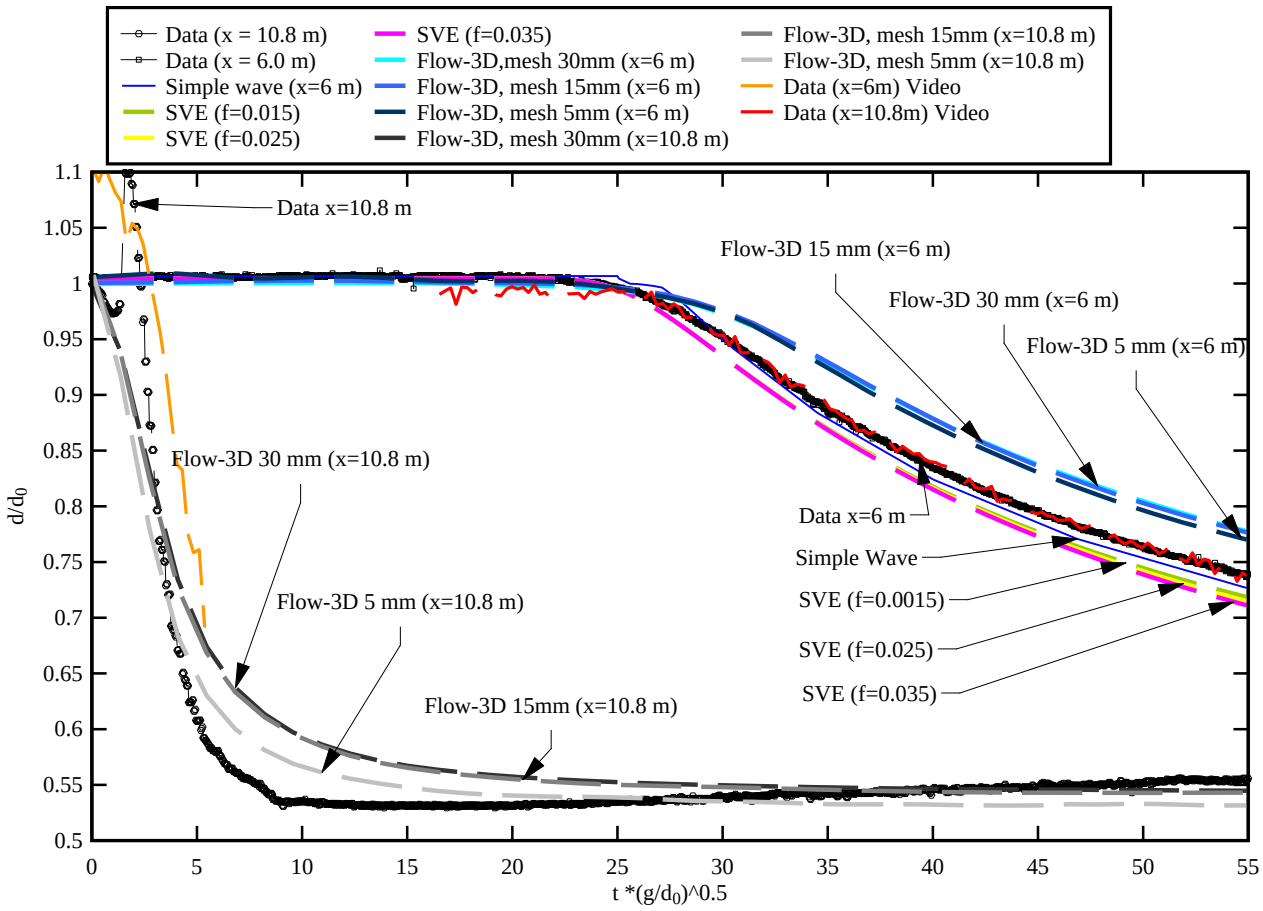

Figure 6-1: Dimensionless unsteady free-surface profile during the negative surge with Q=20 l/s and a 30 mm gate opening

6.1.2 Turbulent velocities

The longitudinal velocities of the measured data were compared with the velocities of the simple wave methods, the numerical integration of the Saint-Venant equations and the outputs of the Flow-3D^{TM} simulations. The results are presented in Figure 6-2. The longitudinal velocities V_x were measured at z=6.69 mm, z=123.94 mm and z=135.2 mm. The Flow-3D^{TM} results for the model with 5 mm mesh size were output at locations closest to the measured z values. The V_x velocity component for the simple wave method and numerical integration of the Saint-Venant equations are the same for all vertical elevations. All the velocities in the figures below are presented in dimensionless time and dimensionless velocity components at x=6 m. The comparison of the simple wave method, the numerical integration of the Saint-Venant equations and the Flow-3D^{TM} simulation with experimental data showed that there is an increase in the longitudinal velocity components, as observed in all vertical locations.

However, the analytical method and the numerical integration generally overestimated the longitudinal velocity component V_x for all vertical elevations.

The longitudinal velocity at z=135.2 mm showed the best agreement of the simple wave methods and the numerical integration of the Saint-Venant equations with measured data. The analytical method and numerical integration of the Saint-Venant equations overestimated the longitudinal velocity component V_x close to the channel bed. Overall, the analytical method compared best with the recorded V_x velocity component of the negative surge. It replicated the longitudinal velocity trend at z=135.2 mm very closely. The numerical integration of the Saint-Venant equations using different Darcy friction factors compared reasonably well with the measured data. Generally, the results using the highest friction factor f=0.035 overestimated the velocities the most, while the results of the numerical integration of the Sain-Venant equations using the lowest Darcy friction factor f=0.015 compared better with the measured data. This confirms the assumption made in previous sections that for the experimental setup used in this the friction effect is negligible for the negative surge.

The Flow-3D^{TM} results generally underestimated the velocities for the negative surge for all vertical elevations. The velocities before the surge passage were a close match to the recorded data. The very initial stage of the surge propagation replicated the measured data well. The Flow-3D^{TM} simulation underestimated the velocities considerably during the surge passage for all vertical elevations. The Flow-3D^{TM} simulation compared best for z=123.94 mm, compared to z=6.69 mm and z=135.2 mm. The much lower V_x values during the surge propagation at z=6.69 mm suggested that the model did not represent the physical processes closest to the channel bed. This was consistent with velocities of the analytical and the numerical integration of the Saint-Venant equations, which showed the biggest differences closest to the channel bed when compared with measured data. The Flow-3D^{TM} results presented are for the model setup as discussed in section 5.2. A different model setup may lead to different findings.

In general, the simple wave methods produced good results when compared to the experimental data. It was also the least time consuming method tested in this study. The Flow-3D^{TM} models were easy to setup, however, the choice of input parameters required the user to have detailed knowledge of all the fluid properties. Also, Flow-3D^{TM} simulations were both time and computational intensive.

On the other hand, the simple wave method and the numerical integration of the Saint-Venant equations required an initial input time series for the boundary setup and therefore, would not be able to calculate the surge propagation without the availability of the input data.

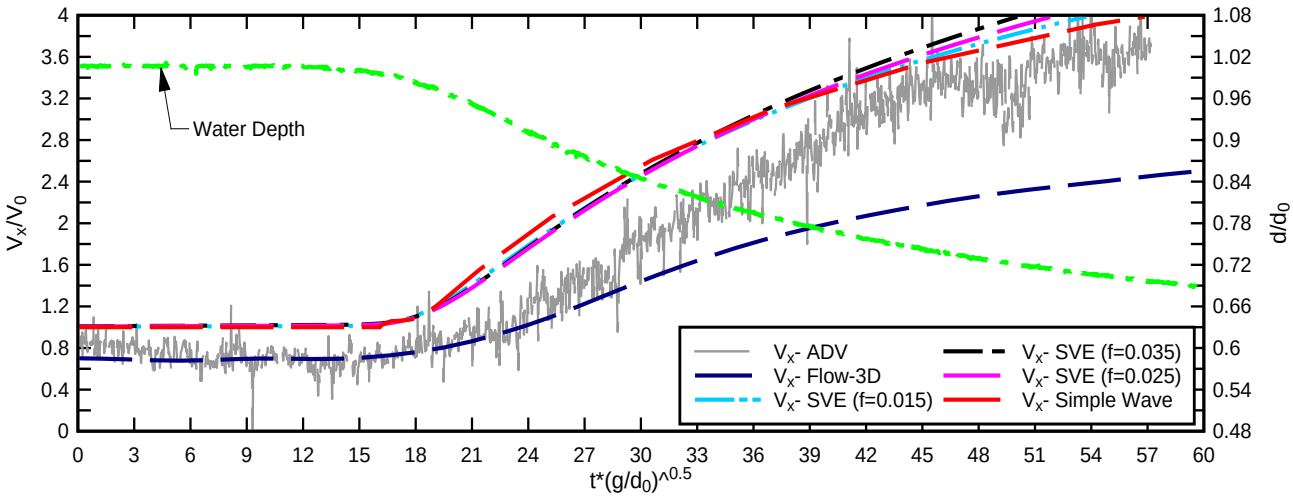

(a) z=6.69 mm, Q=20 l/s and 30 mm gate opening

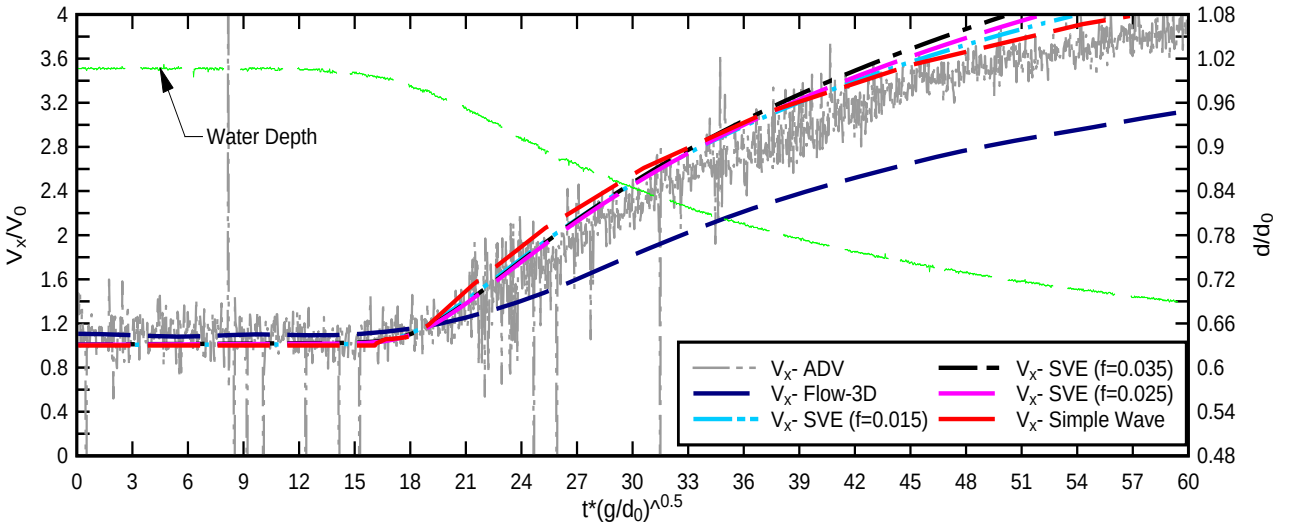

(b) z=123.94 mm, Q=20 l/s and 30 mm gate opening

Figure 6-2: Comparison of the dimensionless longitudinal velocity components V_x derived from analytical and numerical methods with measured data at x=6 m - Flow-3D™ calculations performed with 5 mm mesh size (cont'd).

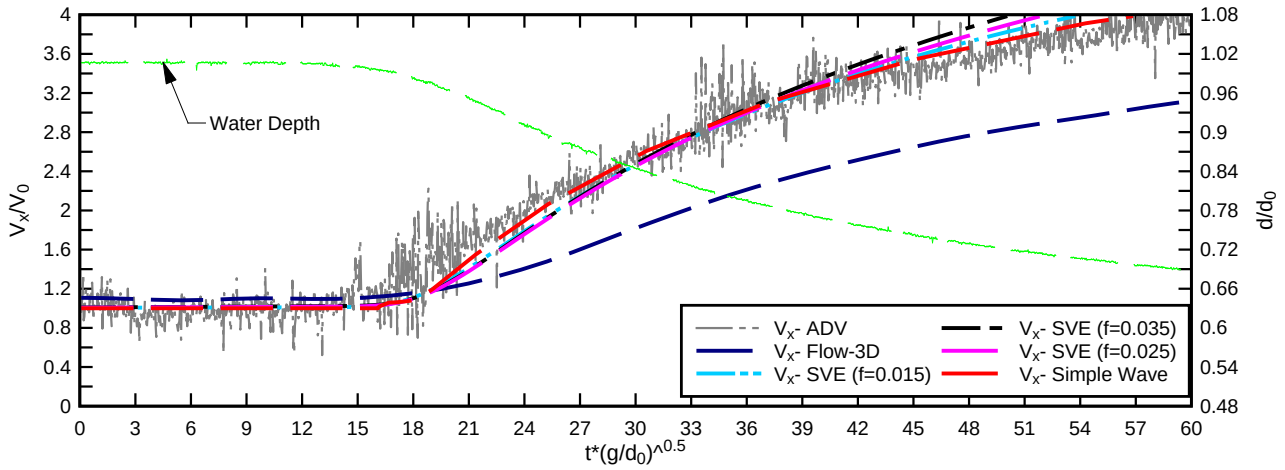

(c) z=135.2 mm, Q=20 l/s and 30 mm gate opening

Figure 6-2: Comparison of the dimensionless longitudinal velocity components V_x derived from analytical and numerical methods with measured data at x=6 m - Flow-3D™ calculations performed with 5 mm mesh size.

6.2 Positive surge

6.2.1 Surface profile

The simple wave method was used to obtain the analytical solution of the Saint-Venant equations for the positive surge. The result was compared to surface water profile data measured with acoustic displacement meters (Figure 6-3). The simple wave method did not provide good results for the positive surge. There was a difference of 7.8 s between the arrival of the surge front of the simple wave method and the physical data. In addition, the wave amplitude was much lower than the amplitude observed in the recorded data. The two-dimensional Flow-3D™ model was tested against physical data. The results are presented in Figure 6-3. There was a substantial difference between the timing of the initial surge formation between the three Flow-3D™ tests using 5 mm, 15 mm and 30 mm mesh sizes. The Flow-3D™ model with a mesh 15 mm mesh size replicated the timing of the initial surge formation the best, but it underestimated the wave amplitude. In the Flow-3D™ model with a uniform mesh size of 5 mm, the initial formation of the positive surge occurred much earlier than in the physical data. Although the wave amplitude was slightly larger than in the other two Flow-3D™ configurations, it was still fundamentally underestimated. The simple wave method and the Flow-3D™ simulation with a 5 mm mesh provided simular results regarding the wave amplitude. Overall, all three Flow-3D™ configurations and the simple wave methods did not compare well with the physical data.

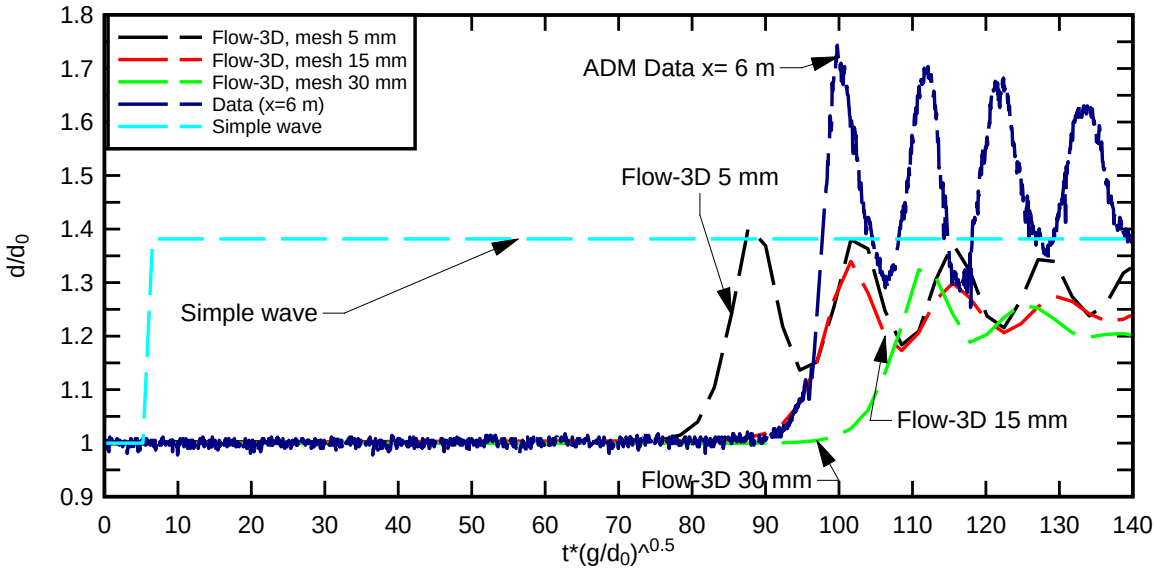

Figure 6-3: Unsteady free-surface profile during the positive surge

6.2.2 Turbulent velocities

The velocities of the Flow-3D^{TM} model with a 5 mm uniform mesh size were compared to experimental data. The Flow-3D^{TM} model with a 5 mm mesh size was chosen because it had a more detailed vertical velocity profile, compared to the 15 mm and 30 mm mesh size models. The results are shown in dimensionless terms in Figure 6-4.

The results of the Flow-3D simulations showed a sharp deceleration of the longitudinal velocity V_x, which was also observed in the physical data. Also, the results showed an undular velocity pattern that is similar to the recorded data. The measured velocity data were selected at z/d_0=0.1 and z/d_0=0.4. The Flow-3D^{TM} results, recorded a larger velocity at z/d_0=0.4 than at z/d_0=0.1. As expected, the velocities for the Flow-3D^{TM} model were smaller than the measured data. The sharp discontinuity in terms of the longitudinal velocities occurred earlier in the Flow-3D^{TM} model than in the measured data. This was consistent with the earlier timing of the initial surge formation (section 6.2.1). While the velocity at z=22.5 mm was close to the observed velocities, the velocity at z=7.5, was smaller than the experimental data. This might be linked with the smaller wave amplitude observed in the previous section.

Other studies, by Simon et al. (2011) and Lubin et al. (2010) found that the computation of positive surges using a CFD code may be impacted by boundary conditions.

While the results of these studies provided good agreement of the surge flow patterns, they also stated that the velocity profiles were not completely satisfying.

The presented data showed that the surge generation immediately upstream of the gate was an intense turbulent process, which cannot be modelled easily, with one-dimensional equations, or a limited CFD model.

The difficulty to compute an accurate velocity profile for a positive surge, results in the inaccuracy of the timing of the initial surge formation. It might be concluded that the velocity profile and the turbulent mixing in positive surges are much more complex than in negative surges. Also, the simulation of positive surges using CFD codes is still in its early stages and the results should be validated against physical data.

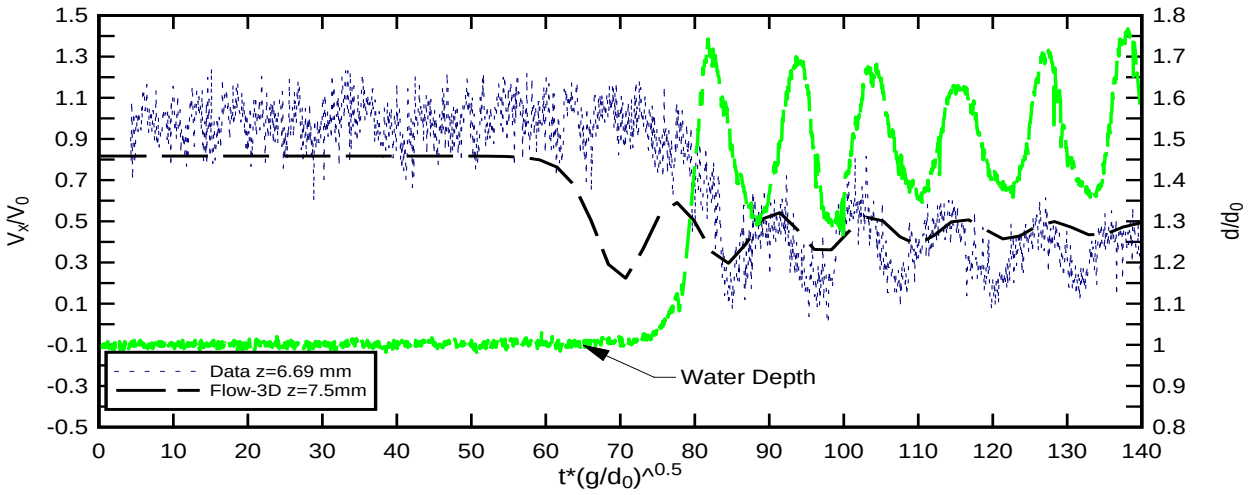

(a) z/d_0=0.1

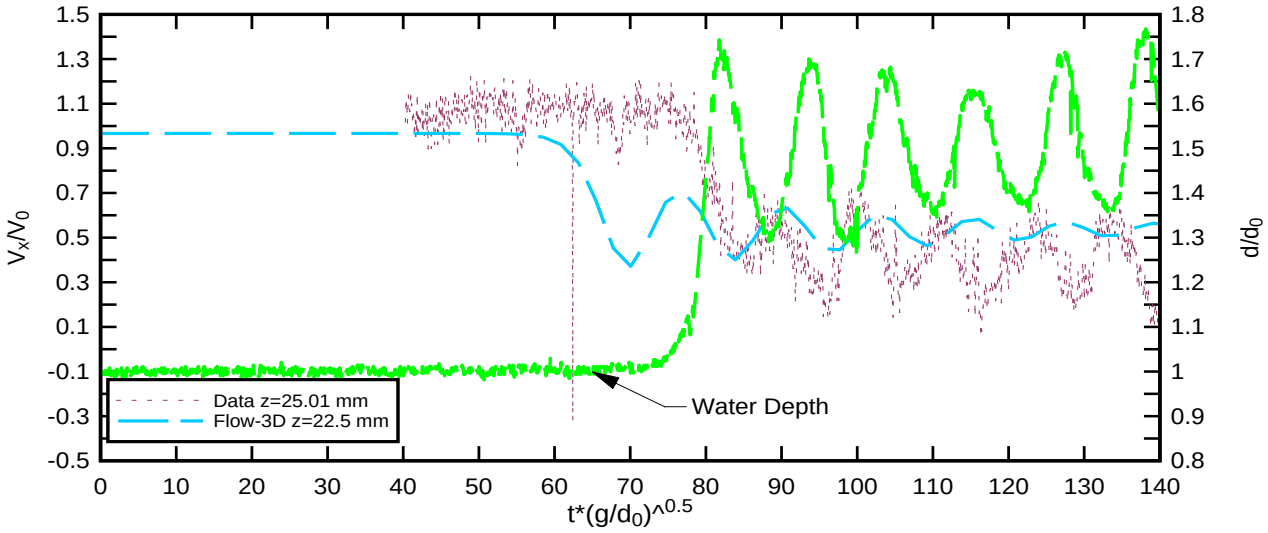

(b) z/d_0=0.4

Figure 6-4: Comparison of the dimensionless longitudinal velocity components V_x derived from analytical and numerical methods with measured data at x=6 m - Flow-3D calculations performed with 5 mm mesh size.

7 Conclusion

Unsteady open channel flow data were collected during the upstream propagation of negative and positive surges. Both, physical and numerical modelling, were performed. Some detailed measurements of free-surface fluctuations were recorded using non-intrusive techniques, including acoustic displacement meters and video recordings. Velocity measurements were sampled with high temporal and spatial resolution using an ADV (200 Hz) at four vertical elevations and two longitudinal locations. The velocity and water depth results were ensemble-averaged for both negative and positive surges. The results showed that the water curvature of the negative surge was steeper near the gate at x=10.5 m compared to further upstream at x=6 m. Both the instantaneous and ensemble-average data showed that in the negative surge the inflection point of the water surface and the longitudinal velocity V_x occurred simultaneously. Also, an increase in V_x was observed at all elevations during the surge passage. For the positive surge the propagation of the bore and the velocity fluctuations characteristics supported earlier findings by Koch and Chanson (2009) and Docherty and Chanson (2010). The surge was a major discontinuity in terms of the free-surface elevations, and a deceleration of the longitudinal velocities V_x was observed during the surge passage.

The free-surface profile was analysed analytically using the simple wave solution of the Saint-Venant equations. The analytical results in terms of water depth compared well with the experimental results at x=6 m for the negative surge, but provided poorer results for the positive surge. The numerical integration of the Saint-Venant equations compared reasonably well with the physical data for the negative surge, in terms of both water depth and longitudinal velocities. The longitudinal velocities where slightly overestimated resulting in the underestimation of water depth. For the negative surge, the results of Flow-3D^{TM} simulations compared reasonably well with the measured data, but underestimated the velocities resulting in an overestimation of the water surface. For the positive surge, the analytical method and the computational analysis using Flow-3D^{TM} did not compare well with the physical data. All the models underestimated the water depth at both the initial stage of the surge and during surge propagation. The simple wave solution and Flow-3D^{TM} simulation, with a uniform mesh size of 5 mm overestimated the velocities of the positive surge. The timing of the positive surge formation was best simulated by the Flow-3D^{TM} model with 15 mm mesh size.

This study had two aims. First, to analyse the propagation and velocity fluctuations characteristics of positive and negative surges, second, to validate the analytical and numerical techniques against the physical data sets.

The study resulted in a number of significant outcomes:

1. High quality benchmark data was collected. Complete data sets including simultaneous data for depth and velocity were collected specifically with high spatial and temporal resolution in unsteady open channel flows. The physical data provide a unique data set for future numerical model validation.
2. The study showed that theoretical models may be applied successfully to unsteady flow situations, with simple channel geometry. The theoretical models are often overlooked for more complex numerical methods to solve unsteady open channel flow situations. However, a theoretical model may provide better results in some unsteady flow situations in simple channel geometries as shown for the negative surge herein.
3. The one-dimensional (1D) modelling compared well with physical data and better than a more complex CFD model for the negative surge. Although one-dimensional modelling is popular in the engineering industry, some engineers believe that CFD modelling is more capable. This study showed that the numerical integration of the Saint-Venant equations compared well with the measured data for the negative surge, while CFD modelling did not match physical data in highly unsteady open channel flows within the setup used in this study.
4. The study showed that the selection of the appropriate mesh size for CFD simulations is critical and that a sensitivity analysis is essential for highly unsteady open channel flows, together with access to a solid validation data set. In the absence of quality validation data, the user would not be able to determine the appropriate mesh size, which might results in substantial differences of model outcomes.
5. The present experience demonstrated that the usage of a commercial CFD package requires some solid understanding of all the properties of the software, including the basic equations, the velocity fluctuations model(s) and the definition of the boundary conditions.

6. A negative surge is associated with a relative gentle decrease in water elevation. Although, the pressure distributions might not be hydrostatic at the leading edge of the surge, the Saint-Venant equations provide reasonably accurate predictions of the surge properties using both analytical and numerical approaches.
7. In a positive surge, the surge front is a sharp discontinuity in terms of water elevations, velocities and pressure. The present data showed that the surge generation immediately upstream of the gate is an intense turbulent process, which cannot be simply modelled neither, with one-dimensional equations nor a limited CFD model.
8. Highly unsteady open channel flows remain a challenge for professional engineers and researchers.

References

ARIC'O, C., NASELLO, C., and TUCCIARELLI, T. (2007). "A Marching in Space and Time (MAST) Solver of the Shallow Water Equations, Part II: The2-D model." *Adv. Water Res*., Vol. 30, No.5, pp. 1253–1271.

ALCRUDO, F. and SORARES FRAZAO, S. (1998). "Conclusions from 1st CADAM Meeting." *Proc. of 1st CADAM Meeting*, Paper 5, Wallingford.

ALTINAKAR, M.S., MATHEU, E.E, and MCGRANTH, M.Z. (2009a). "New Generation Modeling and Decision Support Tools for Studying Impacts of Dam Failures. Dam Safety 2009." *Proc., ASDSO 2009 Annual Conference,* Sept. 27-October 1, Hollywood, FL (CD-Rom). Association of State Dam Safety Officials, Lexington, KY.

BARRÉ de SAINT-VENANT, A.J.C. (1871a). "Théorie et Equations Générales du Mouvement Non Permanent des Eaux Courantes." *Comptes Rendus des séances de l'Académie des Sciences*, Paris, France, Séance 17 July 1871, Vol. 73, pp. 147-154.

BARRÉ de SAINT-VENANT, A.J.C. (1871b). "Théorie du Mouvement Non Permanent des Eaux, avec Application aux Crues de Rivières et à l'Introduction des Marées dans leur Lit." *Comptes Rendus des séances de l'Académie des Sciences*, Paris, France, Vol. 73, No. 4, pp. 237-240.

BAZIN, H. (1865a). "Recherches Expérimentales sur l'Ecoulement de l'Eau dans les Canaux Découverts." ('Experimental Research on Water Flow in Open Channels.') *Mémoires presents par divers savants à l'Académie des Sciences*, Paris, France, Vol. 19, pp. 1-494.

BAZIN, H. (1865b). "Recherches Expérimentales sur la Propagation des Ondes." ('Experimental Research on Wave Propagation.') *Mémoires présentés par divers savants à l'Académie des Sciences*, Paris, France, Vol. 19, pp. 495-644.

BENET, F., and CUNGE, J.A. (1971). "Analysis of Experiments on Secondary Undulations caused by Surge Waves in Trapezoidal Channels." *Jl of Hyd. Res.*, IAHR, Vol. 9, No. 1, pp. 11-33.

BENJAMIN, T.B., and LIGHTHILL, M.J. (1954). "On Cnoidal Waves and Bores." *Proc. Royal Soc. Of London, Series A, Math. & Phys. Sc.*, Vol. 224, No. 1159, pp. 448-460.

BISCARINI, C., DI FRANCESCO, S. and MANCIOLA P. (2009). “CFD Modelling Approach for Dam Break Flow Studies.” *Hydrol. Earth Syst. Sci.*, Vol. 14, pp.705–718.

BOUSSINESQ, J.V. (1877). "Essai sur la Théorie des Eaux Courantes." ('Essay on the Theory of Water Flow.') *Mémoires présentés par divers savants à l'Académie des Sciences*, Paris, France, Vol. 23, Série 3, No. 1, supplément 24, pp. 1-680.

CAVAILLE, Y. (1965). "Contribution à l'Etude de l'Ecoulement Variable Accompagnant la Vidange Brusque d'une Retenue." ('Contribution to the Study of Unsteady Flow Following a Dam Break.') *Publ. Scient. et Techn. du Ministère de l'Air*, No. 410, Paris, France, 165 pages.

CHANSON, H. (1995). "Flow Characteristics of Undular Hydraulic Jumps. Comparison with Near-Critical Flows." *Report CH45/95*, Dept. Of Civil Engineering, University of Queensland, Australia, June, 202 pages.

CHANSON, H., AOKI, S., and MARUYAMA, M. (2000). "Experimental Investigations of Wave Runup Downstream of Nappe Impact. Applications to Flood Wave Resulting from Dam Overtopping and Tsunami Wave Runup." *Coastal/Ocean Engineering Report*, No. COE00-2, Dept. of Architecture and Civil Eng., Toyohashi University of Technology, Japan, 38 pages.

CHANSON, H. (2004). "The Hydraulics of Open Channel Flows: An Introduction." *Butterworth-Heinemann*, Oxford, UK, 2nd edition, 630 pages.
{http://www.uq.edu.au/~e2hchans/reprints/book3_2.htm}

CHANSON, H. (2005). "Le Tsunami du 26 Décembre 2004: un Phénomène Hydraulique d'Ampleur Internationale. Premier Constats." ('The 26 December 2004 Tsunami: a Hydraulic Engineering Phenomenon of International Significance. First Comments') *Jl La Houille Blanche, No. 2, pp. 25-32.*

CHANSON, H. (2010). "Unsteady Turbulence in Tidal Bores: the Effects of Bed Roughness." *Journal of Waterway, Port, Coastal, and Ocean Engineering*, ASCE, Vol. 136 (ISSN 0733-950X).

CHANSON, H. (2011). "Turbulent Shear Stresses in Hydraulic Jumps, Bores and Decelerating Surges.” *Earth Surf. Processes*, Vol. 36, pp.180-189.

CUNGE, J.A., F.M. HOLLY and Jr. and A. VERWEY (1980*). "*Practical Aspects of Computational River Hydraulics. *London, Pitman.*

CUNGE, J.A. (2003). Undular bores and secondary waves -experiments and hybrid finite-volume modelling.*"J. Hyd. Res.,* IAHR, Vol 41, No.5,pp. 557–558.

DE MAIO, A., SAVI, F., and SCLAFANI, L (2004). "Three-dimensional Mathematical Simulation of Dambreak Flow." *Proceeding of IASTED conferences – Environmental Modelling and Simulation* ISBN: 0-88986-441-1 St. Thomas, US Virgin Island.

DE MARCHI, G. (1945). "Ondi di depressione provocato da apperatura di paratoia in un canale in definito." *L'Energia Elettrica* , Vol. 22(1/2), pp. 1-13.

DOCHERTY, N.J., and CHANSON, H. (2010). "Characterisation of Unsteady Turbulence in Breaking Tidal Bores including the Effects of Bed Roughness." *Hydraulic Model Report No. CH76/10*, School of Civil Engineering, The University of Queensland, Brisbane, Australia, 112 pages.

DRESSLER, R.F. (1952). "Hydraulic Resistance Effect upon the Dam-Break Functions." *Jl of Research, Natl. Bureau of Standards*, Vol. 49, No. 3, pp. 217-225.

DRESSLER, R. (1954). "Comparison of Theories and Experiments for the Hydraulic Dam-Break Wave." *Proc. Intl Assoc. of Scientific Hydrology Assemblée Générale*, Rome, Italy, Vol. 3, No.38, pp. 319-328.

ESTRADE, J. (1967). "Contribution à l'Etude de la Suppression d'un Barrage. Phase Initiale de l'Ecoulement." ('Contribution to the Study of Dam Break. Initial Stages of the Wave.') *Bulletin de la Direction des Etudes et Recherches*, Series A, Nucléaire, Hydraulique et Thermique, EDF Chatou, France, No. 1, pp. 3-128.

ESTRADE, J., and MARTINOT-LAGARDE, A. (1964). "Ecoulement Consécutif à la Suppression d'un Barrage dans un Canal Horizontal de Section Rectangulaire." ('Dam Break Wave Flow in a Horizontal Rectangular Canal.') *Comptes-Rendus de l'Académie des Sciences de Paris*, Vol. 259, 21 December, Group 2, pp. 4502-4505.

FAVRE, H. (1935). "Etude Théorique et Expérimentale des Ondes de Translation dans les Canaux Découverts." ('Theoretical and Experimental Study of Travelling Surges in Open Channels.') *Dunod*, Paris, France.

FAURE, J., and NAHAS, N. (1961). "Etude Numérique et Expérimentale d'Intumescences à Forte Courbure du Front." ('A Numerical and Experimental Study of Steep-Fronted Solitary Waves.')*Jl La Houille Blanche*, No. 5, pp. 576-586. Discussion: No. 5, p. 587.

FLOW SCIENCE, INC. (2007). "*Flow-3D User's Manuals*", Version 9.2, Santa Fe, NM

FRACCAROLLO, L. and TORO, E. F.(1995). "Experimental and Numerical Assessment of the Shallow Water Model for Two-Dimensional Dam-Break Problems, *Jl. Hydr. Res*., Vol. 33, pp. 843–864.

FURUYAMA, S.I. and CHANSON, H. (2010). "A numerical simulation of a tidal bore flow." *Costal Engineering Journal,* Vol. 52, No. 3, pp.215-234.

G'OMEZ-GESTEIRA, M. and DALRYMPLE, R. A. (2004). "Using a Three Dimensional Smoothed Particle Hydrodynamics Method for Wave Impact on a Tall Structure. "J*. Waterway, Port, Coastal and Ocean Eng.*, Vol. 130, No. 2, pp. 63–69.

GORING, D.G., and NIKORA, V.I. (2002). "Despiking Acoustic Doppler Velocimeter Data." *Jl of Hyd. Engrg*., ASCE, Vol. 128, No. 1, pp. 117-126. Discussion: Vol. 129, No. 6, pp.484-489.

HENDERSON, F.M. (1966). "Open Channel Flow." *MacMillan Company*, New York, USA.

HORMADKA, T. V., BERENBROCK, C. E., FRECKLETON, J. R., and GUYMON, G. L (1985). "A Two-Dimensional Dam-Break Flood Plain Model, *Adv. Wat. Res.*, Vol. 8, 7–14 March.

HORNUNG, H.G., WILLERT, C., and TURNER, S. (1995). "The Flow Field Downstream of a Hydraulic Jump." *Jl of Fluid Mech.*, Vol. 287, pp. 299-316.

JIN, M and D. L. FREAD (1997). "Dynamic flood routing with explicit and implicit numerical solution schemes." *Jl of Hyd. Engrg*, ASCE, Vol. 123, No.3,pp. 166-173.

KOCH, C., and CHANSON, H. (2005). "An Experimental Study of Tidal Bores and Positive Surges: Hydrodynamics and Turbulence of the Bore Front." *Report No. CH56/05*, Dept. of Civil Engineering, The University of Queensland, Brisbane, Australia, July, 170 pages.

KOCH, C., and CHANSON, H. (2009). "Turbulence Measurements in Positive Surges and Bores." *Jl of Hyd. Res.*, IAHR, Vol. 47, No. 1, pp. 29-40.

LAUBER, G. (1997). "Experimente zur Talsperrenbruchwelle im glatten geneigten Rechteckkanal." ('Dam Break Wave Experiments in Rectangular Channels.') *Ph.D. thesis*, VAW-ETH, Zürich,Switzerland. (also *Mitteilungen der Versuchsanstalt fur Wasserbau, Hydrologie und Glaziologie*, ETH-Zurich, Switzerland, No. 152).

LAUBER, G., and HAGER, W.H. (1998). “Experiment to Dambreak Wave: Horizontal Channel.” *Jl of Hyd. Res*., IAHR, Vol. 36, No. 3, pp. 291-307.

LEMMIN, U., and LHERMITTE, R. (1999). “ ADV Measurements of Turbulence: can we Improve their Interpretation? Discussion.” *Jl of Hyd. Engrg*., ASCE, Vol. 125, No. 6, pp. 987-988.

LEMOINE, R. (1948). "Sur les Ondes Positives de Translation dans les Canaux et sur le Ressaut Ondulé de Faible Amplitude." ('On the Positive Surges in Channels and on the Undular Jumps of Low Wave Height.') *Jl La Houille Blanche*, Mar-Apr., pp. 183-185.

LEWIS, A.W. (1972). "Field Studies of a Tidal Bore in the River Dee." *M.Sc. thesis*, Marine Science Laboratories, University College of North Wales, Bangor, UK.

LEVIN, L. (1952). "Mouvement Non Permanent sur les Cours d'Eau à la Suite de Rupture de Barrage." ('Unsteady Flow Motion Induced by a Dam Break.') *Revue Générale de l'Hydraulique*, Vol. 18, pp. 297-315.

LIANG, D., LIN, B., and FALCONER, R. A. (2007). “Simulation of Rapidly Varying Flow Using an Efficient TVD-MacCormack Scheme.” *Int. J. Numer. Meth. Fl*., Vol. 53, pp.811–826.

LIGGETT, J.A. (1994). "Fluid Mechanics." *McGraw-Hill*, New York, USA.

LUBIN, P., GLOCKNER, S. and CHANSON, H. (2010). “Numerical simulation of a weak breaking tidal bore.” *Mech. Res. Comm.,* Vol.37, pp.119-121.

MADSEN, A., SVENDSEN, I.A and PAN, C.H. (2005). “Numerical simulation of tidal bores and hydraulic jumps. “ *Costal Eng.,* Vol. 52, pp. 409-433.

MANCIOLA, P., MAZZONI, A., and SAVI, F. (1994). ”Formation and Propagation of Steep Waves: An Investigative Experimental Interpretation.” *Proceedings of the Specialty Conference Co-sponsored by ASCE-CNR/CNDCI-ENEL Spa*, Milan, Italy, 29 June–1 July.

MARTIN, H. (1983). “Dam-break Wave in Horizontal Channels with Parallel and Divergent Side Walls.” 20 *IAHR Congress* Moscow 2, pp.494-505.

MENENDEZ, A.N., and NAVARRO, F. (1990). “An Experimental Study of the Continuous Breaking of a Dam.” *Jl of Hyd. Res*., IAHR, Vol.28, No.6, pp.753-772.

McLELLAND, S.J., and NICHOLAS, A.P. (2000).”A New Method for Evaluating Errors in High-Frequency ADV Measurements.” *Hydrological Processes*, Vol.14, pp.351-366.

MOHAMMANDI, M.(2008). “Boundary Shear Stress Around Bridge Piers.” *Am. J. Appl. Sci*., Vol. 5, No.11, pp. 1547–1551.

MONTES, J.S. (1998). "Hydraulics of Open Channel Flow." *ASCE Press*, New-York, USA, 697pages.

NAGATA, N., HOSODA, T., NAKATO, T., and MURAMOTO, Y. (2005). “Three-Dimensional Numerical Model for Flow and Bed Deformation around River Hydraulic.” *Jl. Hyd. Engrg*.-ASCE, Vol. 131, No.12, pp. 1074– 1087.

PEREGRINE, D.H. (1966). "Calculations of the Development of an Undular Bore." *Jl. Fluid Mech.*, Vol 25, pp.321-330.

QUECEDO, M., PASTOR, M., HERREROS, M.I., FERNANDEZ MERODO, J. A., and ZHANG, Q. (2005). Comparison of Two Mathematical Models for Solving the Dam Break Problem Using the FEM Method.” *Comput. Method Appl. M.*, Vol. 194, No. 36–38, pp. 3984–4005.

RAJAR, R. (1973). “ Modèle Mathematique et Abaques sans Dimensions pour la Determination de L’écoulement qui suit la Rupture d’un Barrage.” *ICOLD Congress*, Madrid Q40(R34), pp. 503-521.

SANDER, J and HUTTER, K (1991). “On the development of the theory of the solitary wave. A historical essay,” *Acta Mech.*, Vol. 86, pp. 111–152.

SCHOKLITSCH, A. (1917). “Über Dambruchwellen." *Sitzungberichten der Königliche Akademie der Wissenschaften, Vienna*, Vol. 126, Part IIa, pp. 1489-1514.

SERRE, F. (1953). "Contribution à l'Etude des Ecoulements Permanents et Variables dans les Canaux." ('Contribution to the Study of Permanent and Non-Permanent Flows in Channels.') *Jl La Houille Blanche*, Dec., pp. 830-872.

SIMON, B., LUBIN, P., GLOCKNER, S., and CHANSON, H. (2011). "Three-Dimensional Numerical Simulation of the Hydrodynamics generated by a Weak Breaking Tidal Bore." *Proc. 34th IAHR World Congress*, Brisbane, Australia, 26 June-1 July, Engineers Australia Publication, Eric VALENTINE, Colin APELT, James BALL, Hubert CHANSON, Ron COX, Rob ETTEMA, George KUCZERA, Martin LAMBERT, Bruce MELVILLE and Jane SARGISON Editors, pp. 1133-1140.

SOAREZ FRAZAO, S. and ZECH, Y (2002). "Dam Break in Channels with 90 °bend*." Jl of Hyd. Engrg* -ASCE, Vol.128, No.11, pp. 956–968.

SOBEY, R.J. and DINGEMANS, M.W. (1992). "Rapidly varied flow analysis of undular bore."*J. Waterway, Port, Coastal and Ocean Engrg.,* ASCE, Vol. 118, No.4, 417–436.

STRELKOFF, T. S and H. T. FALVEY (1993). "Numerical method used to model unsteady canal flow." *Jl. of Hyd. Engrg.*, ASCE, Vol. 119, No. 4, pp. 637-655.

TAN, L. and CHU, V.H. (2010). "Lauber and Hager's Dam-break Wave Data for Numerical Model Validation." *Jl of Hyd. Res*., Vol. 47, No.4, pp.524-528.

TELES DA SILVA, A.F. and PERERINE, D.H. (1990). "Nonsteady computations of undular and breaking bores." *Proceeding of the 22nd International Congress Coastal Engineering*, Delft, The Netherlands, ASCE Publ., Vol. 1, pp. 1019–1032.

TOOMBES, L. and CHANSON, H. (2011). "Numerical Limitations of Hydraulic Models." *Proc. 34th IAHR World Congress*, Brisbane, Australia, 26 June-1 July, Engineers Australia Publication, Eric VALENTINE, Colin APELT, James BALL, Hubert CHANSON, Ron COX, Rob ETTEMA, George KUCZERA, Martin LAMBERT, Bruce MELVILLE and Jane SARGISON Editors, pp. 2322-2328.

TRESKE, A. (1994). "Undular Bores (Favre-Waves) in Open Channels - Experimental Studies." *Jl of Hyd. Res.*, IAHR, Vol. 32, No. 3, pp. 355-370. Discussion: Vol. 33, No. 3, pp. 274-278.

TRICKER, R.A.R. (1965*)."* Bores, Breakers, Waves and Wakes*." American Elsevier Publ. Co.,* NewYork, USA*.*

TRIFFONOV, E.K. (1935). "Etudes Expérimentales de la Propagation d'une Onde Positive le Long d'un fond sec. "Bulletin des Congrès de Navigation, Bruxelles 10(19), pp. 66-77.

US CORPS OF ENGINEERS (1960). “Floods Resulting from Suddenly Breached Dams. Miscellaneous Paper 2 (374), Report 1. UA Army Engineers Waterways Experiment Station, Corps of engineers: Vicksburg, Mississippi.

VOULGARIS, G. and TOWNBRIDGE J.H. (1998). “Evaluation of the Acoustic Doppler Velocimeter (ADV) for Turbulence Measurements.” *J. Atmos. Oceanic. Technol,* Vol 15,pp. 272-289.

WHAL, T.L. (2003). “Despiking Acoustic Doppler Velocimeter Data. Discussion.” *Jl of Hyd. Engrg*., ASCE, Vol. 129, No. 6, pp. 484-487.

WILKINSON, D.L. and BANNER, M.L. (1977). “Undular bores.” *Proceeding of 6th Australasian Hydraulic and Fluid Mechanics Conference*, Adelaide, Australia, 369–373.

XANTHOPOULOS, T. and KOUTITAS, C (1976). “Numerical Simulation of a Two Dimensional Flood Wave Propagation Due to Dam-Failure, *J. Hyd. Res*., Vol. 14, No. 4, pp. 321–331.

YEH, H.H. and MOK, K.M. (1990). “On turbulence in bores.” *Physics of Fluids*, Series A, Vol.2, No.5, 821–828.

ZHANG W. and W. SUMMER (1994). “Computation of rapidly varied unsteady flows in open channels and comparison with physical model and field experiments.” *Hydroinformatics ’94*, A. Verwey, A. M. Minns, V. Babovic & C. Maksimovic (eds), Balkema, Rotterdam 731-737.

ZIENKIEWICZ, O.C. and SANDOVER, J.A. (1957). “The undular surge wave.” *Proceeding of the 7th IAHR Congress*,, Lisbon, Portugal, Vol. II, paper D25, D1–11.

Appendix A – Photographs of the experiments

A-1Presentation

New experiments were performed in the hydraulic laboratory at the University of Queensland. The channel was horizontal, 12 m long and 0.5 m wide. The sidewalls were made of 0.45 m high glass panels and the bed was made of 12 mm thick PVC sheets.

Notation

d_o	initial reservoir height (m) measured normal to the chute invert;
L	channel length (m);
Q	volume flow rate (m^3/s);
V_o	initial velocity (m/s);
W	channel width (m);
x	longitudinal distance (m) measured from the upstream end;

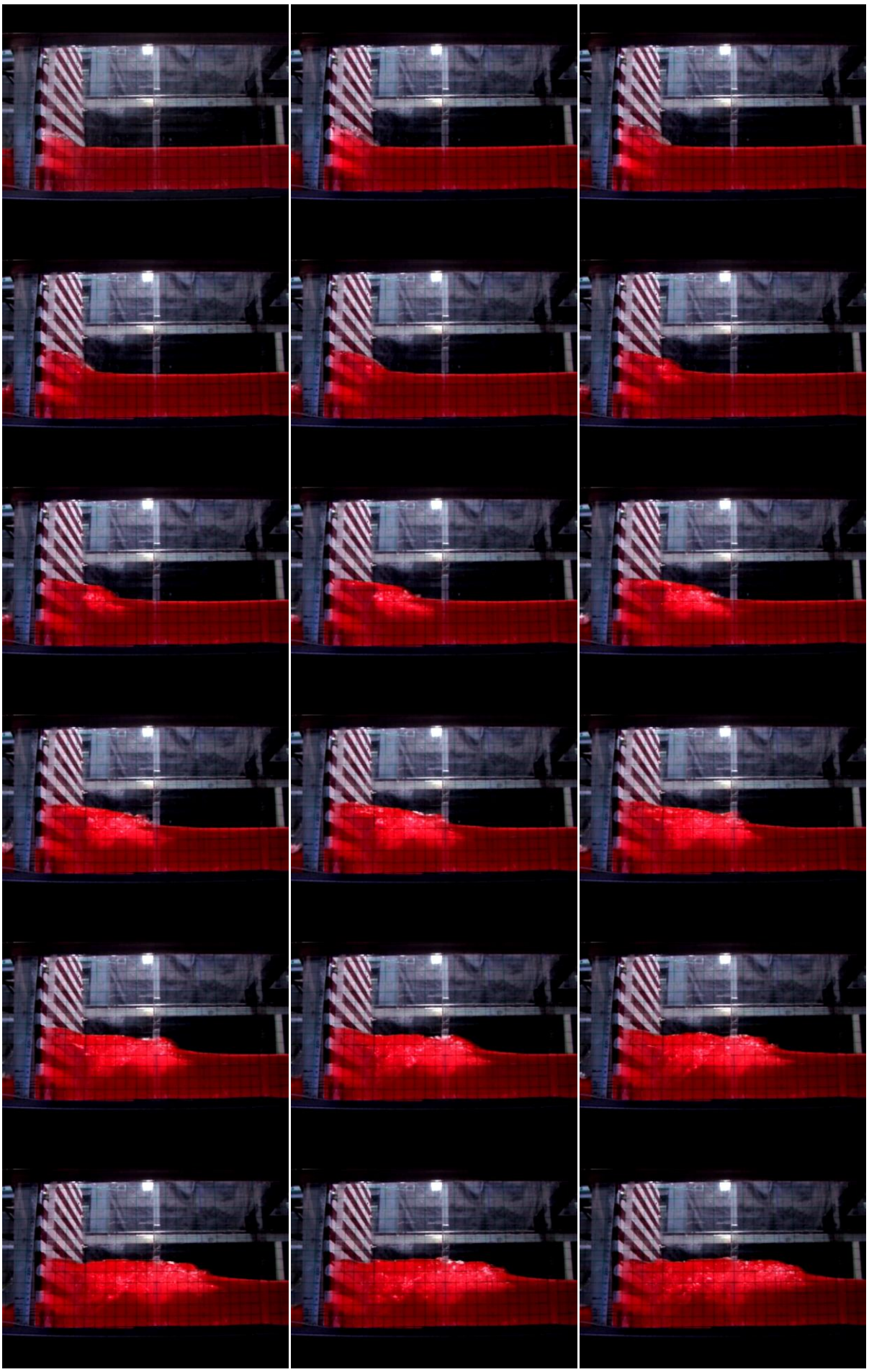

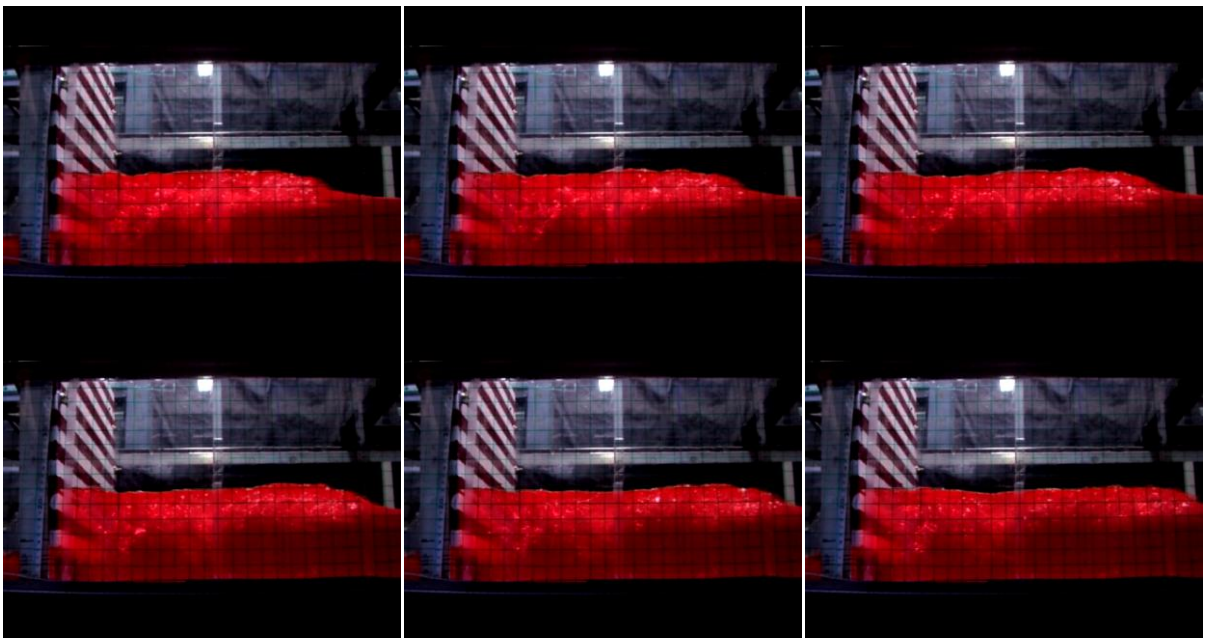

Figure A-1: Propagation of a positive surge – Q=30 l/s, d_0=6.4 cm, 25 frames per second, initial gate opening of 40 mm and 11.2< x <10.48 m

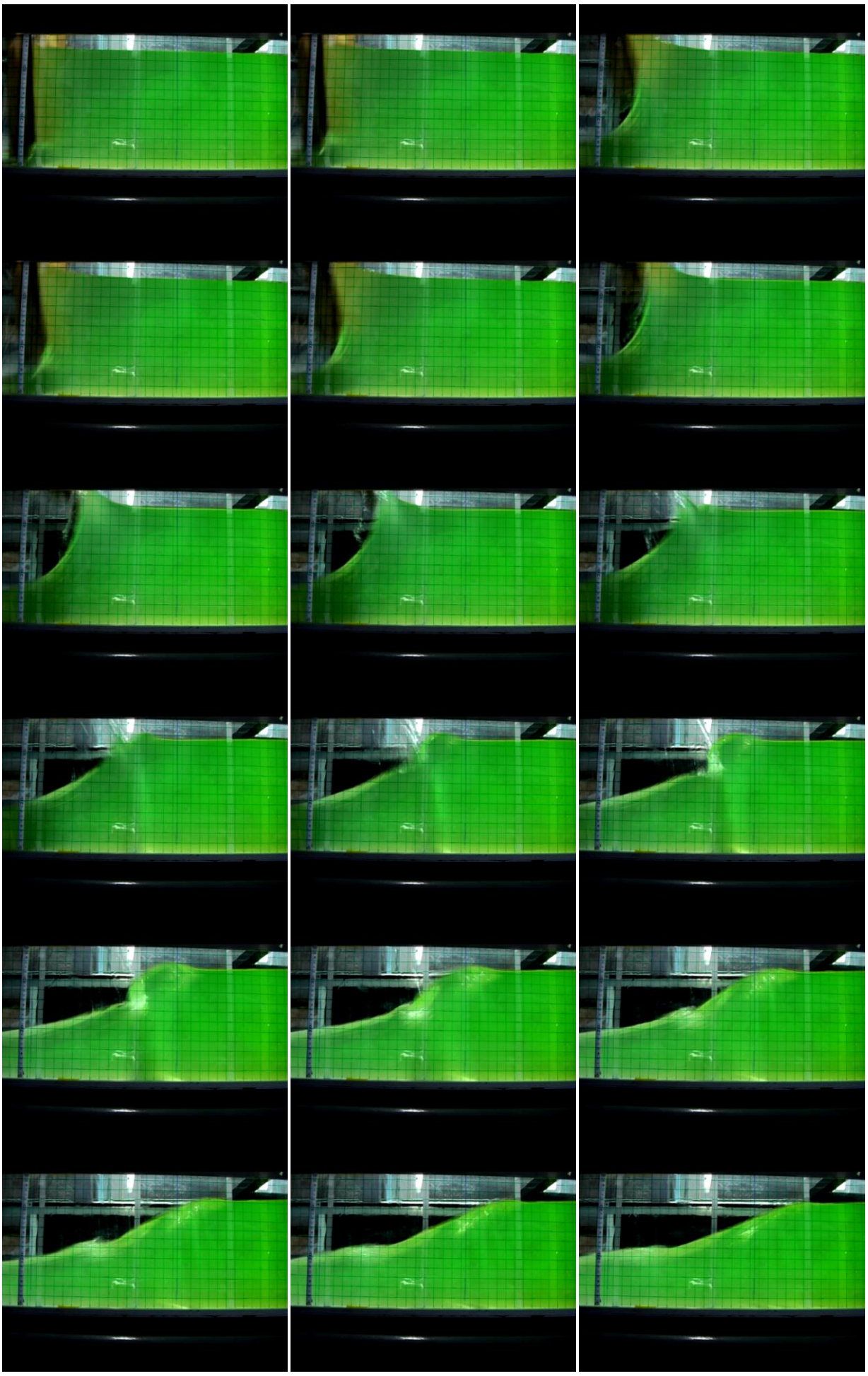

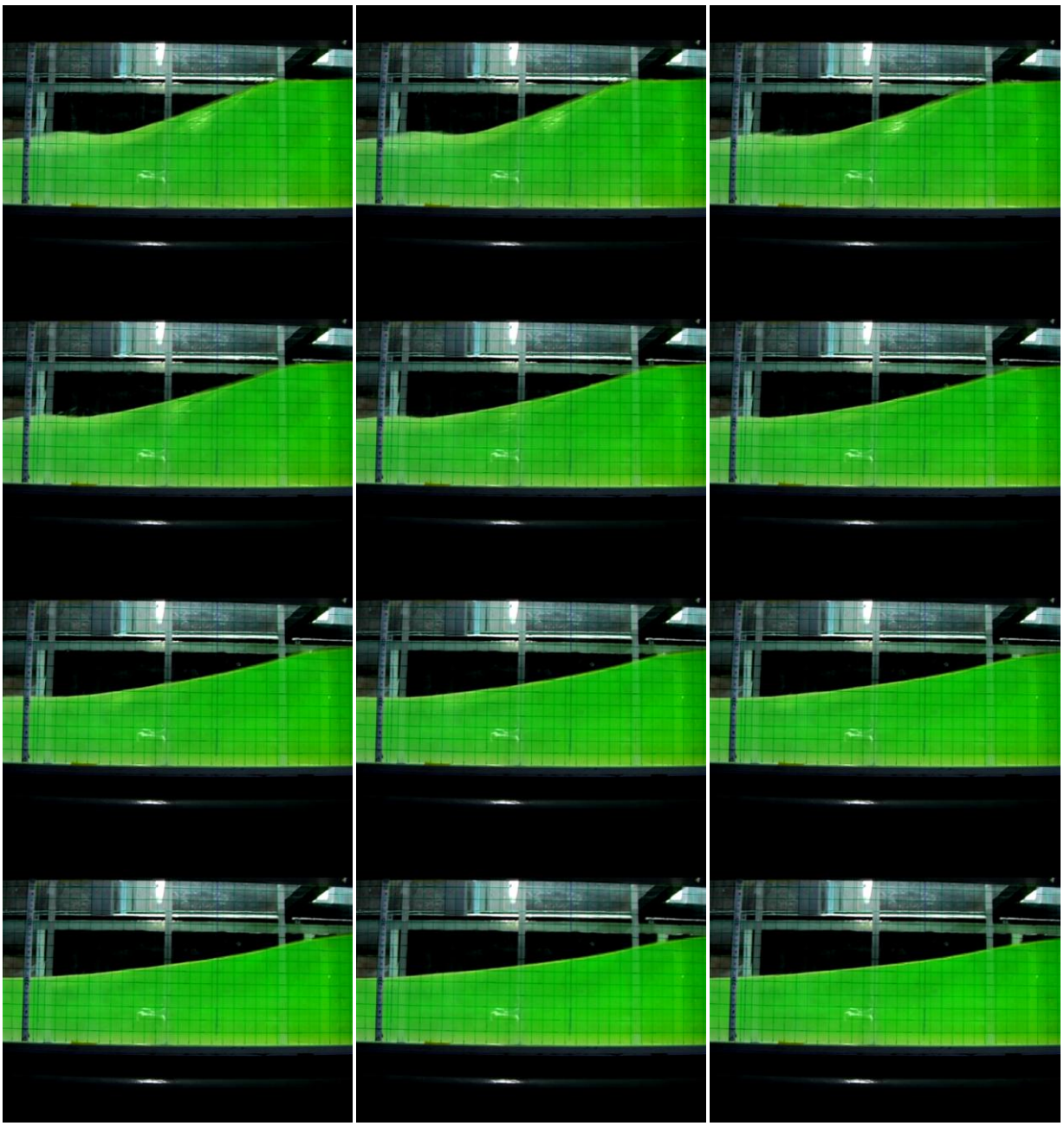

Figure A-2: Propagation of a negative surge – Q=20 l/s, d_0=26 cm, 25 frames per second, initial gate opening of 40 mm and 11.2< x <10.48 m

Appendix B - Ensemble-average results - negative surge

B-1.Presentation

A series of 25 instantaneous velocity records were prepared at four vertical locations above the smooth PVC bed. The acoustic Doppler velocimeter (ADV) sampled the instantaneous velocity component s on the channel centreline at x=10.5 m and x=6 m and four vertical sampling locations z=6.69 mm, 25.01 mm, 123.94 mm and 135.2 mm.

Notations

d_o	initial reservoir height (m) measured normal to the chute invert;
Q	volume flow rate (m^3)
V_o	initial velocity (m/s);
x	longitudinal distance (m) measured from the upstream end;

B2. Experimental results

An ensemble-median of each instantaneous velocity component was produced for each vertical elevation of the ADV measurements. All the negative surge data were synchronised based on the characteristic time t_3 which is further illustrated in Figure B-1. The instantaneous depth data was plotted for every run of the 25 runs and the first derivate was calculated. The data was then filtered using a 0-1 Hz band pass.

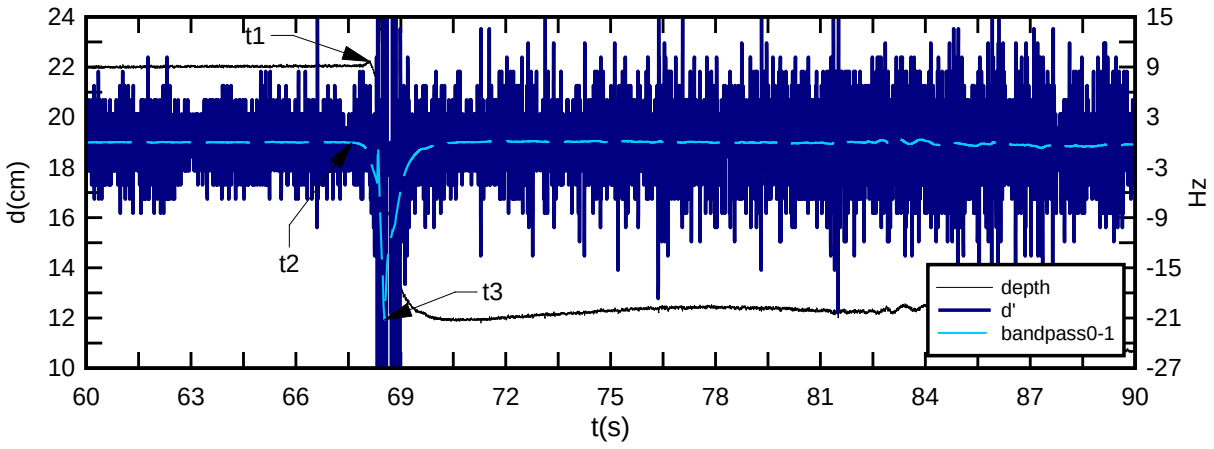

Figure B-1: Instantaneous water depth measurement, water depth derivative and band pass (0-1 Hz) for synchronisation purposes for the negative surge

The experimental results are shown in terms of ensemble-averaged median velocity component as a function of time. Each graph includes the ensemble-averaged median velocity component (V_x, V_y, V_z) the range of maximum to minimum velocities, the differences between the 3rd and 4th quartiles (V_{75}-V_{25}) and 90% and 10% percentiles, (V_{90}-V_{10}) and the ensemble-averaged water depth, d_{Median}.

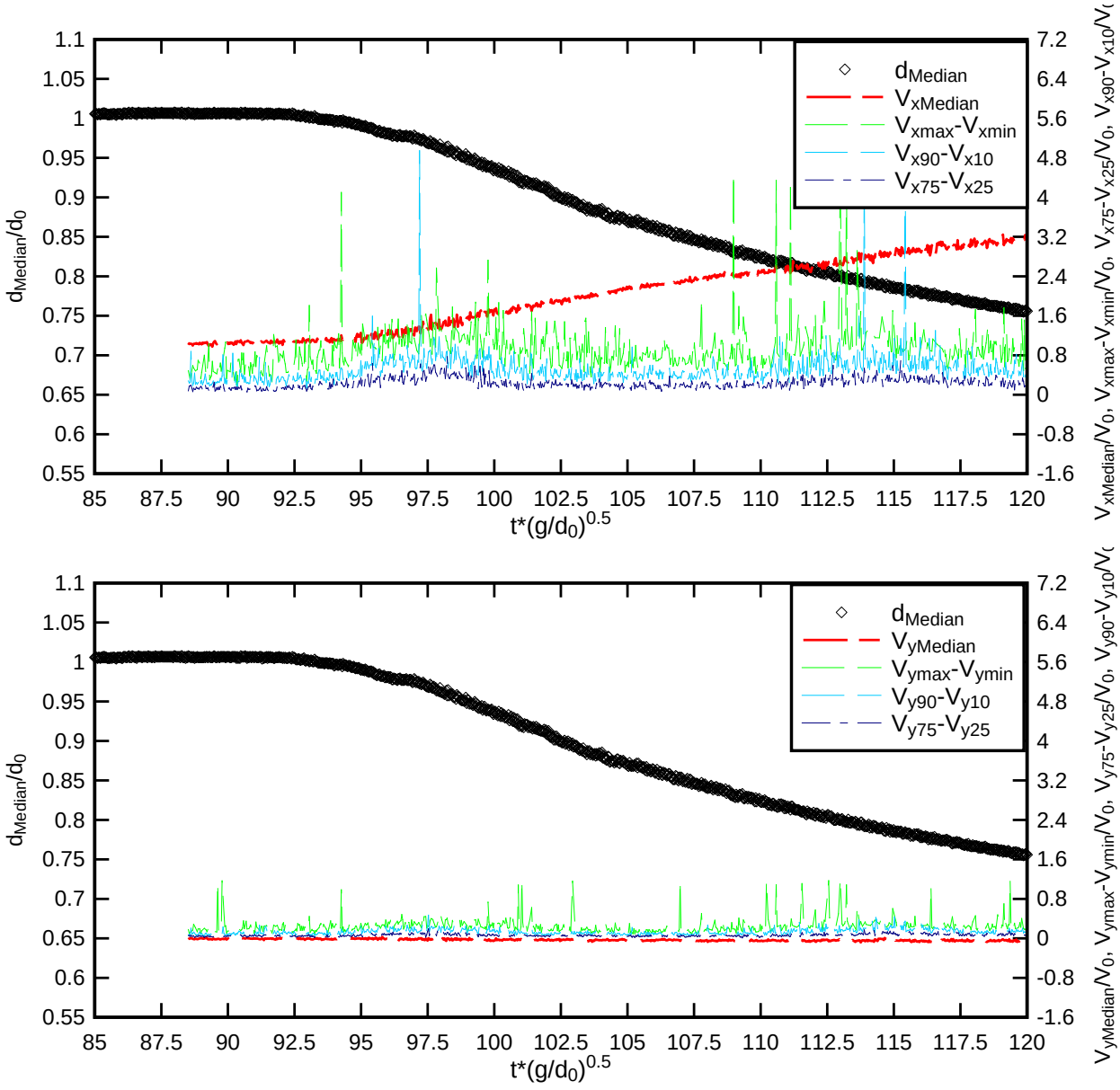

(a) z=123.94 mm, x=6 m (con't)

Figure B-3: Dimensionless ensemble-average median velocity $V_{yMedian}$, difference between 3rd and 4th quartiles (V_{75}- V_{25}) and 90% and 10% percentiles (V_{90}- V_{10}), and range of maximum to minimum velocities (V_{max}- V_{min}) at x=6 m- From Top to bottom V_x, V_y, V_z (con't)

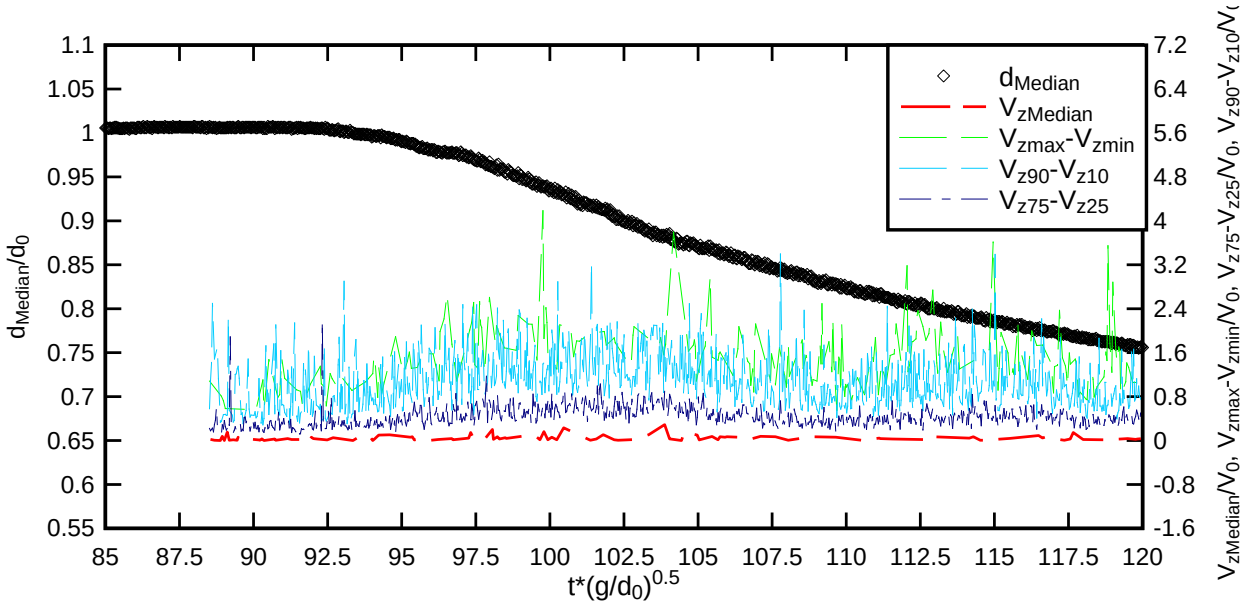

(a) z=123.94 mm, x=6 m

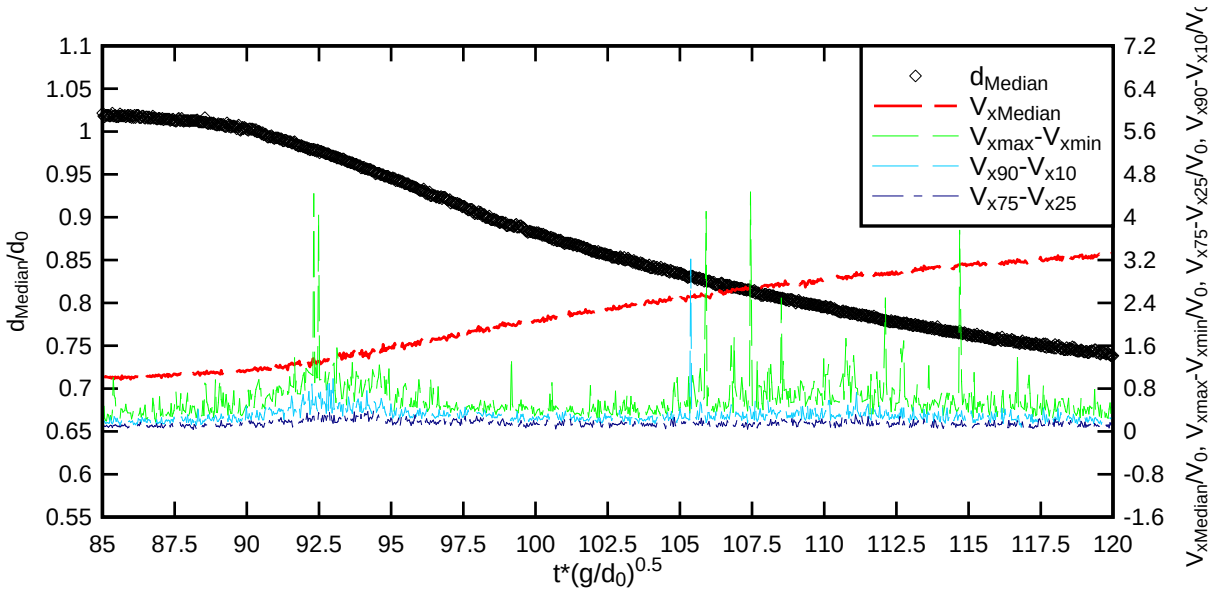

(b) z= 135.2 mm, x=6 m (con't)

Figure B-3: Dimensionless ensemble-average median velocity $V_{yMedian}$, difference between 3rd and 4th quartiles (V_{75}- V_{25}) and 90% and 10% percentiles (V_{90}- V_{10}), and range of maximum to minimum velocities (V_{max}- V_{min}) at x=6 m- From Top to bottom V_x, V_y, V_z (con't)

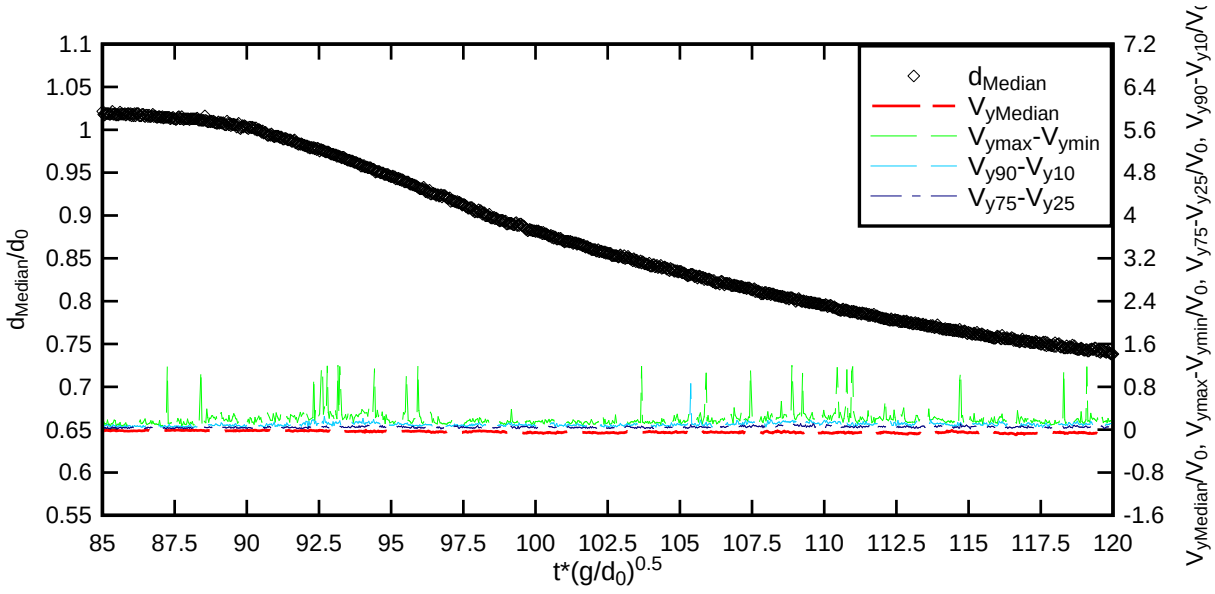

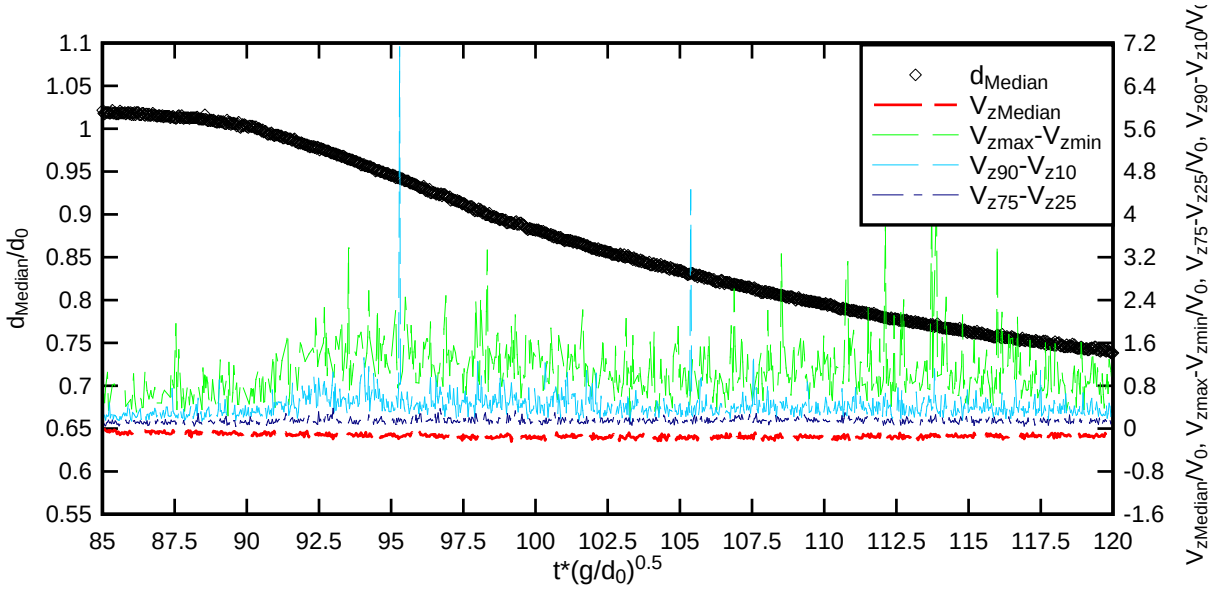

(b) z= 135.2 mm, x=6 m

Figure B-3: Dimensionless ensemble-average median velocity $V_{yMedian}$, difference between 3rd and 4th quartiles (V_{75}- V_{25}) and 90% and 10% percentiles (V_{90}- V_{10}), and range of maximum to minimum velocities (V_{max}- V_{min}) at x=6 m- From Top to bottom V_x, V_y, V_z

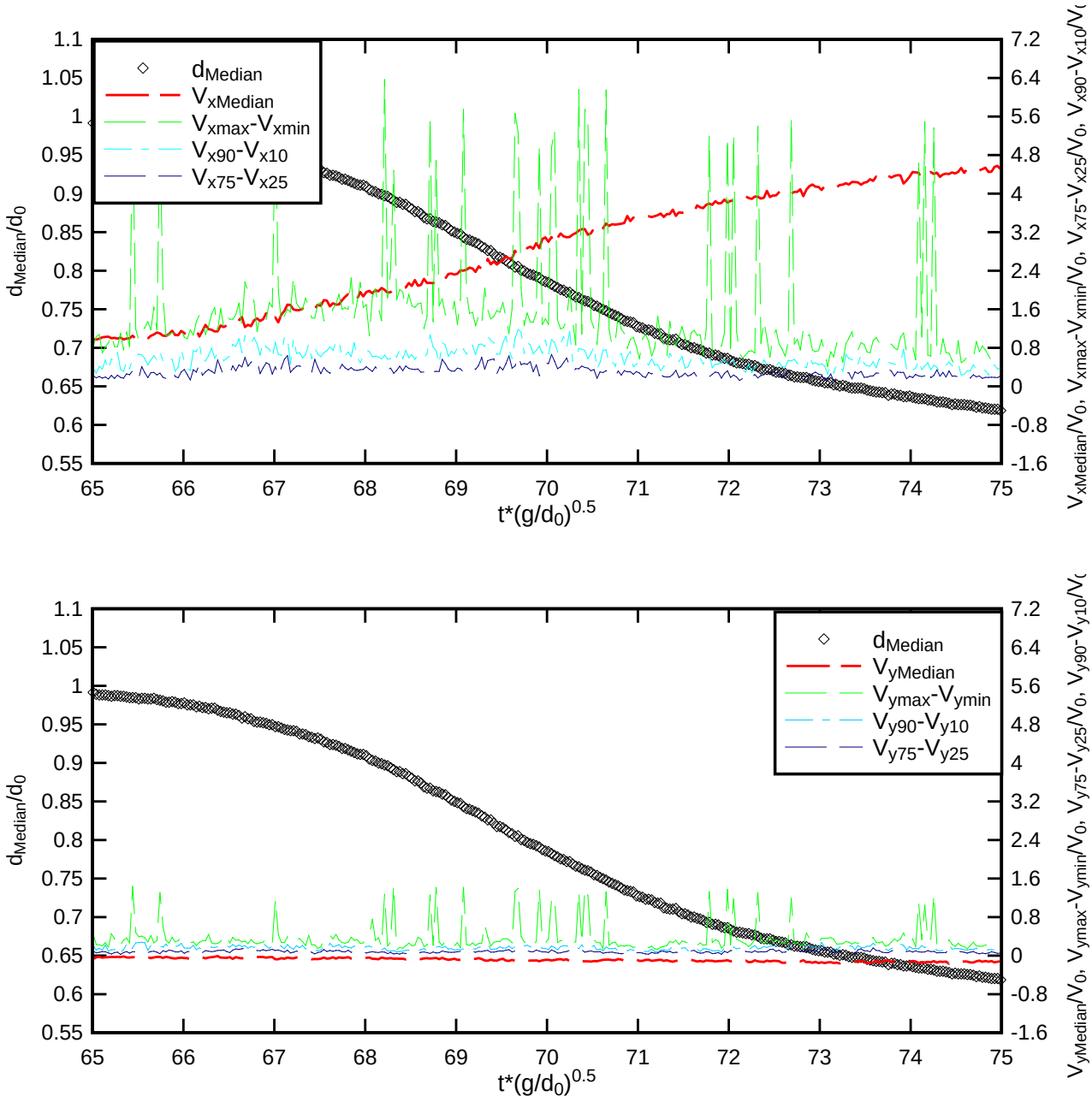

(a) z=25.01 mm, x=10.5 m (con't)

Figure B-4: Dimensionless ensemble-average median velocity $V_{yMedian}$, difference between 3rd and 4th quartiles (V_{75}- V_{25}) and 90% and 10% percentiles (V_{90}- V_{10}), and range of maximum to minimum velocities (V_{max}- V_{min}) at x=10.5 m- From Top to bottom V_x, V_y, V_z (con't)

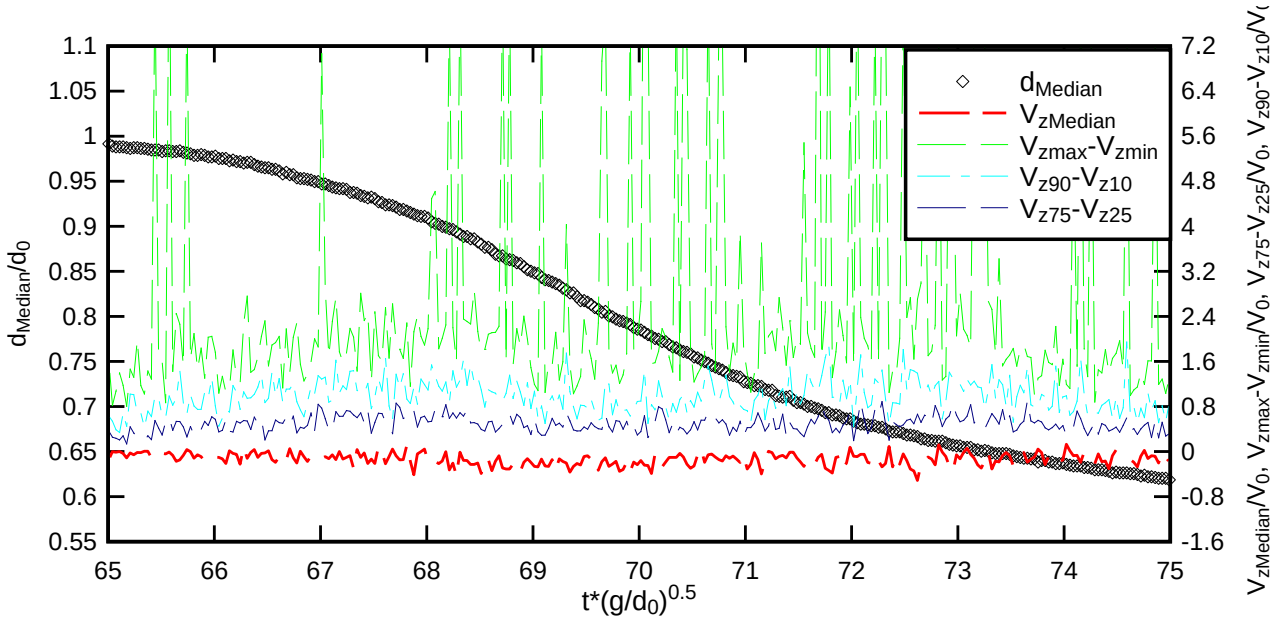

(a) z=25.01 mm, x=10.5 m

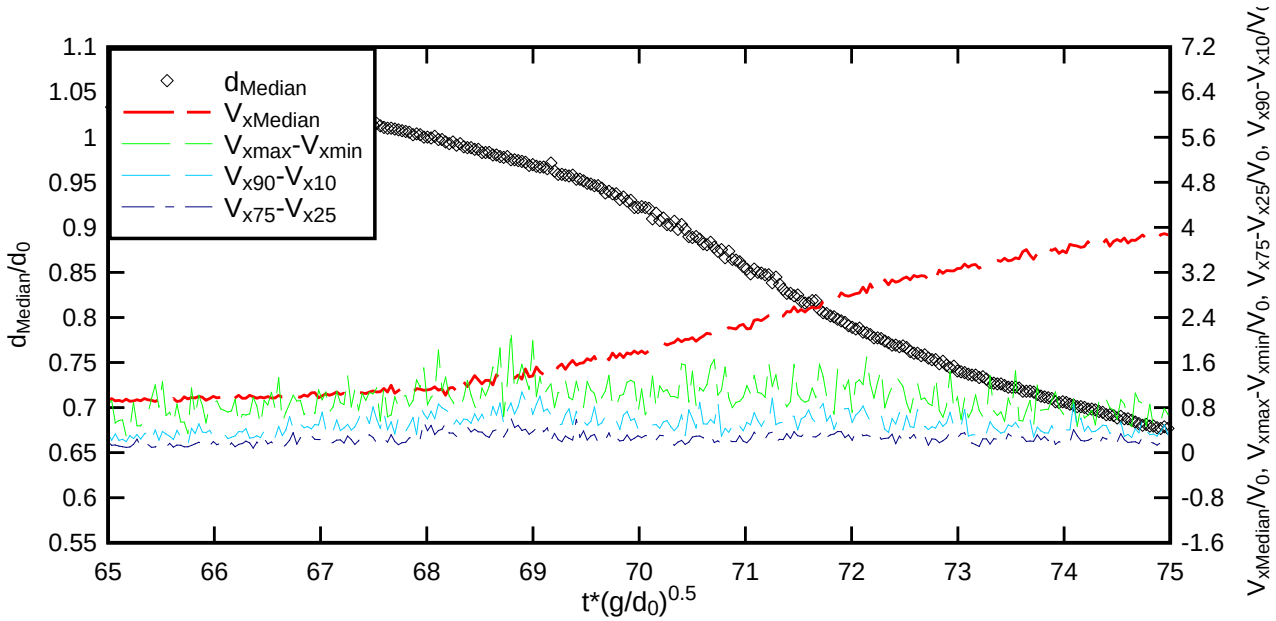

(b) z=123.94 mm, x=10.5 m (con't)

Figure B-4: Dimensionless ensemble-average median velocity $V_{yMedian}$, difference between 3rd and 4th quartiles (V_{75}- V_{25}) and 90% and 10% percentiles (V_{90}- V_{10}), and range of maximum to minimum velocities (V_{max}- V_{min}) at x=10.5 m- From Top to bottom V_x, V_y, V_z (con't)

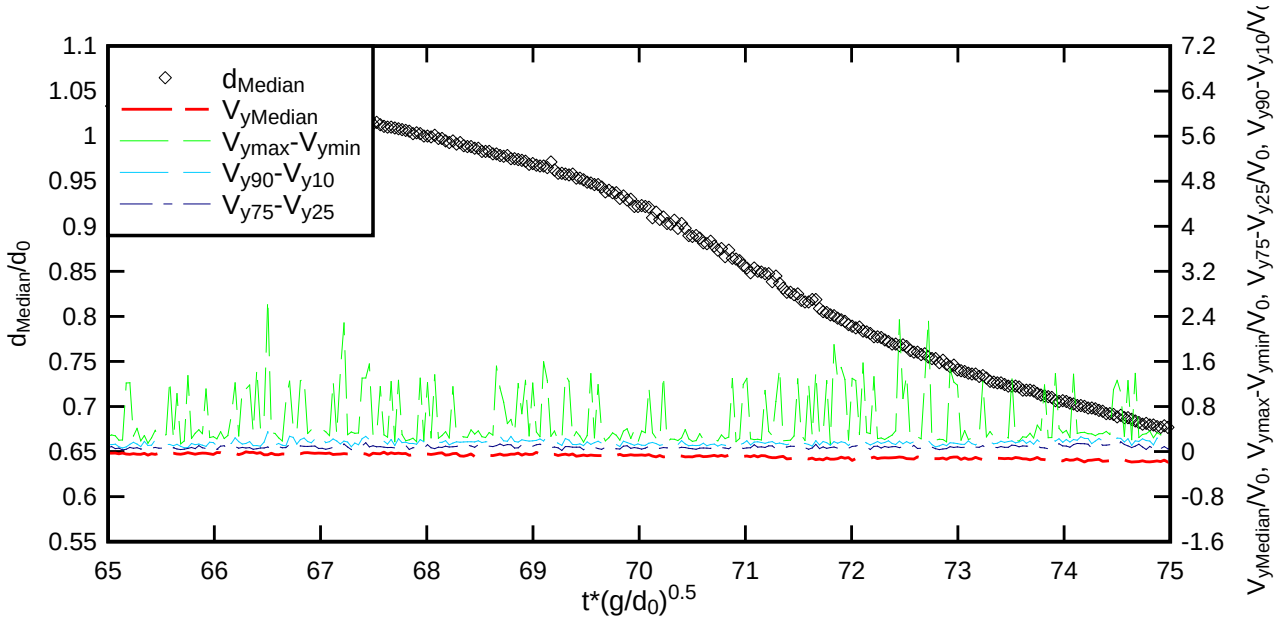

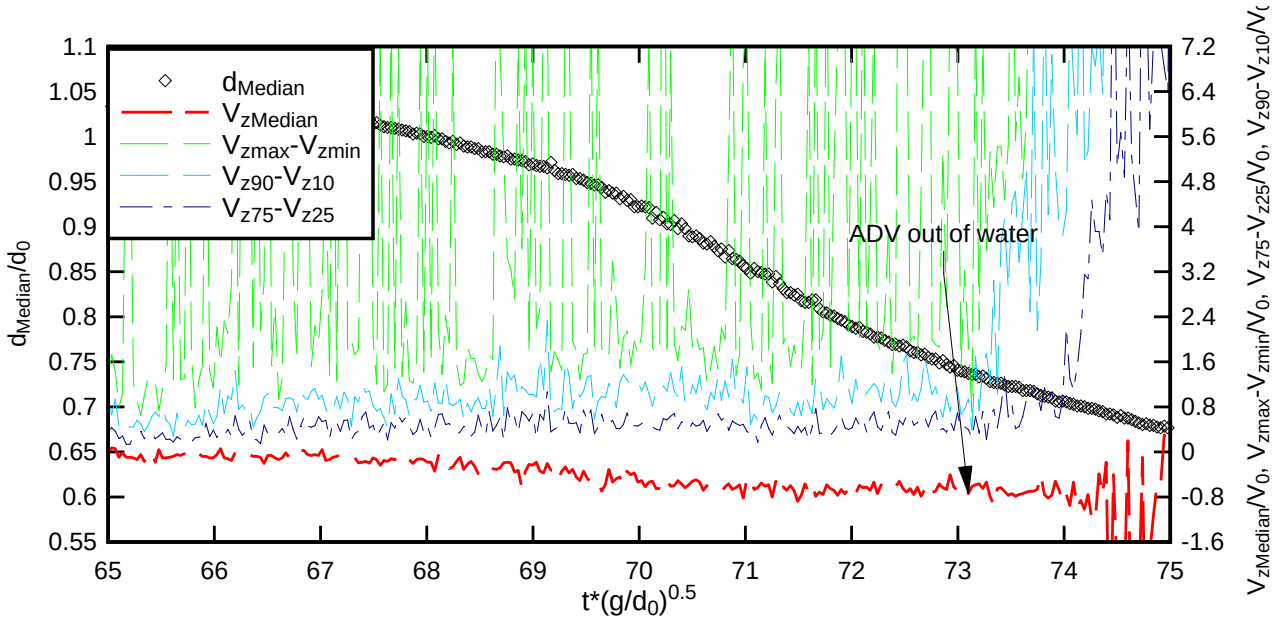

(b) z=123.94 mm, x=10.5 m

Figure B-4: Dimensionless ensemble-average median velocity $V_{yMedian}$, difference between 3rd and 4th quartiles (V_{75}- V_{25}) and 90% and 10% percentiles (V_{90}- V_{10}), and range of maximum to minimum velocities (V_{max}- V_{min}) at x=10.5 m- From Top to bottom V_x, V_y, V_z (con't)

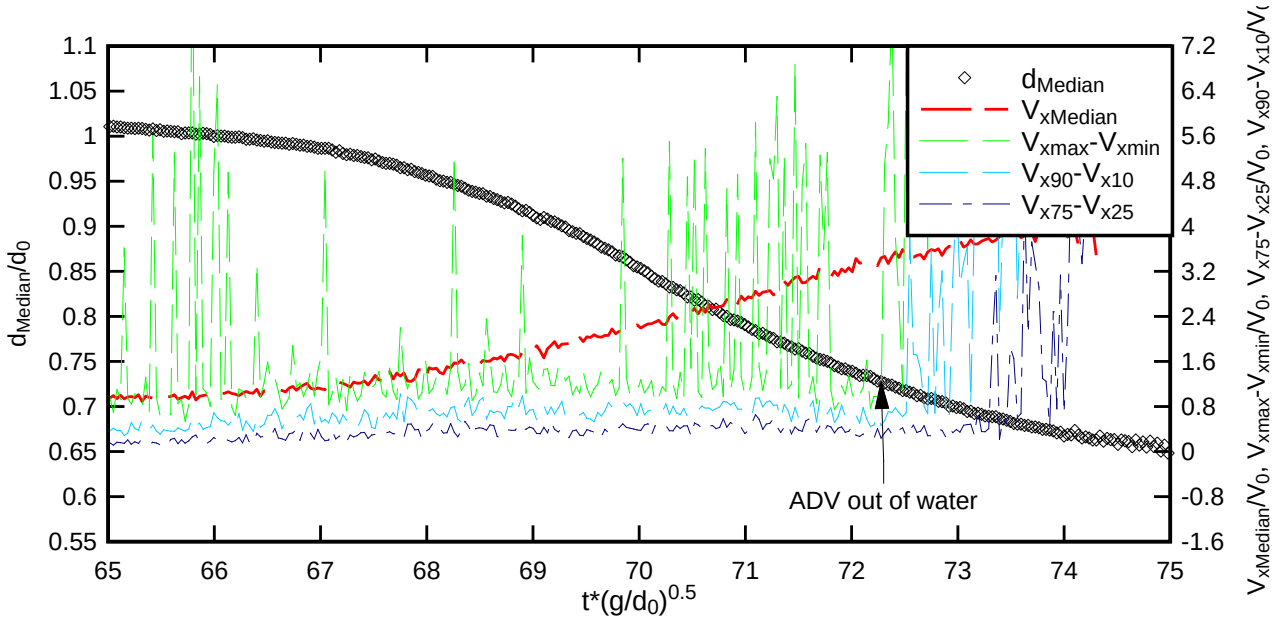
dMedian
VxMedian
Vxmax-Vxmin
Vx90-Vx10
Vx75-Vx25
ADV out of water
dMedian/d0
t*(g/d0)0.5
VxMedian/V0, Vxmax-Vxmin/V0, Vx75-Vx25/V0, Vx90-Vx10/V0

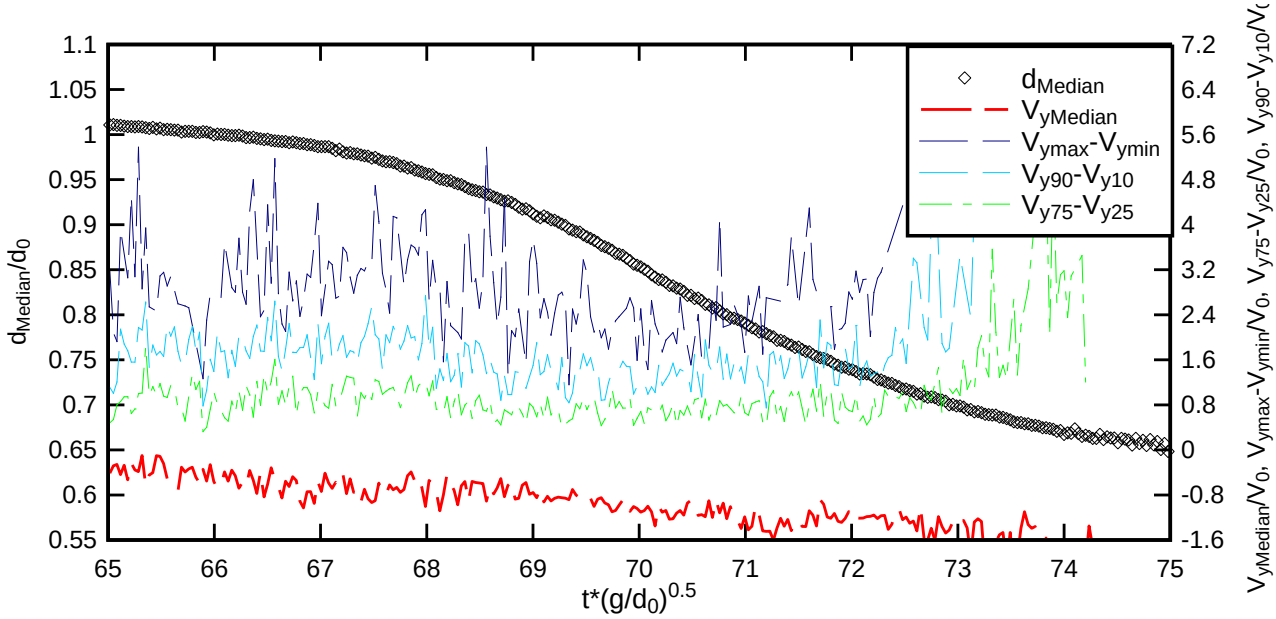
dMedian
VyMedian
Vymax-Vymin
Vy90-Vy10
Vy75-Vy25
dMedian/d0
t*(g/d0)0.5
VyMedian/V0, Vymax-Vymin/V0, Vy75-Vy25/V0, Vy90-Vy10/V0

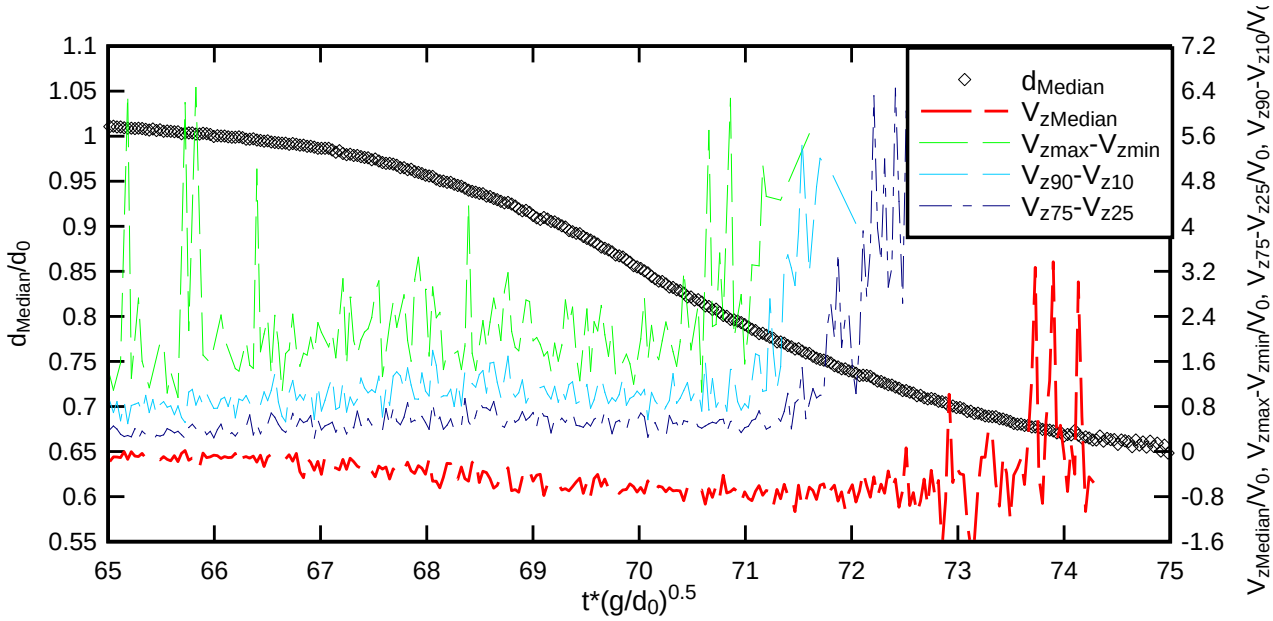

(c) z=135.2 mm, x=10.5 m

Figure B-4: Dimensionless ensemble-average median velocity $V_{yMedian}$, difference between 3rd and 4th quartiles (V_{75}- V_{25}) and 90% and 10% percentiles (V_{90}- V_{10}), and range of maximum to minimum velocities (V_{max}- V_{min}) at x=10.5 m- From Top to bottom V_x, V_y, V_z

Appendix C - Ensemble-average results – positive surge

C-1.Presentation

A series of 25 instantaneous velocity records were prepared at four vertical locations above the smooth PVC bed. The acoustic Doppler velocimeter (ADV) sampled the instantaneous velocity components on the channel centreline at x=10.5 m and x=6 m and four vertical sampling locations z=6.69 mm, 25.01 mm, 123.94 mm and 135.2 mm.

Notations

d_o	initial reservoir height (m) measured normal to the chute invert;
Q	volume flow rate (m^3)
V_o	initial velocity (m/s);
x	longitudinal distance (m) measured from the upstream end;

C-2.Experimental Results

An ensemble-median of each instantaneous velocity component was produced for each vertical elevation of the ADV measurements. All the positive surge data were synchronised based on the characteristic time t_3, which is illustrated in Figure C-1.

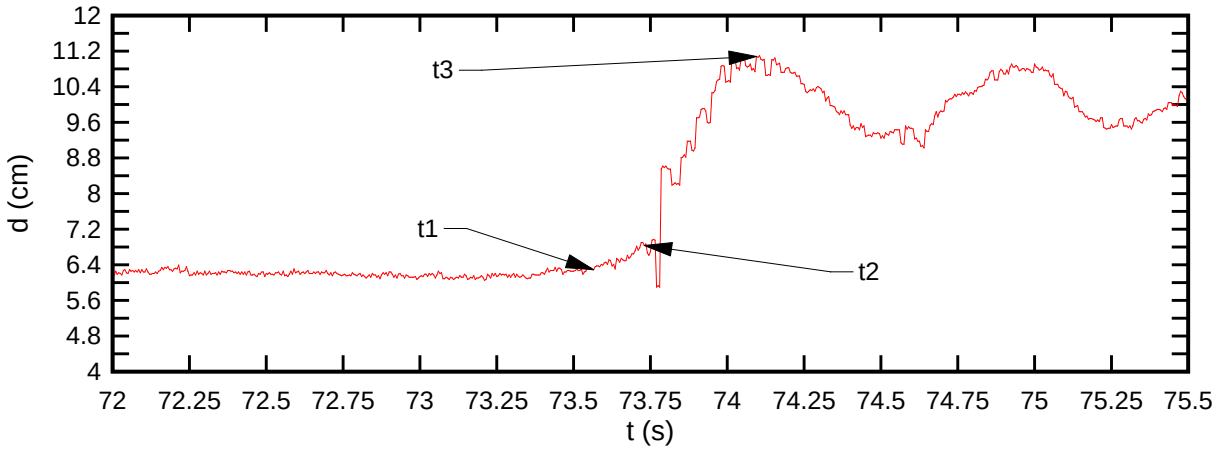

Figure C-1: Instantaneous water depth measurement for synchronisation purposes for the positive surge

The experimental results are shown in terms of ensemble-averaged median velocity component as a function of time. Each graph includes the ensemble-averaged median velocity component (V_x, V_y, V_z) the range of maximum to minimum velocities, the differences between the 3rd and 4th quartiles (V_{75}-V_{25}) and 90% and 10% percentiles, (V_{90}-V_{10}) and the ensemble-averaged water depth, d_{Median}.

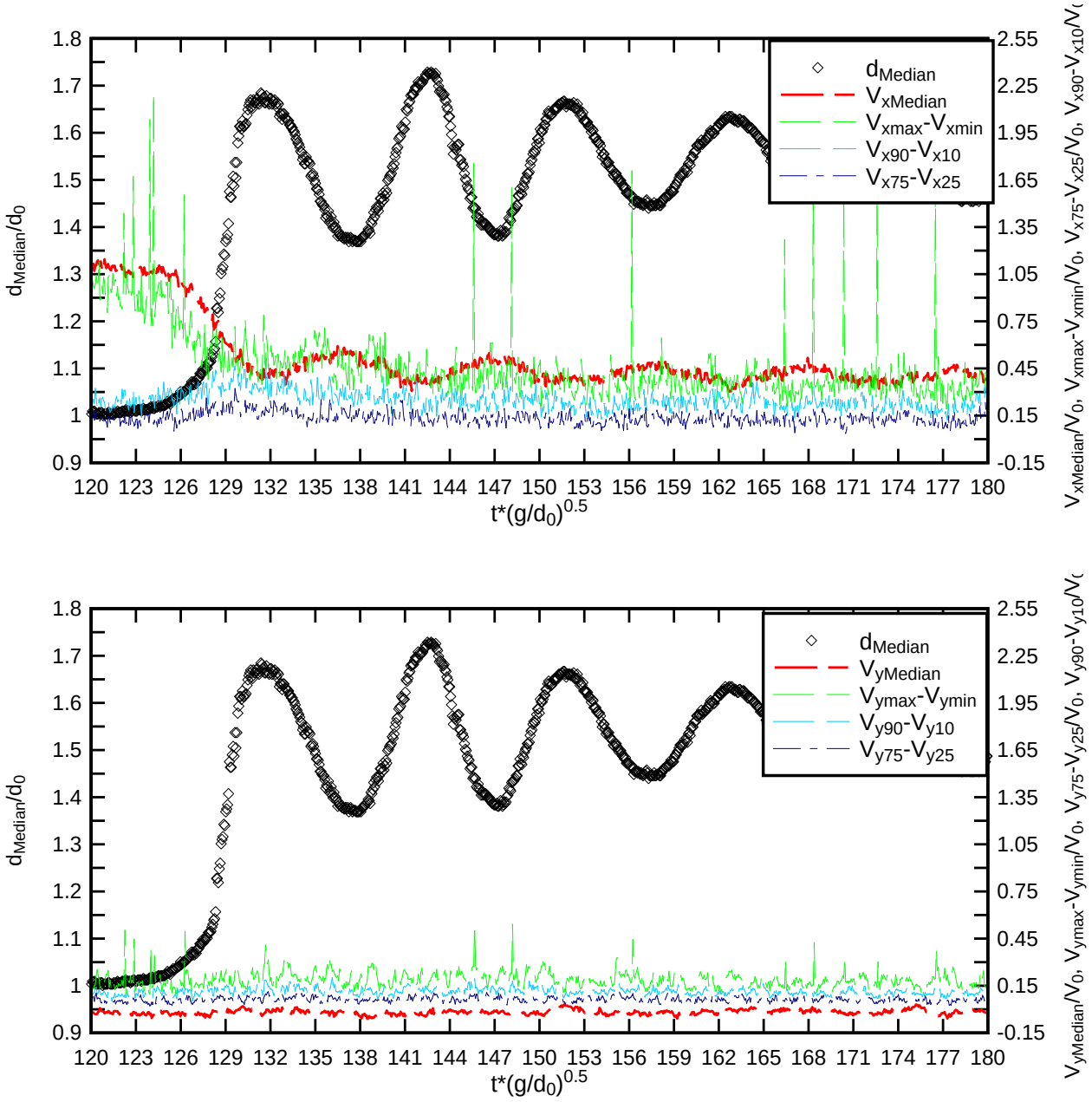

Figure C-2: Dimensionless ensemble-average median velocity $V_{yMedian}$, difference between 3rd and 4th quartiles (V_{75}- V_{25}) and 90% and 10% percentiles (V_{90}- V_{10}), and range of maximum to minimum velocities (V_{max}- V_{min}) at x=10.5 m and z=25.01 mm - From Top to bottom V_x, V_y, V_z (con't)

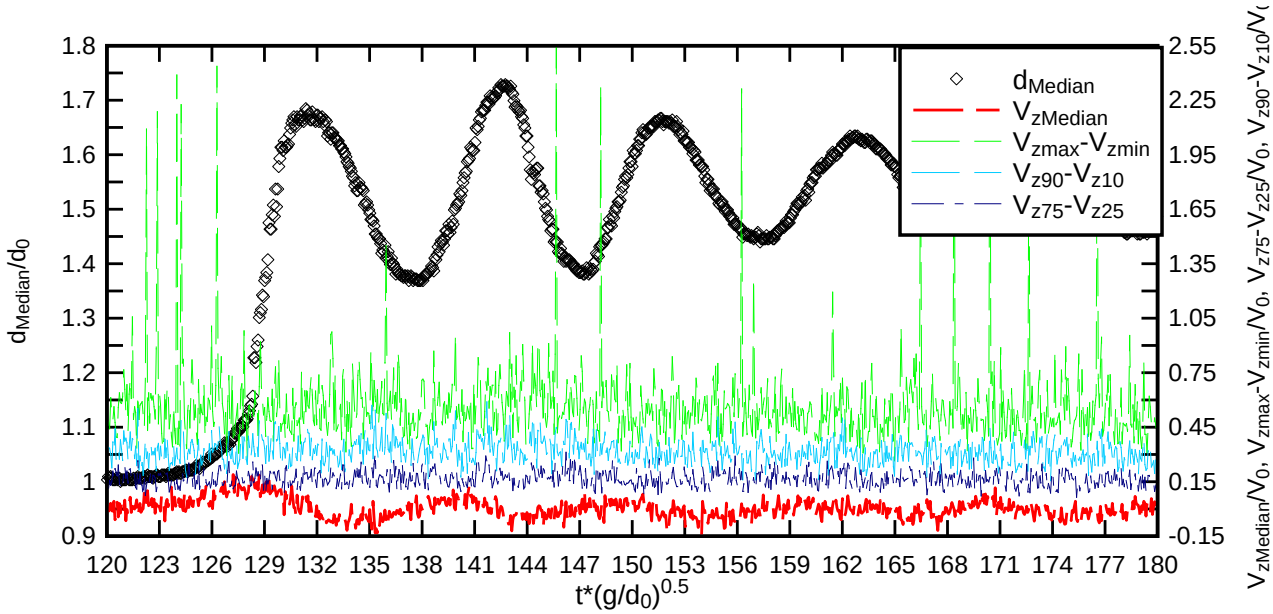

Figure C-2: Dimensionless ensemble-average median velocity $V_{yMedian}$, difference between 3rd and 4th quartiles (V_{75}- V_{25}) and 90% and 10% percentiles (V_{90}- V_{10}), and range of maximum to minimum velocities (V_{max}- V_{min}) at x=10.5 m and z=25.01 mm - From Top to bottom V_x, V_y, V_z

Appendix D – Flow-3D setup and results

D1- Presentation

Flow-3D^{TM} is a CFD model developed by Flow Science Inc.. Flow-3D^{TM} calculates the three velocity components (V_x, V_y, V_z) and pressures at the nodes of an orthogonal finite difference grid, using different turbulence models, selected by the user, such as *k*-ε, RNG and LES. Compared to other general purpose CFD codes, Flow-3D^{TM} has capabilities intended for hydraulic engineering applications, such as the capabilities of modelling free surface flow. Flow-3D^{TM} has been applied to model in-stream structures such as, spillways, stilling basins, water intakes and fish ladders. Flow-3D^{TM} uses the VOF method, which is at present one of the best methods available to simulate the movement of rapidly-varying water surfaces.

The models were set up using Flow-3D^{TM} version 9.3. Each model was set up with one fluid, incompressible flow and a free surface or sharp interface. The fluid properties were set as water at 20 degrees Celsius for all simulations.

There are different physics options available for selections, three options were activated to obtain accurate results for the cases presented in this report. The gravity option was selected with gravitational acceleration in the vertical direction set to -9.806m/s^2. The viscosity and turbulence option was selected with Newtonian viscosity and the renormalisation group (RNG) turbulence model that used dynamically computed maximum turbulence mixing length. The RNG model was selected because it was recommended as the most robust turbulence model available within the Flow-3D^{TM} modelling software by the Flow-3D^{TM} user manual (2007). The moving and deforming option was selected for the gate operation.

The geometry for the models was a simple rectangular channel with the same width and depth as the experimental channel. The length of the channel was extended by 0.8 m to reduce boundary effects. The gate was simulated using the general moving object (GMO). The GMO settings were set as prescribed motion with 6 degree of freedom (6-DOF). The initial location of the reference point was selected in the middle of the gate at x=11.2 m, y=0.25 m and z=0.25 m. The gate was operated using the translational velocity component in the space system with a velocity of non-sinusoidal movement in the z direction of -1 m/s for the positive surge and +1 m/s for the negative surge. The speed of the gate movement was selected to increase the stability of the model.

Different gate opening times were selected, but it was found that slower and faster gate opening times result in instability of the models resulting in the termination of the simulation. The gate movement for the simulations was vertical, which is different from the gate operation in the experimental setup, where the gate opens in a semi-circular movement.

The mesh subdivides the flow domain into smaller regions, where numerical values, such as velocity and pressure are calculated. Choosing the right mesh size is essential for both the accuracy of the result and the simulation times. It is important to get enough resolution to capture the important features of the geometry. However, the computing time can increase significantly with reducing the mesh size. Therefore, a sensitivity analysis was performed using three different uniform mesh sizes of 5 mm, 15 mm and 30 mm. It was decided that the channel is modelled in two dimensions instead of three, to reduce simulation time. To further reduce the simulation time, a restart file was produced simulating the steady flow conditions for each case for 200 s. The restart option allows the user to run a simulation before changing the model settings including its geometry and configuration. The simulation was restarted using the information calculated at the selected time step of the last simulation.

The selection of appropriate boundary conditions is essential for the accuracy of the simulations. Several boundary conditions were tested for both the negative and the positive surges. The boundary conditions are summarised in Table D-1. However, there are several other boundary options available in the software that could be applied for the cases in this study. The choice of the boundary options was made to replicate the steady flow state prior to the surge generation as closely to the experimental conditions as possible.

Table D-1: Boundary conditions

	X_{Min}	X_{Max}	Y_{Min}	Y_{Max}	Z_{Min}	Z_{Max}
Negative surge	**P**	**P**	**S**	**S**	**W**	**S**
Positive Surge	**Q**	**P**	**S**	**S**	**W**	**S**

Notes; P is the specified pressure boundary; S is the symmetry boundary; W is the wall boundary and Q stands for the volume flow rate boundary.

The numeric options within Flow-3D™ are modifications to the way the Reynolds-averaged Navier Stokes (RANS) equations are solved. The RANS equations are the fundamental underlying equations solved by Flow-3D™. The time steps were left as default, except the initial time step was adjusted down for initial model stability to 0.0002 s. A small initial time step was necessary for the simulations as the gate opening and closing using the GMO application resulted in an initially less stable model environment. The time step size was controlled by stability and convergence. The pressure solver option was selected as implicit with automatic limited compressibility and the implicit solver option was generalised minimum residual (GMRES). The simulations were calculated using the explicit solver options. The difference between the explicit and implicit solver options are that the explicit solution is solved progressively at each computational cell by stepping trough time, while the time step is restricted to meet stability criteria. On the other hand the implicit solution is solved in each time step using the information from a previous time step, which requires more complex interactive or matrix solution but does not impose time step restrictions. The models were run calculating both the momentum and continuity equation with a first order momentum advection.

D 2 – Flow-3D results

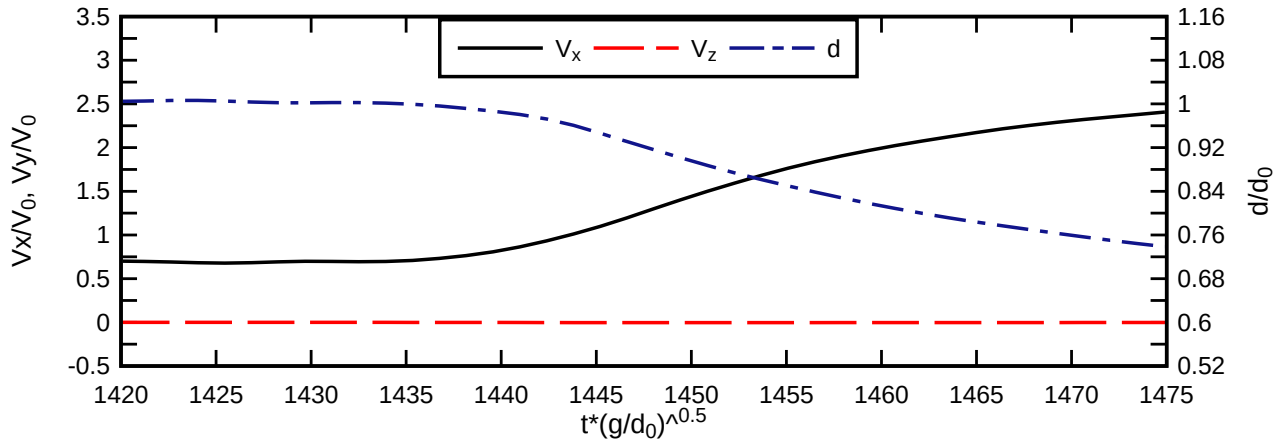

(a) x=6 m, z=7.5 mm, Q=20 l/s, d_0=0.20 m and initial gate opening 30 mm

Figure D-1 Dimensionless velocity and depth measurements of a negative surge Simulated using Flow-3D™ (con't)

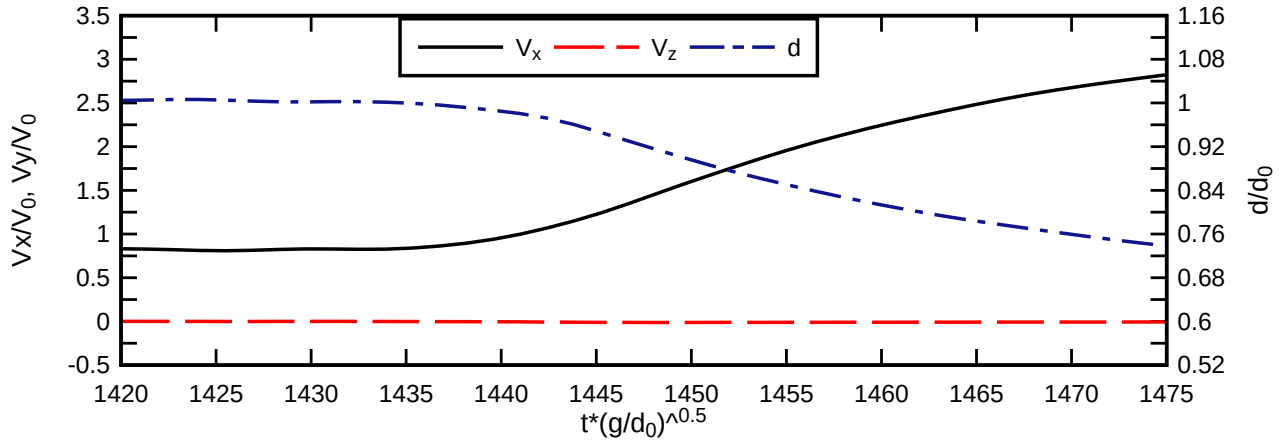

(b) x=6 m, z=22.5 mm, Q=20 l/s, d_0=0.20 m and initial gate opening 30 mm

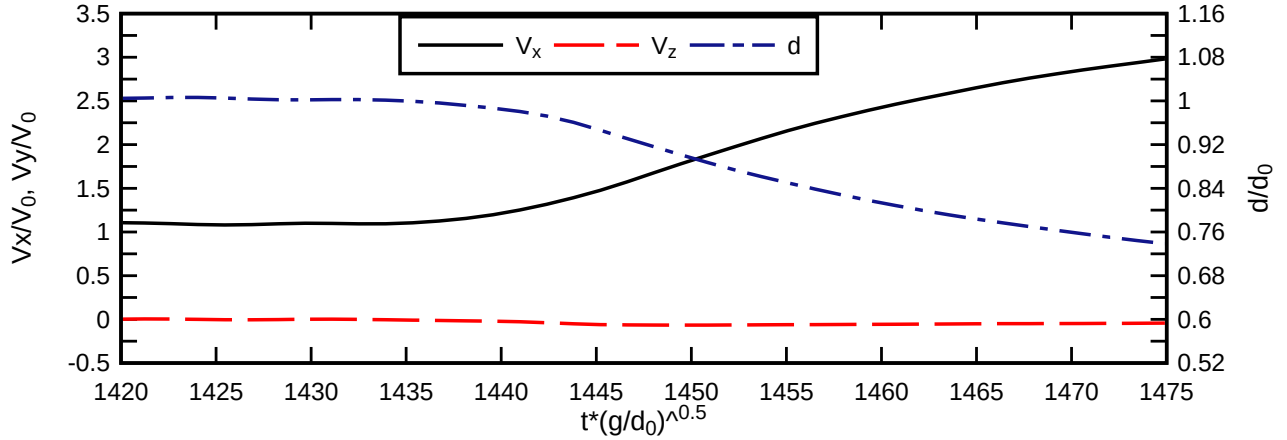

(c) x=6 m, z=123 mm, Q=20 l/s, d_0=0.20 m and initial gate opening 30 mm

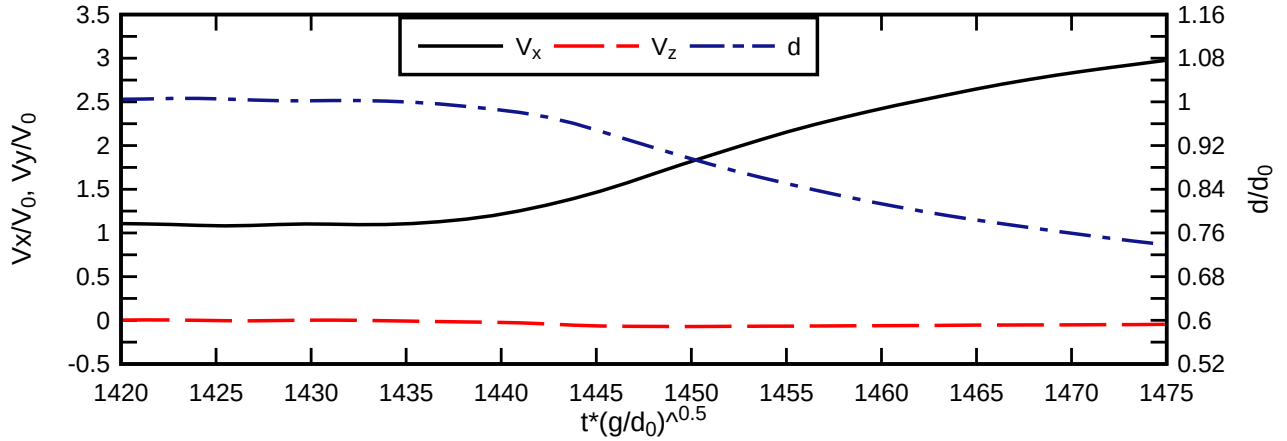

(d) x=6 m, z=138 mm, Q=20 l/s, d_0=0.20 m and initial gate opening 30 mm

Figure D-1 Dimensionless velocity and depth measurements of a negative surge Simulated using Flow-3D™

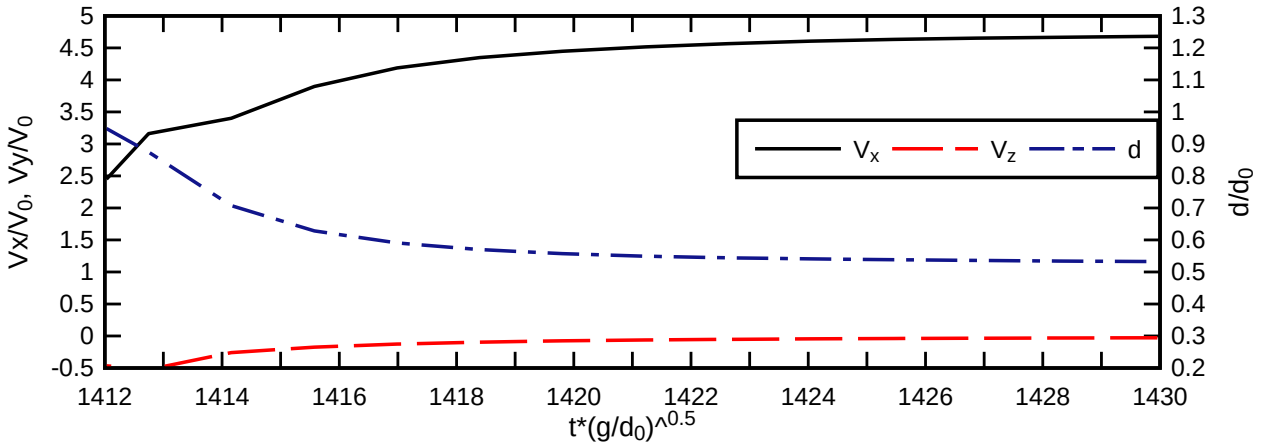

Figure D-2 Dimensionless velocity and depth measurements of a negative surge simulated using Flow-3D™: (a) x=10.5 m, z=22.5 mm, Q=20 l/s, d_0=0.20 m and initial gate opening 30 mm

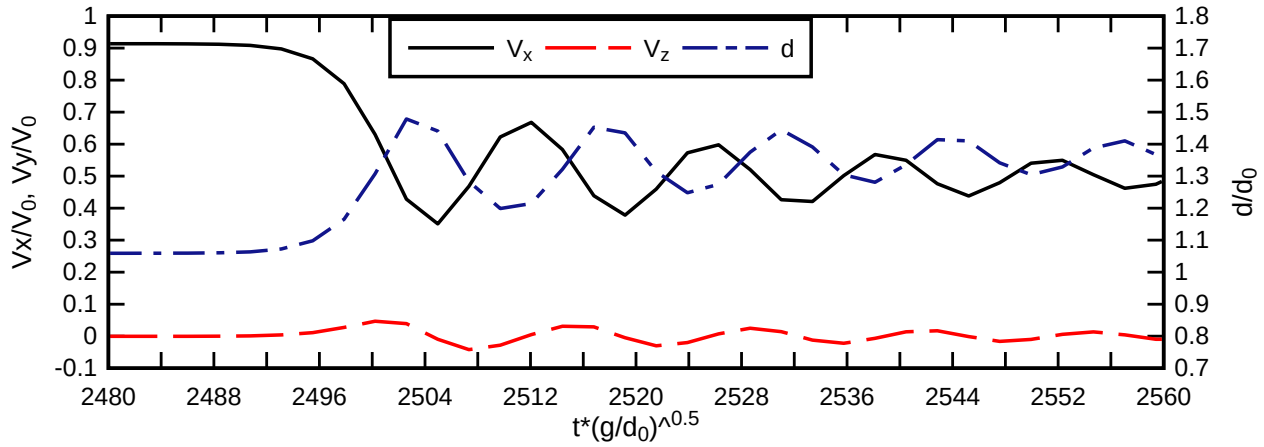

Figure D-3 Dimensionless velocity and depth measurements of a positive surge simulated using Flow-3D™ with x=6 m, z=22.5 mm, Q=20 l/s, d_0=0.064 m

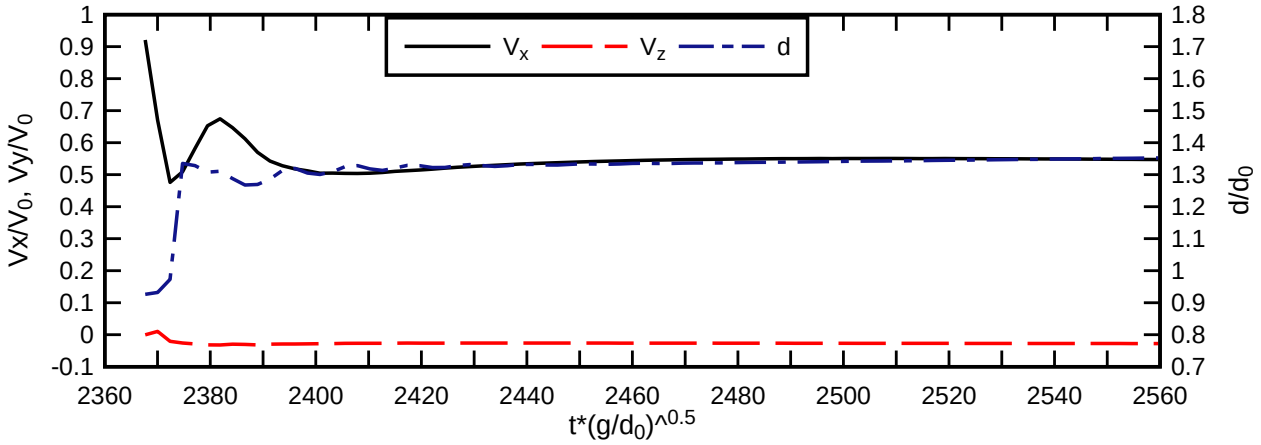

Figure D-4 Dimensionless velocity and depth measurements of a positive surge simulated using Flow-3D™ with x=10.5 m, z=22.5 mm, Q=20 l/s, d_0=0.064 m

Appendix E - Celerity

E1- Presentation

The celerity of the negative surge was measured from video and acoustic displacement meter data. Table E-1 summarises the celerity data and the initial flow conditions. Figures E-1 to E-4 illustrate the celerity results under different flow conditions.

Table E-1: Celerity measurements

Q	h	d_0	v_0	x	U	$(U+V_0)/sqrt(g*d_o)$
m^3/s	Gate	x=6m	x=6m	m	m/s	
0.020	0.030	0.236	0.169	8.550	1.599	1.162
0.020	0.030	0.230	0.174	6.150	0.923	0.718
				5.800	0.899	0.702
				10.650	0.984	0.758
0.020	0.030	0.240	0.167	10.350	1.765	1.271
				8.100	1.479	1.083
				11.092	0.136	0.197
0.020	0.050	0.100	0.400	11.080	0.436	0.393
				11.059	0.643	0.528
				11.039	0.340	0.331
				11.027	0.242	0.267
				11.011	0.560	0.474
				10.989	0.557	0.472
				10.945	1.664	1.194
				10.884	1.375	1.005
				11.092	0.382	0.790
0.030	0.040	0.260	0.231	11.080	0.225	0.631
				11.071	0.223	0.629
				11.060	0.328	0.735
				11.043	0.518	0.927
				11.033	0.418	0.826
				11.049	0.390	0.389
0.030	0.050	0.220	0.273	11.016	1.235	0.918
				10.972	0.975	0.755
				10.927	1.248	0.926
				10.888	0.722	0.597
				10.829	2.256	1.558
				10.756	1.365	1.000
				10.729	0.810	0.652
				11.048	0.490	0.519
0.020	0.030	0.240	0.167	11.038	0.011	0.193
				11.030	0.380	0.444
				11.011	0.556	0.564
				10.980	0.995	0.863
				10.940	1.034	0.890
				10.912	0.371	0.438
				10.904	0.615	0.604
				6.673	1.380	1.009
0.020	0.050	0.100	0.400	6.639	0.250	0.657
0.030	0.040	0.260	0.231	6.730	0.330	0.350
0.030	0.050	0.220	0.273	6.603	0.490	0.519

E 2 – Results

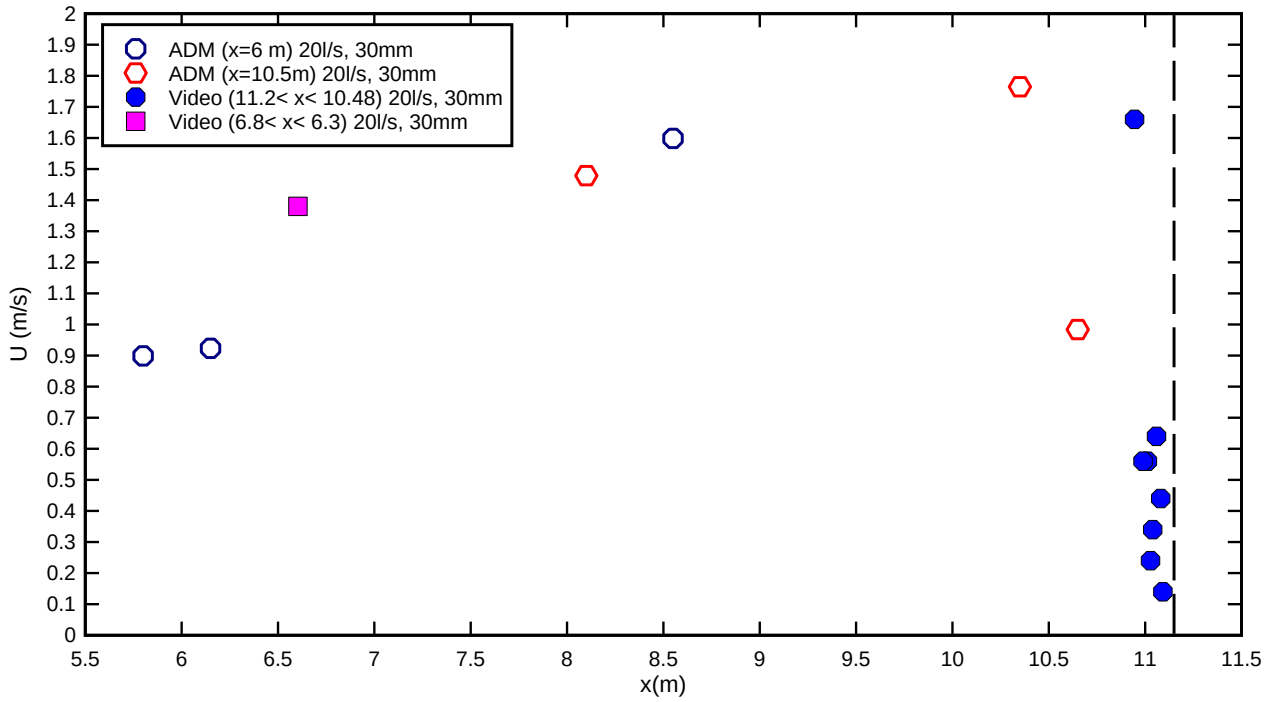

Figure E-1: Celerity measurements for Q= 20 l/s and a 30 mm gate opening

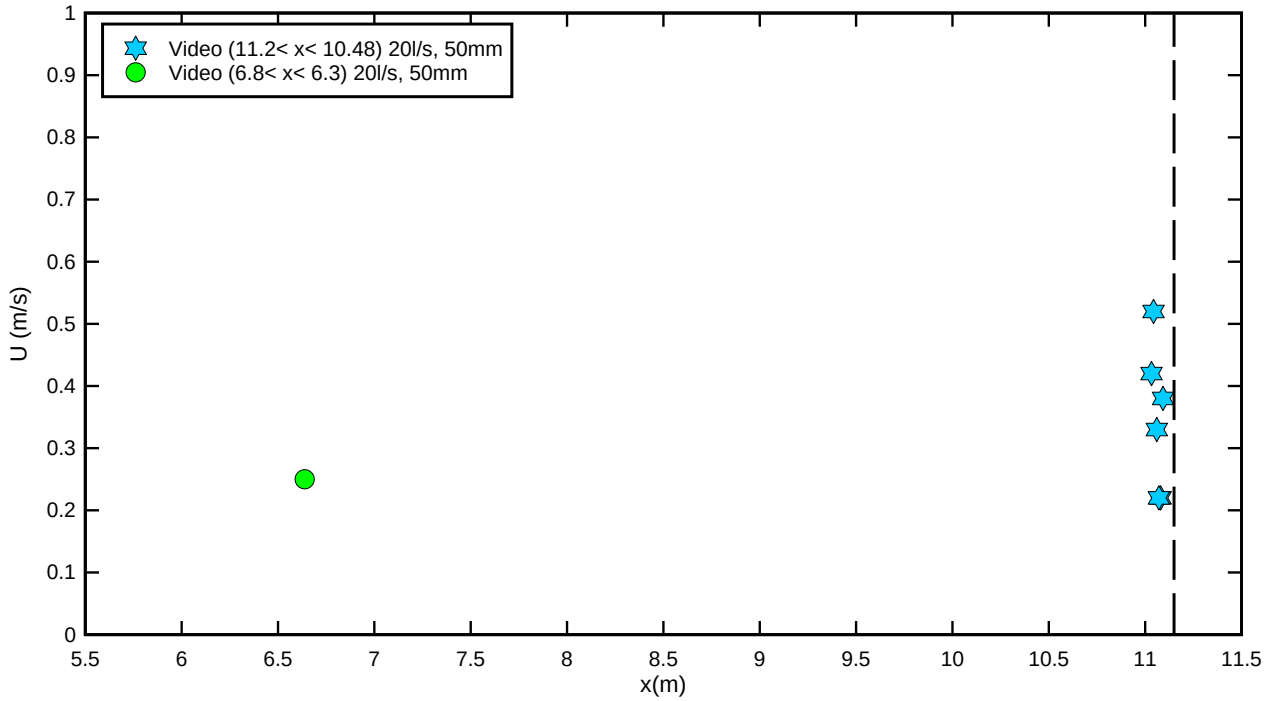

Figure E-2: Celerity measurements for Q=20 l/s and a 50 mm gate opening

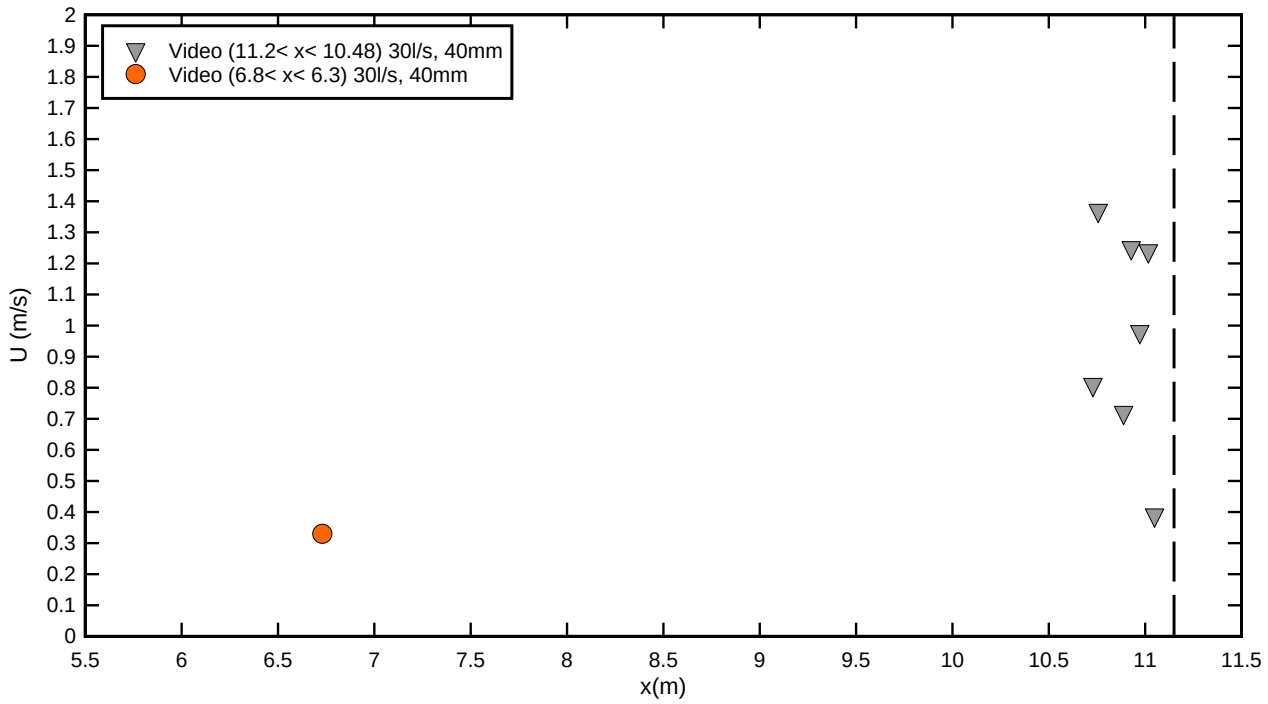

Figure E-3: Celerity measurements for Q= 30 l/s and a 40 mm gate opening

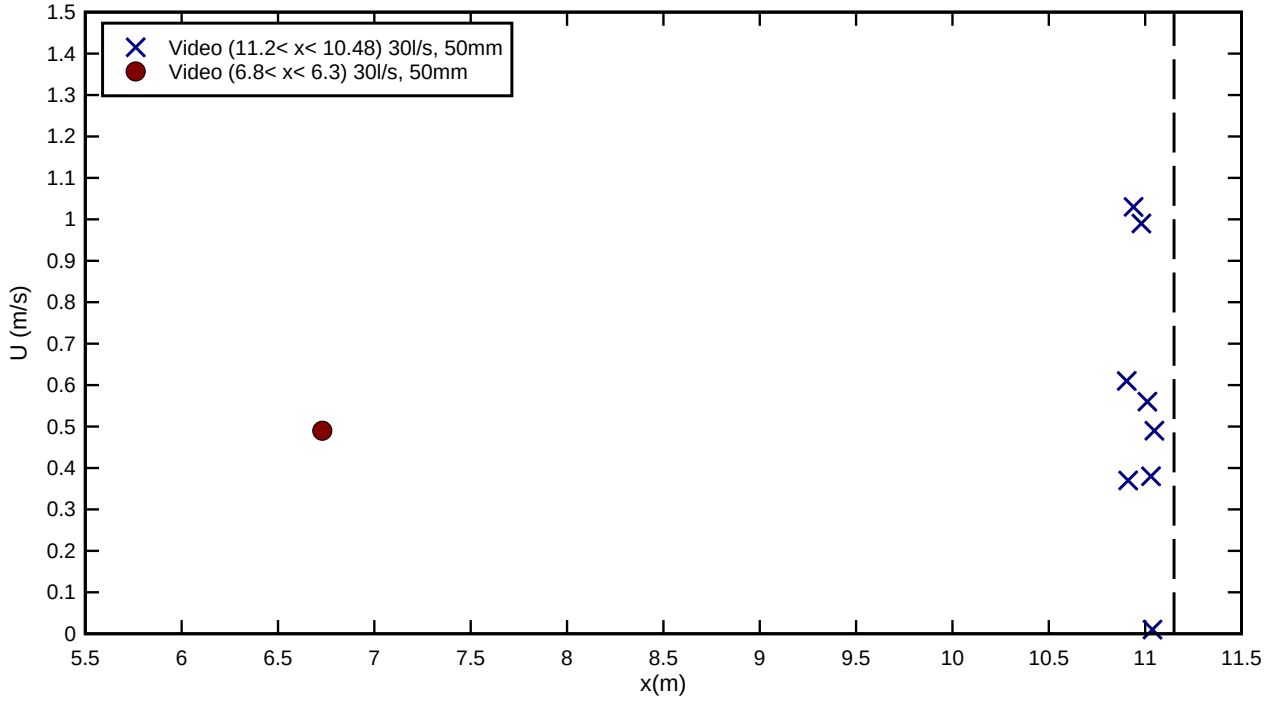

Figure E-4: Celerity measurements for Q= 30 l/s and a 50 mm gate opening

Appendix F – Steady state flow profiles

F-1 Presentation

The steady state flow profiles were recorded using ADM and video data. Typical steady state flow profiles using acoustic displacement meters for the negative and positive surge are illustrated in Figures F-1 and F-2 respectively. Typical steady state flow profiles using video recordings for the positive and negative surge are illustrated in Figures F-3 and F-4 respectively.

Notations

d_o	initial reservoir height (m) measured normal to the chute invert;
Q	volume flow rate (m^3)
V_o	initial velocity (m/s);
x	longitudinal distance (m) measured from the upstream end;

F-2 Results

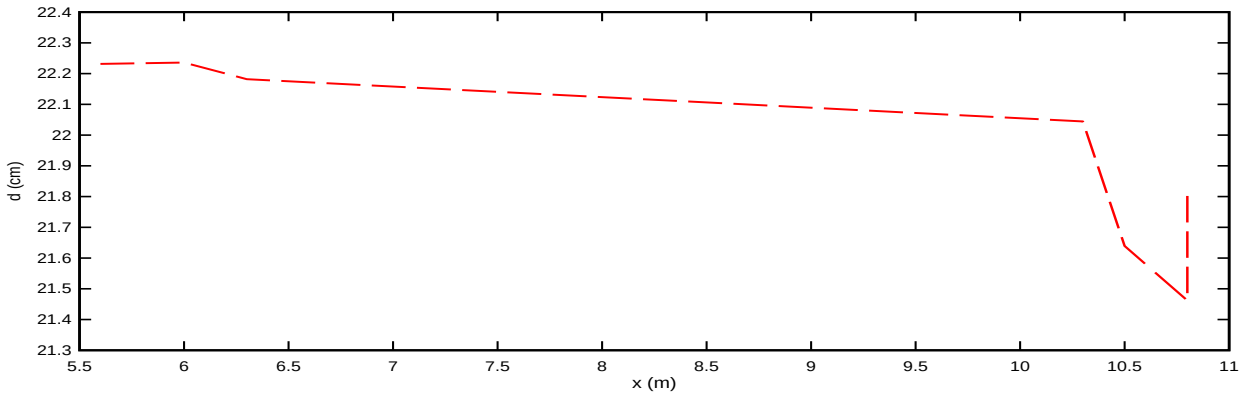

Figure F-1: Steady state profile for negative surge from ADM analysis, Q=20 l/s, h=30 mm, d_0 at 6 m

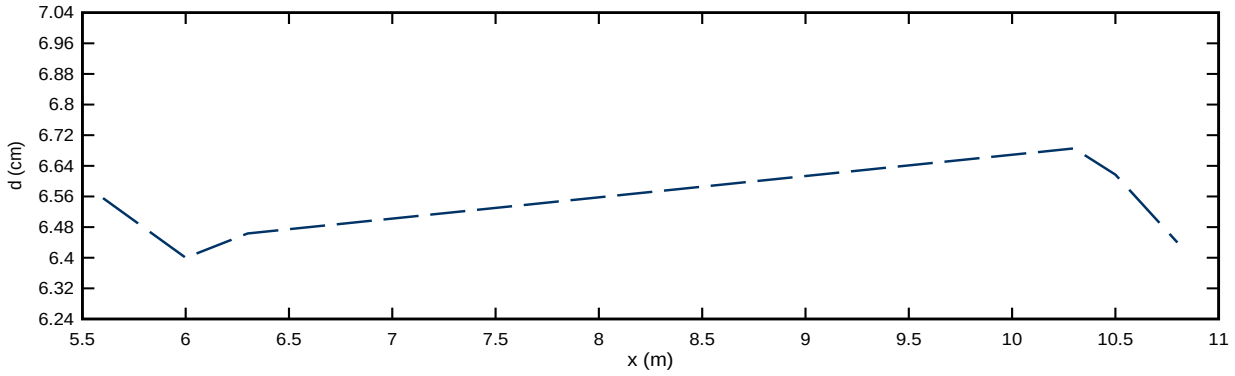

Figure F-2: Steady state profile for positive surge from ADM analysis, Q=20 l/s, h=30 mm, d_0 at 6 m

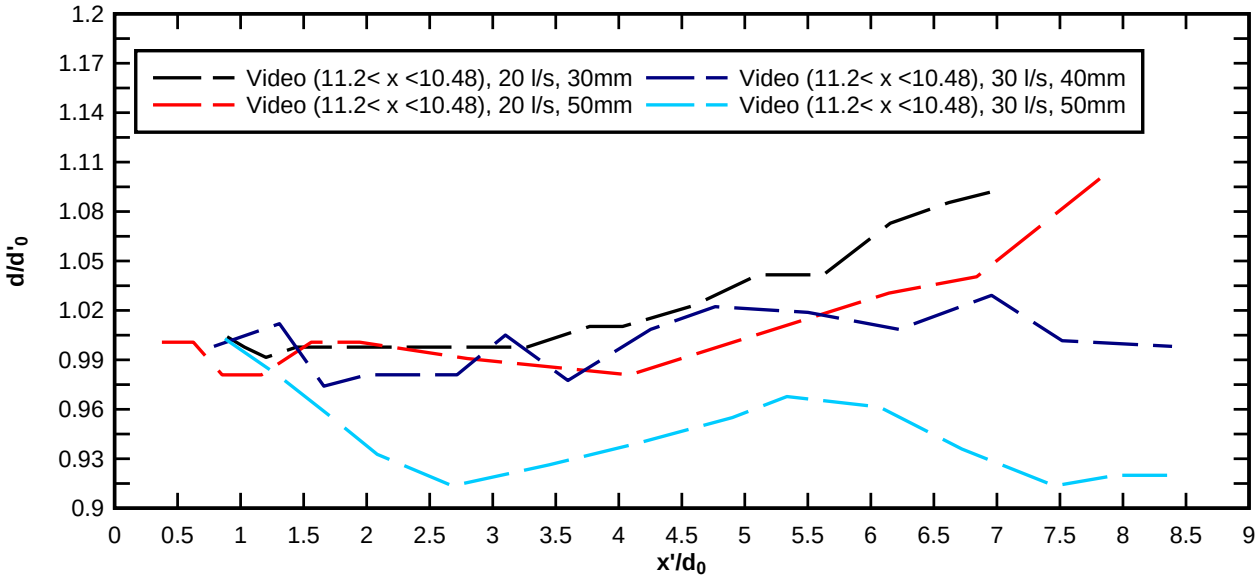

Figure F-3: Dimensionless steady state profile positive surge from video data analysis

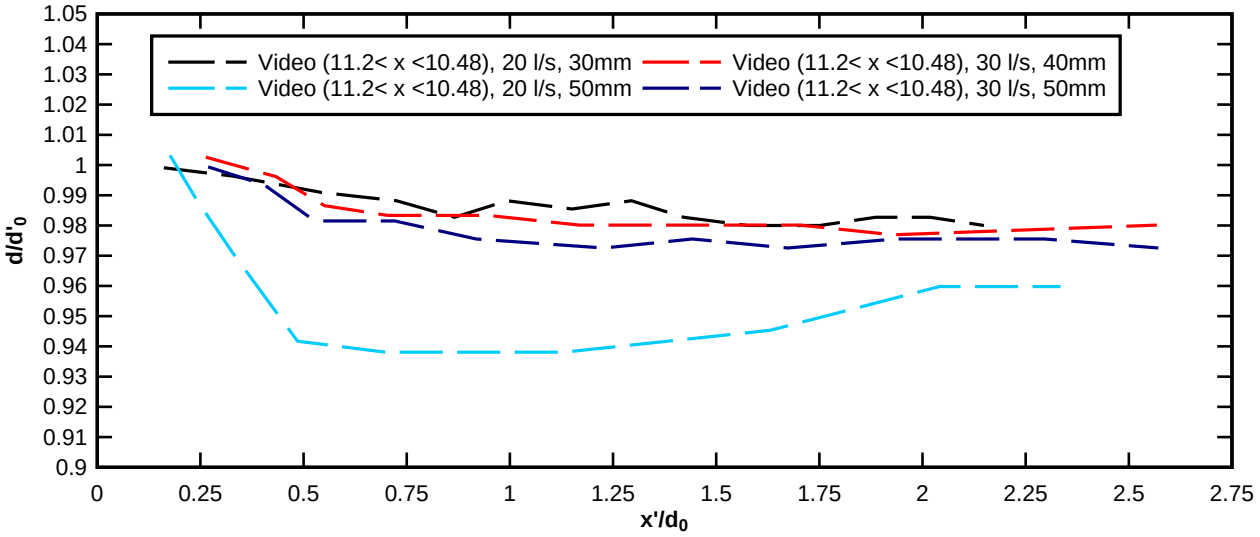

Figure F-4: Dimensionless steady state profile negative surge from video data analysis